

**NUMERICAL MODEL OF A RECIPROCATING ROD SEAL,  
INCLUDING SURFACE ROUGHNESS AND MIXED  
LUBRICATION**

A Thesis  
Presented to  
The Academic Faculty

By

Nicholas B. Maser

In Partial Fulfillment  
of the Requirements for the Degree  
Master of Science in Mechanical Engineering

Georgia Institute of Technology

December 2006

**NUMERICAL MODEL OF A RECIPROCATING ROD SEAL,  
INCLUDING SURFACE ROUGHNESS AND MIXED  
LUBRICATION**

Approved by:

Dr. Richard F. Salant, Advisor  
School of Mechanical Engineering  
*Georgia Institute of Technology*

Dr. Jeffrey L. Streater  
School of Mechanical Engineering  
*Georgia Institute of Technology*

Dr. Wayne J. Book  
School of Mechanical Engineering  
*Georgia Institute of Technology*

Date Approved: August 18, 2006

## **ACKNOWLEDGEMENTS**

I would like to thank Dr. Richard Salant, my advisor, for his efforts, expertise, and support during my graduate studies at Georgia Tech. Additional thanks are in order for Dr. Jeffrey Streater and Dr. Wayne Book for their time and efforts throughout my studies as well.

I also appreciate the funding from the CNR of the NFPA, as well as Eaton Hydraulics and Hallite Seals for their providing of a typical seal to be used for my research.

## TABLE OF CONTENTS

ACKNOWLEDGEMENTS .....	iii
LIST OF TABLES .....	vi
LIST OF FIGURES .....	vii
NOMENCLATURE .....	x
SUMMARY .....	xiv
CHAPTER 1 INTRODUCTION .....	1
CHAPTER 2 LITERATURE REVIEW .....	4
2.1 Fluid Sealing Technology .....	5
2.2 Initial Seal Studies using FEA .....	6
2.3 Previous Numerical Models.....	6
2.4 Previous Experimental Results .....	7
2.5 Recent Studies.....	8
2.6 Pressure and Shear Flow Factors .....	8
CHAPTER 3 METHODOLOGY .....	9
3.1 Fluid Mechanics Analysis.....	11
3.1.1 Numerical Scheme - Discretization of the Reynolds Equation.....	12
3.1.2 Cavitation Effects.....	17
3.1.3 Additional Assumptions.....	18
3.1.4 Auxiliary Calculations .....	18
3.1.5 Flow Factors.....	19
3.2 Deformation - FEA for Influence Coefficients.....	23

3.3 Contact Mechanics.....	29
3.4 Program Details .....	30
CHAPTER 4 RESULTS .....	33
4.1 Dimensionless Results for 6.9 MPa Sealed Pressure.....	33
4.2 Dimensionless Results for 13.8 MPa Sealed Pressure.....	48
4.3 Dimensional Results for 6.9 MPa Sealed Pressure.....	60
4.4 Dimensional Results for 13.8 MPa Sealed Pressure.....	64
CHAPTER 5 CONCLUSIONS .....	69
APPENDIX A TDMA Procedure.....	70
APPENDIX B Dimensional Results for 6.9 MPa Sealed Pressure .....	73
APPENDIX C Dimensional Results for 13.8 MPa Sealed Pressure .....	80
REFERENCES .....	87

## LIST OF TABLES

Table 1: Coefficient values used to calculate $\phi_{xx}$ .....	20
Table 2: Coefficients used in Equations 24 and 25 .....	21
Table 3: Coefficients used in Equation 26 .....	21
Table 4: Coefficients used in Equation 27 .....	22
Table 5: Base seal parameters .....	34
Table 6: Dimensionless flow rates for base case, 6.9 MPa sealed .....	39
Table 7: Leakage rates for base cases, 6.9 MPa sealed .....	43
Table 8: Dimensionless flow rates for base case, 13.8 MPa sealed .....	53
Table 9: Leakage rates for base cases, 13.8 MPa sealed .....	56
Table 10: Fluid transport results for different roughness values .....	63
Table 11: Fluid transport results for different roughness values .....	67

## LIST OF FIGURES

Figure 1: Typical seal configuration .....	5
Figure 2: Sealing zone of previous numerical models.....	9
Figure 3: Sealing zone for new numerical model .....	10
Figure 4: Diagram of control volume for discretization process .....	13
Figure 5: Meshing of geometries .....	25
Figure 6: Deformed seal with meshing.....	27
Figure 7: Influence coefficients for the deformation analysis .....	28
Figure 8: Computational scheme .....	32
Figure 9: Film thickness distributions, base case.....	35
Figure 10: Pressure distributions, base case, outstroke.....	36
Figure 11: Pressure distributions, base case, instroke.....	37
Figure 12: Frictional shear stress distributions, base case .....	38
Figure 13: Flow rate/speed vs. roughness, base case speeds .....	40
Figure 14: Flow rate/speed vs. speed for 1.392 & 2.320 roughnesses (0.3 $\mu\text{m}$ & 0.5 $\mu\text{m}$ ) .....	42
Figure 15: Pressure distributions, 2.320 roughness (0.5 $\mu\text{m}$ ), base speeds, outstroke.....	44
Figure 16: Pressure distributions, 2.320 roughness (0.5 $\mu\text{m}$ ), base speeds, instroke.....	45
Figure 17: Film thickness distributions, 2.320 roughness (0.5 $\mu\text{m}$ ), base speeds.....	47
Figure 18: Film thickness distributions, base case.....	48
Figure 19: Pressure distributions, base case, outstroke.....	50
Figure 20: Pressure distributions, base case, instroke.....	51

Figure 21: Frictional shear stress distributions, base case .....	52
Figure 22: Flow rate/speed vs. roughness, base case speeds, 13.8 MPa.....	54
Figure 23: Flow rate/speed vs. speed for 1.392 & 2.320 roughness (0.3 $\mu\text{m}$ & 0.5 $\mu\text{m}$ )..	55
Figure 24: Pressure distributions, 2.320 roughness (0.5 $\mu\text{m}$ ), base speeds, outstroke.....	57
Figure 25: Pressure distributions, 2.320 roughness (0.5 $\mu\text{m}$ ), base speeds, instroke.....	58
Figure 26: Film thickness distributions, 2.320 roughness (0.5 $\mu\text{m}$ ), base speeds.....	59
Figure 27: Fluid transport vs. roughness.....	61
Figure 28: Fluid transport vs. rod speed for 0.3 $\mu\text{m}$ roughness .....	62
Figure 29: Fluid transport vs. rod speed for 0.5 $\mu\text{m}$ roughness .....	63
Figure 30: Fluid transport vs. roughness for 13.8 MPa .....	65
Figure 31: Fluid transport vs. rod speed for 0.3 $\mu\text{m}$ roughness .....	66
Figure 32: Fluid transport vs. rod speed for 0.5 $\mu\text{m}$ roughness .....	67
Figure 33: Nodal definitions .....	70
Figure 34: Film thickness distributions, base case.....	73
Figure 35: Pressure distributions, outstroke, base case.....	74
Figure 36: Pressure distributions, instroke, base case.....	75
Figure 37: Frictional shear stress distributions, base case .....	76
Figure 38: Pressure distributions, outstroke, 0.5 $\mu\text{m}$ roughness .....	77
Figure 39: Pressure distributions, instroke, 0.5 $\mu\text{m}$ roughness .....	78
Figure 40: Film thickness distributions, 0.5 $\mu\text{m}$ roughness .....	79
Figure 41: Dimensional film thickness distributions for 13.8 MPa, base case.....	80
Figure 42: Dimensional pressure distributions, outstroke, base case, 13.8 MPa.....	81
Figure 43: Dimensional pressure distributions, instroke, base case, 13.8 MPa.....	82



Figure 44: Frictional shear stress distributions, base case, 13.8 MPa.....	83
Figure 45: Dimensional pressure distributions, outstroke, 0.5 $\mu\text{m}$ roughness.....	84
Figure 46: Dimensional pressure distributions, instroke, 0.5 $\mu\text{m}$ roughness.....	85
Figure 47: Dimensional film thickness distributions for 13.8 MPa, 0.5 $\mu\text{m}$ roughness ...	86

## NOMENCLATURE

$E$	elastic modulus
$E^*$	$E / (1 - \nu^2)$
$F$	cavitation index
$f$	friction coefficient
$F(\delta)$	dimensionless probability density function of roughness
$h$	film thickness
$H$	dimensionless average film thickness, $h / \sigma$
$h_s$	static undeformed film thickness
$H_s$	dimensionless static undeformed film thickness, $h_s / \sigma$
$h_T$	average truncated film thickness
$H_T$	dimensionless average truncated film thickness, $h_T / \sigma$
$I_1$	influence coefficient for normal (radial) deformation
$I$	function defined by Equation 38
$L$	length of solution domain in x-direction
$p$	fluid pressure
$P$	dimensionless fluid pressure, $p / p_a$
$p_a$	ambient pressure
$p_c$	contact pressure
$P_c$	dimensionless contact pressure for deformation analysis, $p_c / E$
$P_{def}$	dimensionless fluid pressure for deformation analysis, $P \cdot p_a / E$

$P_t$	dimensionless total pressure, $P_{def} + P_c$
$p_{sc}$	static contact pressure
$P_{sc}$	dimensionless static contact pressure, $p_{sc} / E$
$P_{sealed}$	sealed pressure
$P_{sealed}$	dimensionless sealed pressure, $p_{sealed} / p_a$
$\hat{Q}$	dimensionless flow rate in x-direction per unit length in y-direction, $12\mu_0 QL / (p_a \sigma^3)$
$\hat{q}$	dimensionless flow rate during stroke, $12\mu_0 qL / (p_a \sigma^3)$
$R$	asperity radius
$U$	surface speed of rod
$\hat{x}$	dimensionless axial coordinate, $x / L$
$\hat{\alpha}$	dimensionless pressure-viscosity coefficient, $\alpha \cdot p_a$
$\phi$	fluid pressure/density function
$\phi_f, \phi_{fss}, \phi_{fpp}$	shear stress factors
$\phi_{s.c.x}$	shear flow factor
$\phi_{xx}$	pressure flow factor
$\mu_0$	viscosity at atmospheric pressure
$\hat{\rho}$	dimensionless density, $\rho / \rho_t$
$\rho_t$	liquid density
$\sigma$	dimensional rms roughness
$\hat{\sigma}$	dimensionless rms roughness of sealing element surface, $\sigma \cdot R^{1/3} \eta^{2/3}$

$\hat{\tau}_{avg}$	average dimensionless viscous shear stress in the x-direction, $\tau_{avg} / E$
$\hat{\tau}_c$	shear stress due to contacting asperities
$\left[ \hat{\tau}_{avg} \right]_t$	total shear stress, $\hat{\tau}_{avg} + \hat{\tau}_c$
$\nu$	Poisson's ratio
$\xi$	$R^{1/3} \eta^{2/3} EL / p_a$
$\zeta$	dimensionless rod speed, $(\mu_0 UL) / (p_a \cdot \sigma^2)$
$\eta$	asperity density
$\mu$	viscosity
$\gamma$	aspect ratio of asperities
$\Delta x$	nodal step size
$D$	rod diameter
$\varepsilon$	error

### Superscripts

$\wedge$	dimensionless quantity
----------	------------------------

### Subscripts

$a$	ambient
$avg$	average
$c$	contact
$def$	deformation
$i, i + 1, i - 1$	nodal locations

$s$	static
$sc$	static contact
$sealed$	sealed
$t$	total
$T$	truncated
$W, E, P$	nodes defined by Figure 4
$w, e$	nodes defined by Figure 4

## SUMMARY

Currently, finite element analysis (FEA) serves as the only analytical tool used in the evaluation of reciprocating hydraulic rod seals. The FEA does not allow for dynamic analysis of the seal, which must be performed experimentally. As a result, the designing of a seal is basically an empirical process that can be both a costly and extensive procedure. The aim of this project is to develop a numerical model and computer program that will have the ability to predict key seal performance characteristics, such as leakage and friction. This numerical model will provide a means for evaluating potential seal designs, which can be performed without having to endure the costs of creating and evaluating the performance of the seal. Thus, the numerical model and computer program will assist the seal designers in reducing the time and cost involved in evaluating potential seal designs. Hopefully, further advances in seal design concepts can be made due to the results obtained via this numerical model.

The numerical model developed differs from previous models as the effects of mixed lubrication and surface roughness are investigated. Previously, the developed numerical models all made the basic assumptions of full film lubrication and smooth sealing surfaces. Experimental research over the years has shown that this is not a valid assumption to make, as mixed lubrication is present through part of the sealing zone and the seal roughness has an effect on the behavior of the seal (Kawahara, Ohtake, and Hirabayashi, 1981). Mixed lubrication is where asperity contact occurs between the seal and the rod, which tends to occur in these applications. Assuming the seal to be perfectly smooth is not realistic, as the surface is bound to have some sort of roughness which

plays a significant role in the lubrication for these reciprocating seals (Kanters and Visscher, 1988).

This model consists of three coupled analyses of fluid mechanics, deformation, and contact mechanics. The fluid mechanics portion deals with solving the Reynolds equation for the pressure distribution in the lubricating film between the seal and the rod, using a finite difference scheme. The deformation section addresses the deformation of the seal based on different sealed pressures, which is investigated using a FEA and influence coefficients. Additionally, the contact mechanics analysis deals with determining the contact pressure in the sealing zone. The three analyses determine the film thickness distribution in the sealing zone. The computer program couples these three analyses and converges to a final solution using relaxation techniques. After the computational process has converged, auxiliary calculations are performed on the results to obtain the quantities of leakage rate and friction force. Analysis can be performed on these obtained results which then allow the evaluation of the seal design. This analysis can lead to better seal designs with lower friction and less (or potentially no) leakage.

# **CHAPTER 1**

## **INTRODUCTION**

“Because leakage from the cylinder rod escapes to the environment, the reciprocating rod seal is one of the most critical elements in hydraulic equipment” (Müller and Nau, 1998). As a result, the goal of this project is to develop a numerical model for a reciprocating rod seal, including mixed lubrication and surface roughness that will be able to predict key seal performance characteristics, such as leakage and friction. Environmental concern regarding leakage from seals is a strong driver in the completion of this project. A leaky seal can have adverse effects on the environment, and thus yields a desire to design and use seals having little or no leakage produced. Additionally, a leaky seal can also cause problems for the application with respect to the operation and life. This numerical model will allow the evaluation of seal designs to predict the likelihood and amount of leakage for any set of characteristics of a particular seal.

Since 1964, important research has been performed in studying the operation of reciprocating seals beginning with Ishiwata and Kambayashi (1964) as well as O'Donogue and Lawrie (1964). Since that time many other studies have been performed, with limited results impacting the way seals are designed and selected. At the present time, only empirical means along with Finite Element Analysis (FEA) are used to predict the performance of seals during the design phase. Müller and Nau observed that “a seal that seals perfectly under static conditions can leak appreciably when the shaft reciprocates, because the dynamic sealing mechanism is quite different to that when static” (1998). Since the FEA does not allow for dynamic conditions to be simulated



within the seal, cost and time intensive experimental testing must be performed on the seal to determine the friction and whether or not the seal leaks.

However, this numerical model will be able to predict the leakage and friction within a sealing zone (the region where the elastomeric seal lip meets the rod), which will assist in reducing both cost and time of design.

In most previous numerical models two key assumptions stunt the usage of the results and they are the assumptions of full film lubrication in the sealing zone and a completely smooth seal. By assuming full film lubrication, it is implied that a continuous layer of lubricating film exists in between the seal and the rod throughout the entire operation. Experimental research over the years has been performed to show that these two assumptions are not valid, and the effects of both mixed lubrication and seal surface roughness must be considered (Kawahara, Ohtake, and Hirabayashi, 1981; Kanter and Visscher, 1988).

More recently, research has been performed taking into account the effects of mixed lubrication and surface roughness of the seal; however, these results are only obtained for a specific rectangular cross-sectioned elastomeric seal (Nikas, 2003; Nikas, 2004; Nikas and Sayles, 2004).

Based on the fact that most of the significant research in reciprocating rod seals has the two basic assumptions previously discussed, little impact has been made on the way that seals are designed. In order to have impact in this field, a numerical model must be developed that takes into consideration both the effects of mixed lubrication and of surface roughness of the sealing element. The numerical model developed for this project takes into consideration both of those ideas. Hopefully, this numerical model will

allow further insight into the physics of how the sealing zone functions. In the future, the further understanding of the seals produced through this numerical model will allow new and innovative seal concepts to be developed and evaluated. Ideally, the end result of the research for this project will assist in the creation of better functioning seals that could potentially one day have no leakage.

Further descriptions of the other background work performed on reciprocating rod seals that is relevant to the development of this numerical model is detailed in the following chapter. Chapter three outlines the methodology for creating this numerical model, while providing the equations used and how they were solved. Chapter four details the results obtained via the numerical model for both low and high pressure scenarios, and it also discusses the implications of the results and what impact they may have on the future design of seals. Chapter five chronicles the conclusions that can be drawn from this study and future work that can be performed to improve upon the numerical model as it stands today.

## **CHAPTER 2**

### **LITERATURE REVIEW**

Reciprocating seals have been researched upon since at least 1964 beginning with the works of Ishiwata and Kambayashi (1964) and O'Donogue and Lawrie (1964). Since that time, several modeling studies have been performed on the seals without yielding any significant results to affect the design process for seals. These previous numerical models have been created using two key assumptions. First, that there is full-film lubrication throughout the sealing zone. Second, the sealing surface is completely smooth. These models use a coupling of fluid mechanics and deformation analyses to obtain a prediction for the pressure and the leakage rates. These models use the Reynolds equation to govern the fluid mechanics of the sealing zone, which is a function of the film thickness and elasticity equations for the deformation of the seal.

Experimental results have shown that the assumption of full-film lubrication is not valid, as the results have shown that over a range of operating conditions mixed lubrication does occur. Additionally, the results obtained in other experiments show that a smooth surface for the seal is not a good approximation, and it becomes obvious that the roughness of the sealing element plays an important role in the performance of the seal and thus must be considered. Thus, the effects of assuming mixed lubrication and a surface roughness for the sealing element will be investigated in this project. A typical seal is shown below in Figure 1.

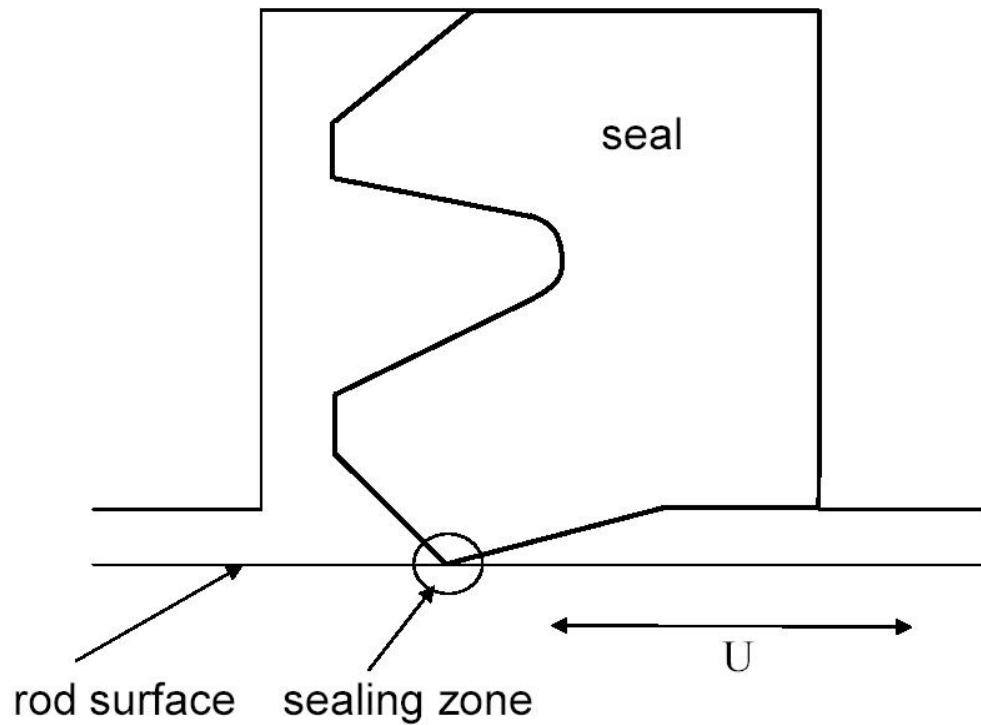


Figure 1: Typical seal configuration

## 2.1 Fluid Sealing Technology

Müller and Nau (1998) discuss the dynamic analysis of the sealing zone for a hydraulic seal. Based on a full-film lubrication model, Müller and Nau state that in order “to keep leakage low a seal is required to produce a contact pressure distribution with a steep slope at the inside and a low slope and the outside of the sealing contact.” As a result of the contact pressure distribution, no leakage will occur as long as the ratio of the outstroke rod speed to the contact pressure slope on the liquid side is less than the ratio of the instroke rod speed to the contact pressure slope on the air side. The conclusion that Müller and Nau (1998) have made regarding the design of the hydraulic seal is that in order “to minimize leakage, a rod seal should have a virtually triangular contact pressure

profile, with its maximum close to the fluid end of the contact.” The elastomeric U-cup seal shown in Figure 1 adheres with the design suggestion.

## **2.2 Initial Seal Studies using FEA**

The only significant tool used to evaluate the performance of seals is finite element analysis (FEA). The FEA can only provide a static structural analysis of the seal. Studies by Peng, Sun, and Albertson (1996) and Naderi, Albertson, and Peng (1994) have analyzed the performance of U-Cup hydraulic seals under static loading conditions and obtained frictional forces and see the stresses developed within the seals. A study by Claus (2002) discusses the development of a new heavy duty piston seal using FEA and the extensive testing needed to be performed to validate the seal design. These FEA results have helped designers over the years evaluate seals, but FEA is not an effective design tool as it does not show the seals response to dynamic conditions, which it will be operating under. Thus, a numerical model capable of simulating the dynamic conditions for the seal is necessary to further impact seal design and analysis.

## **2.3 Previous Numerical Models**

Over the years, several numerical models have been developed in an attempt to obtain the film thickness and pressure distributions to predict the leakage for hydraulic seals. Field and Nau (1974) develop a method for simultaneously solving the Reynolds equation and the elasticity equation using numerical techniques. Full film lubrication and a smooth sealing surface were assumed in the model for simplification of what proves to be a difficult mathematical problem to solve. These techniques proved to be very

computationally taxing and only outstroke results could be obtained. The results did show the strong impact of the rod speed on the overall leakage. Further studies were performed attempting different ways for mathematically solving the Reynolds equation and the elasticity equation using an iterative procedure by Ruskell (1980), Yang and Hughes (1983), and Prati and Strozzi (1984). Kanters, Verest, and Visscher (1990) and Müller and Nau (1998) assumed a hydrostatic pressure distribution and equated it to the static contact pressure distribution. A method of solving the Reynolds equation for the film thickness distribution was developed, yielding an expression used to obtain an estimate for the leakage of the seal during instroke and outstroke of the rod. The results from these numerical models were helpful, but experimental results would show issues involved in their development.

## **2.4 Previous Experimental Results**

Experimental results have been performed on these reciprocating rod seals, and several experiments have shown that basic assumptions of the initial numerical models are incorrect. The assumption of full film lubrication is shown to not be valid as the experimental results of Kawahara, Ohtake, and Hirabayashi (1981) has shown that over certain conditions asperity contact occurs between the seal and the rod leading to mixed lubrication in this region. The experimental work of Kanters and Visscher (1988) investigated the behavior of reciprocating seals and developed an accurate methodology for measuring leakage. Investigation of the results has shown that the seal cannot be approximated as smooth, because surface roughness of the seal affects the lubrication in the sealing zone and thus the leakage.

## **2.5 Recent Studies**

A numerical model has been developed recently that considers mixed lubrication and surface roughness effects, but only for rectangular cross-sectioned elastomeric seals (Nikas, 2003; Nikas and Sayles, 2004; Nikas, 2004). The results from the numerical model conclude that the sealed pressure and the stroking velocity vary the performance parameters of leakage rate, film thickness, and friction forces.

## **2.6 Pressure and Shear Flow Factors**

Patir and Cheng (1978, 1979) developed a study involving an average flow model for determining the effects of roughness on partial hydrodynamic lubrication. An average Reynolds equation was defined relative to pressure and shear flow factors, which are functions of the surface characteristics that are obtained from simulations. These obtained pressure and shear flow factors obtained by Patir and Cheng are used in the developed numerical model in the approximation of flow and the hydrodynamic pressure within the seal.

## CHAPTER 3

### METHODOLOGY

A numerical model has been created to predict the key seal performance parameters such as leakage and friction. This numerical model is potentially applicable to both elastomeric and non-elastomeric rod seals. For the scope of this project, only elastomeric seal results have been investigated such as the one shown in Figure 1. A 1-D model has been created to detail the sealing zone between the rod and the sealing element. Figure 2 shows the typical sealing zone used in previous numerical models, where both the seal and rod are assumed to be perfectly smooth.

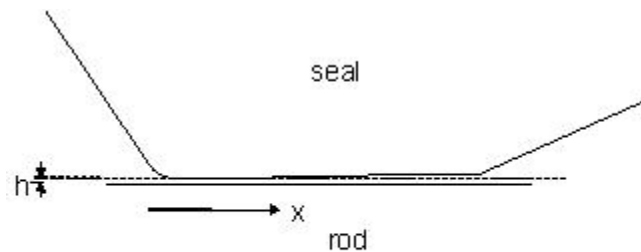


Figure 2: Sealing zone of previous numerical models

Previous experimental results have shown that the seal roughness plays an important role in how the seal functions and whether or not the seal will have leakage (Kanters and Visscher, 1988). Thus, the seal roughness has been taken into consideration in the creation and solution of this model, and its impact on the performance of the seal can be seen in the results. The sealing zone as used in this numerical model is shown below in Figure 3, where the rod is still assumed to be smooth but the seal has some roughness.



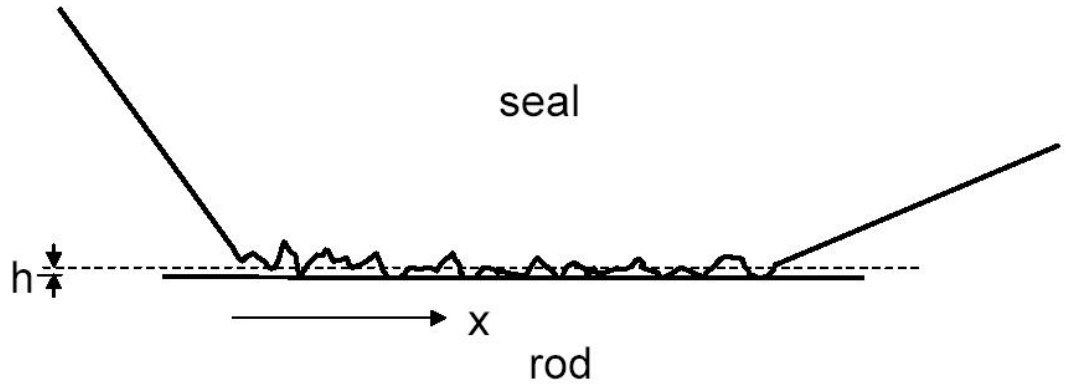


Figure 3: Sealing zone for new numerical model

Despite the film thickness,  $h$ , being shown as having a constant magnitude in Figure 3, the film thickness distribution is solved for using the numerical model and is a function of the  $x$ -direction.

In order to capture all of the effects that occur within the sealing zone of the seal, a coupling of three different analyses was necessary. These three coupled analyses are a fluid mechanics analysis, a contact mechanics analysis, and a deformation mechanics analysis. Details on the solution of these analyses will follow. Initial film thickness and pressure distributions are provided as inputs into the program by the user, and the three analyses are performed until complete convergence is arrived at.

Mesh convergence techniques were used to arrive at the appropriate number of nodes for the 1-D meshing of the sealing zone to be used, and as a result meshes of different densities were used for different sections of the numerical model. For the deformation analysis, a mesh containing 40 nodes provided accurate results. However, for the fluid mechanics and contact mechanics analysis 196 nodes were needed to provide accurate results. Interpolation techniques were used to go between the differing meshes

whenever necessary, as the mesh for the fluid mechanics and contact mechanics is five times denser than the mesh for the deformation analysis. Both full-film and mixed lubrication were taken into consideration, differing from previous numerical models that have only considered the full film lubrication.

### 3.1 Fluid Mechanics Analysis

The fluid mechanics of the sealing zone is governed by the Reynolds equation. The seal is axisymmetric and the film-thickness is considered to be small when compared to the seal radius, allowing the flow in the sealing zone to be modeled as one-dimensional using a Cartesian coordinate system. The effects of cavitation, where the fluid pressure is equal to zero, are potentially present in portions of the sealing zone, and thus a form of the Reynolds equation that includes cavitation and its effects is used. This form of the steady state Reynolds equation is derived from the Navier-Stokes and continuity equations and is shown in dimensionless terms in Equation 1,

$$\frac{d}{d\hat{x}} \left[ \phi_{xx} H^3 e^{-\hat{\alpha} F \phi} \frac{dF\phi}{d\hat{x}} \right] = 6\zeta \left[ \frac{d}{d\hat{x}} \{ [1 + (1 - F)\phi] H_T \} + F \frac{d\phi_{s.c.x.}}{d\hat{x}} \right] \quad (1)$$

where  $\phi$  is the fluid pressure/density function,  $H$  is the dimensionless film thickness, and  $\zeta$  is the dimensionless rod velocity,  $F$  is the cavitation index (see Section 3.1.2), and  $H_T$  is the truncated film thickness (see Section 3.1.3).  $\phi_{xx}$  and  $\phi_s$  are the flow factors that account for the effects of the surface roughness on the seal lip surface. These flow factors are functions of the ratio of the film thickness to the roughness amplitude and the roughness geometry (aspect ratio and orientation of the asperities). These flow factors are computed numerically using equations derived and outlined by Patir and Cheng (1978, 1979). The derivation of the values for the flow factors is detailed in Section 3.1.5.

Equation 1 is solved for  $\phi$  based on techniques outlined by Patankar (1980) which are further discussed in Section 3.1.1.

### **3.1.1 Numerical Scheme - Discretization of the Reynolds Equation**

A closed form solution for the Reynolds equation is not obtainable. Thus, in order to solve it a numerical finite difference scheme is implemented. A standard Gaussian elimination algorithm could be implemented and be used to solve the Reynolds equation, but another method is more efficient, due to the simplicity of the equations. Equation 1 is solved for the fluid pressure/density function,  $\phi$ , using a finite difference scheme known as the tri-diagonal matrix algorithm, for given  $H$  and  $\Phi_{xx}$ . The method for implementing this finite difference scheme is outlined by Patankar (1980). An analogous form of solving a basic 1-D heat conduction problem is solved by Patankar (1980), and the methodology is followed in this numerical model, however applying the presented techniques to solving Equation 1. The basic process presented by Patankar (1980) includes a discretization of the domain, a control-volume formulation, basic boundary condition assumptions, followed by a solution of a set of linear algebraic equations using a technique known as the tri-diagonal matrix algorithm or simply TDMA. TDMA refers to a matrix in which all of the nonzero values are located along the three main diagonals of the matrix; this is based upon the discretization of the domain. Details of the way the TDMA operates are not crucial to the understanding of the model, but they are presented in Appendix A. By applying these techniques, the Reynolds equation is solved for  $\phi$  and a pressure distribution is obtained.

In order to use the TDMA procedure, a discretization of the domain and a finite difference scheme must be used such that the equations will have the form required by TDMA. The finite difference scheme begins with the Reynolds equation as is shown in Equation 1. Equation 1 is discretized according to the layout shown in Figure 4.

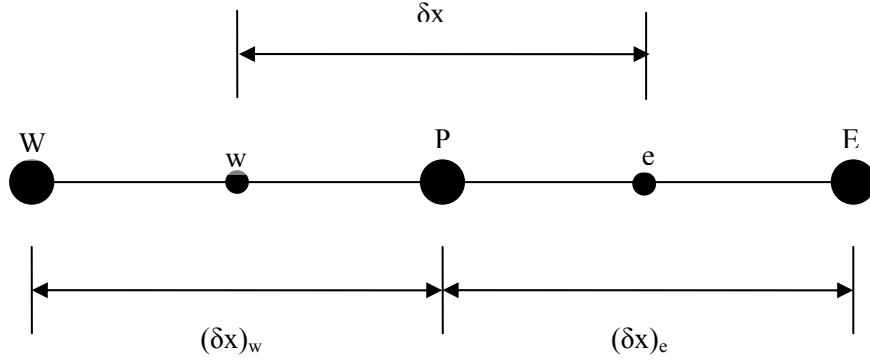


Figure 4: Diagram of control volume for discretization process

A micro control volume scheme is implemented for finite differencing the equations to be solved. This micro control volume scheme uses the e and w nodes, which are defined as being located at the midpoint between the W and P and E and P nodes respectively, as shown in Figure 4. The micro control volume scheme for solving the finite difference equations for the 1-D reciprocating rod seal equation with cavitation uses an algebraic mean is used to calculate the average truncated film thickness for the two nodes, as shown below in Equations 2 and 3.

$$H_e = \frac{(\bar{H}_T(I) + \bar{H}_T(I+1))}{2} \quad (2)$$

$$H_w = \frac{(\bar{H}_T(I) + \bar{H}_T(I-1))}{2} \quad (3)$$

The first step in the discretization is to move all of the terms to one side making the equation homogeneous. For simplification as done by both Patankar (1980) and

Payvar and Salant (1992), a substitution of a variable  $K$  is performed as shown in Equation 4.

$$K = \phi_{xx} H^3 \exp(-\hat{\alpha} F \phi) \quad (4)$$

Application of this substitution to Equation 1 yields the form of the Reynolds equation shown in Equation 5.

$$\frac{d}{d\hat{x}} \left[ K \frac{d}{d\hat{x}} (F\phi) \right] - 6\zeta \frac{d}{d\hat{x}} [\{1 + (1-F)\phi\} \cdot H_T] - 6\zeta F \frac{d\phi_{s.c.x.}}{d\hat{x}} = 0 \quad (5)$$

Integrating Equation 5 over the control volume from  $x_w$  to  $x_e$  yields the following:

$$\int_{x_w}^{x_e} \frac{d}{d\hat{x}} \left[ K \frac{d}{d\hat{x}} (F\phi) \right] d\hat{x} - \int_{x_w}^{x_e} 6\zeta \frac{d}{d\hat{x}} [\{1 + (1-F)\phi\} \cdot H_T] d\hat{x} - \int_{x_w}^{x_e} 6\zeta F \frac{d\phi_{s.c.x.}}{d\hat{x}} d\hat{x} = 0 \quad (6)$$

Now,

$$\int_{x_w}^{x_e} \frac{d}{d\hat{x}} \left[ K \frac{d}{d\hat{x}} (F\phi) \right] d\hat{x} = \left( K \frac{d}{d\hat{x}} (F\phi) \right)_e - \left( K \frac{d}{d\hat{x}} (F\phi) \right)_w \quad (7)$$

Approximating the derivative with finite differences gives

$$\left( K \frac{d}{d\hat{x}} (F\phi) \right)_e - \left( K \frac{d}{d\hat{x}} (F\phi) \right)_w = K_e \frac{F_E \phi_E - F_P \phi_P}{\delta \hat{x}_e} - K_w \frac{F_P \phi_P - F_W \phi_W}{\delta \hat{x}_w} \quad (8)$$

where Equations 9 and 10 define  $K_e$  and  $K_w$  using the harmonic mean, respectively.

$$K_e = \frac{2 \cdot K_E \cdot K_P}{(K_E + K_P) \cdot \Delta \hat{x}} \quad (9)$$

$$K_w = \frac{2 \cdot K_W \cdot K_P}{(K_W + K_P) \cdot \Delta \hat{x}} \quad (10)$$

Similarly,

$$\int_{x_w}^{x_e} 6\zeta \frac{d}{d\hat{x}} [\{1 + (1-F)\phi\} \cdot H_T] d\hat{x} = 6\zeta \{ ([1 + (1-F)\phi] \cdot H_T)_e - ([1 + (1-F)\phi] \cdot H_T)_w \} \quad (11)$$

where  $F$  and  $\phi$ , are defined using an arithmetic mean and  $(H_T)_e$  and  $(H_T)_w$  are defined by,

$$(H_T)_e = \left( \frac{(H_T)_P + (H_T)_E}{2} \right) \quad (12)$$

$$(H_T)_w = \left( \frac{(H_T)_P + (H_T)_W}{2} \right) \quad (13)$$

An “upwind” scheme is applied to Equation 11, where the scheme is dependent on the direction of flow (Patankar, 1980). For flow in a positive x-direction, the second term is defined by,

$$\int_{x_w}^{x_e} 6\zeta \frac{d}{d\hat{x}} \left[ \{1 + (1 - F)\phi\} \cdot H_T \right] d\hat{x} = 6\zeta \left\{ [1 + (1 - F_P)\phi_P] \cdot (H_T)_e - [1 + (1 - F_W)\phi_W] \cdot (H_T)_w \right\} \quad (14)$$

For flow in a negative x-direction, the second term is defined by,

$$\int_{x_w}^{x_e} 6\zeta \frac{d}{d\hat{x}} \left[ \{1 + (1 - F)\phi\} \cdot H_T \right] d\hat{x} = 6\zeta \left\{ [1 + (1 - F_E)\phi_E] \cdot (H_T)_e - [1 + (1 - F_P)\phi_P] \cdot (H_T)_w \right\} \quad (15)$$

By grouping similar terms from the simplification of the finite difference equations and applying a harmonic mean for the flow factors, the third term becomes,

$$\int_{x_w}^{x_e} 6\zeta F \frac{d\phi_{s.c.x.}}{d\hat{x}} d\hat{x} = 6\zeta \cdot F_P \left[ \left( \frac{2 \cdot (\phi_{s.c.x.})_P \cdot (\phi_{s.c.x.})_E}{(\phi_{s.c.x.})_P + (\phi_{s.c.x.})_E} \right) - \left( \frac{2 \cdot (\phi_{s.c.x.})_P \cdot (\phi_{s.c.x.})_W}{(\phi_{s.c.x.})_P + (\phi_{s.c.x.})_W} \right) \right] \quad (16)$$

Equations 8, 14 or 15, and 16 are substituted back into Equation 6. The terms can then be grouped according to the nodal locations of the  $\phi$  as shown in Equation 17.

$$A_P \phi_P = A_E \phi_E + A_W \phi_W + b \quad (17)$$

where for a positive rod speed

$$\begin{aligned}
A_p &= (K_e + K_w)F_p + 6\zeta(1 - F_p)(H_T)_E \\
A_E &= K_e(F_E) \\
A_w &= K_w(F_w) \\
b &= -6\zeta \cdot H_E + 6\zeta \{ [1 + (1 - F_w)\phi_w](H_T)_w \} - \\
&\quad 6\zeta \cdot F_p \left[ \left( \frac{2 \cdot (\phi_{s.c.x.})_p \cdot (\phi_{s.c.x.})_E}{(\phi_{s.c.x.})_p + (\phi_{s.c.x.})_E} \right) - \left( \frac{2 \cdot (\phi_{s.c.x.})_p \cdot (\phi_{s.c.x.})_w}{(\phi_{s.c.x.})_p + (\phi_{s.c.x.})_w} \right) \right]
\end{aligned}$$

and for a negative rod speed

$$\begin{aligned}
A_p &= (K_e + K_w)F_p + 6\zeta(1 - F_p)(H_T)_w \\
A_E &= K_e(F_E) \\
A_w &= K_w(F_w) \\
b &= 6\zeta \cdot H_w - 6\zeta \{ [1 + (1 - F_E)\phi_E](H_T)_E \} - \\
&\quad 6\zeta \cdot F_p \left[ \left( \frac{2 \cdot (\phi_{s.c.x.})_p \cdot (\phi_{s.c.x.})_E}{(\phi_{s.c.x.})_p + (\phi_{s.c.x.})_E} \right) - \left( \frac{2 \cdot (\phi_{s.c.x.})_p \cdot (\phi_{s.c.x.})_w}{(\phi_{s.c.x.})_p + (\phi_{s.c.x.})_w} \right) \right]
\end{aligned}$$

The discretization is applied to the linear equations that are to be solved using the TDMA technique on Equation 18.

$$A_i \phi_i = B_i \phi_{i+1} + C_i \phi_{i-1} + D_i \quad (18)$$

where  $A_i$ ,  $B_i$ ,  $C_i$ , and  $D_i$  are defined for a positive speed by,

$$\begin{aligned}
A_i &= \left( \frac{2 \cdot K_{i+1} \cdot K_i}{K_{i+1} + K_i} + \frac{2 \cdot K_{i-1} \cdot K_i}{K_{i-1} + K_i} \right) \cdot F_i + 6\zeta(1 - F_i)(H_T)_{i+1} \\
B_i &= \left( \frac{2 \cdot K_{i+1} \cdot K_i}{K_{i+1} + K_i} \right) \cdot F_{i+1} \\
C_i &= \left( \frac{2 \cdot K_{i-1} \cdot K_i}{K_{i-1} + K_i} \right) \cdot F_{i-1} \\
D_i &= -6\zeta \cdot H_{i+1} + 6\zeta \{ [1 + (1 - F_{i-1})\phi_{i-1}](H_T)_{i-1} \} \\
&\quad - 6\zeta \cdot F_p \left[ \left( \frac{2 \cdot (\phi_{s.c.x.})_i \cdot (\phi_{s.c.x.})_{i+1}}{(\phi_{s.c.x.})_i + (\phi_{s.c.x.})_{i+1}} \right) - \left( \frac{2 \cdot (\phi_{s.c.x.})_i \cdot (\phi_{s.c.x.})_{i-1}}{(\phi_{s.c.x.})_i + (\phi_{s.c.x.})_{i-1}} \right) \right]
\end{aligned}$$

and for a negative speed by,

$$\begin{aligned}
A_i &= \left( \frac{2 \cdot K_{i+1} \cdot K_i}{K_{i+1} + K_i} + \frac{2 \cdot K_{i-1} \cdot K_i}{K_{i-1} + K_i} \right) \cdot F_i + 6\zeta(1 - F_i)(H_T)_{i-1} \\
B_i &= \left( \frac{2 \cdot K_{i+1} \cdot K_i}{K_{i+1} + K_i} \right) \cdot F_{i+1} \\
C_i &= \left( \frac{2 \cdot K_{i-1} \cdot K_i}{K_{i-1} + K_i} \right) \cdot F_{i-1} \\
D_i &= 6\zeta \cdot H_{i-1} - 6\zeta \{ [1 + (1 - F_{i+1})\phi_{i+1}](H_T)_{i+1} \} \\
&\quad - 6\zeta \cdot F_P \left[ \left( \frac{2 \cdot (\phi_{s.c.x.})_i \cdot (\phi_{s.c.x.})_{i+1}}{(\phi_{s.c.x.})_i + (\phi_{s.c.x.})_{i+1}} \right) - \left( \frac{2 \cdot (\phi_{s.c.x.})_i \cdot (\phi_{s.c.x.})_{i-1}}{(\phi_{s.c.x.})_i + (\phi_{s.c.x.})_{i-1}} \right) \right]
\end{aligned}$$

The TDMA procedure as detailed in Appendix A is applied to this set of equations to obtain the pressure distribution within the sealing zone.

### 3.1.2 Cavitation Effects

In order to account for the effects of cavitation, a technique is used for which a single differential equation, Equation 1, uses a single variable,  $\phi$ , to obtain the correct form of the equation for the different regions of the sealing zone. The  $\phi$  is defined as the dimensionless pressure in the liquid region and is related to the average density in the cavitated region. Pavyar and Salant (1992) define a method that enables  $F$  to act as a switch between two different forms derived from Equation 1. In the full-film lubrication region, application of the conditions found in Equation 19 below to Equation 1 reduces Equation 1 to the Reynolds equation. For the cavitation region, Equation 20 below is used to modify Equation 1 to the form of the continuity equation.

In the liquid region of the sealing zone,

$$\phi \geq 0 \quad F = 1 \text{ and } P = \phi \tag{19}$$

and in the cavitated region,



$$\phi < 0 \quad F = 0 \quad \text{and} \quad P = 0, \quad \hat{\rho} = 1 + \phi \quad (20)$$

where the boundary conditions are  $P = P_{sealed}$  at  $\hat{x} = 0$  and  $P = 1$  at  $\hat{x} = 1$ .

After applying Equations 19 and 20 to the computed  $\phi$  distribution, appropriate results are obtained for the pressure distribution for the fluid mechanics section via the Reynolds equation.

### 3.1.3 Additional Assumptions

For usage in the model, the film thickness distribution must be calculated. The average truncated film thickness is given by (Patir and Cheng, 1978, 1979),

$$H_T = \int_{-H}^{\infty} [H + \delta] F(\delta) d\delta \quad (21)$$

In this numerical model, a Gaussian distribution is used to describe the film thickness profile in the sealing zone,

$$F(\delta) = \frac{1}{\sqrt{2\pi}} e^{\left(-\frac{\delta^2}{2}\right)} \quad (22)$$

Then, Equation 22 is substituted into Equation 21 and is integrated to obtain the result shown in Equation 23 for the average truncated film thickness.

$$H_T = \frac{H}{2} + \frac{H}{2} \operatorname{erf}\left(\frac{H}{\sqrt{2}}\right) + \frac{1}{\sqrt{2\pi}} e^{\left(-\frac{H^2}{2}\right)} \quad (23)$$

For the purposes of this project, the viscosity of the fluid is assumed to be pressure dependent. Equation 24 illustrates that dependence.

$$\mu = \mu_0 \exp(\hat{\alpha} F \phi) \quad (24)$$

### 3.1.4 Auxiliary Calculations

The coupled fluid mechanics, contact mechanics, and deformation analyses are iterated within the computer program until convergence is reached, which usually takes several minutes. Additional auxiliary calculations are performed to obtain the flow rate or total leakage through the film and the shear stress (friction force) exerted by the fluid on the seal.

The instantaneous leakage rate per unit circumferential length in the film is derived from the Navier-Stokes equations and can be calculated according to Equation 25.

$$\hat{q} = -\phi_{xx} e^{-\hat{\alpha} F \phi} H^3 \frac{dF\phi}{d\hat{x}} + 6\zeta \{ [1 + (1 - F)\phi] H_T + F\phi_{s.c.x.} \} \quad (25)$$

The viscous shear stress on the rod can be obtained using the methods provided by Patir and Cheng (1979) which has been applied to this numerical model and the resulting equation is shown below in Equation 26.

$$\hat{\tau}_{avg} = \frac{\tau_{avg}}{E} = \frac{-\hat{\sigma}}{\xi} e^{-\hat{\alpha} F \phi} \frac{\zeta}{H} (\phi_f - \phi_{fss}) - \phi_{fpp} \frac{\hat{\sigma}}{\xi} \frac{H}{2} \frac{dF\phi}{d\hat{x}} \quad (26)$$

### 3.1.5 Flow Factors

Patir and Cheng (1978, 1979) outline results obtained regarding different pressure and shear flow factors, and their results are implemented in the numerical model as parameters for the Reynolds equation.  $\phi_{xx}$  is a pressure flow factor, where  $\phi_{xx}$  compares the average pressure flow in a rough bearing to that of a smooth bearing.  $\phi_{s.c.x.}$  is a shear flow factor that represents additional flow transport due to sliding in a rough bearing. Patir and Cheng (1978) obtained  $\phi_{xx}$  and  $\phi_{s.c.x.}$  through flow simulations. Patir and Cheng did a series of numerical experiments in which the Reynolds equation containing the local film thickness was solved for a variety of randomly generated roughness

patterns, and ensemble averages were obtained. Based on their findings, the values for  $\phi_{xx}$  to be used in the numerical model are calculated using Equation 27 or 28.

For  $\gamma \leq 1$ ,

$$\phi_{xx} = 1 - Ce^{-rH} \quad (27)$$

For  $\gamma > 1$ ,

$$\phi_{xx} = 1 + CH^{-r} \quad (28)$$

The equation to be selected is dependent on the value for  $\gamma$ , which is a parameter that describes the geometry of the contacting asperities. Equations 27 and 28 contain parameters  $C$  and  $r$  for which values have been tabulated by Patir and Cheng (1979) and are shown in Table 1 for different values of  $\gamma$ .

Table 1: Coefficient values used to calculate  $\phi_{xx}$

$\gamma$	C	R
1/9	1.480	0.42
1/6	1.380	0.42
1/3	1.180	0.42
1	0.900	0.56
3	0.225	1.5
6	0.520	1.5
9	0.870	1.5

The value for  $\phi_{s.c.x.}$  is also found experimentally through a curve-fitting of results by Patir and Cheng (1979). The shear flow factor is a function of the film thickness and other roughness parameters. Equations 29 and 30, and the conditions for their usage, are shown below and they are used to obtain  $\phi_{s.c.x.}$ .

For  $H \leq 5$ ,

$$\phi_{s.c.x.} = A_1 H^{\alpha_1} e^{-\alpha_2 H + \alpha_3 H^2} \quad (29)$$

For  $H > 5$ ,

$$\phi_{s.c.x.} = A_2 e^{-0.25H} \quad (30)$$

The roughness parameters found in Equations 29 and 30 were tabulated by Patir and Cheng (1979) and are shown below in Table 2.

Table 2: Coefficients used in Equations 29 and 30

$\gamma$	$A_1$	$\alpha_1$	$\alpha_2$	$\alpha_3$	$A_2$
1/9	2.046	1.12	0.78	0.03	1.856
1/6	1.962	1.08	0.77	0.03	1.754
1/3	1.858	1.01	0.76	0.03	1.561
1	1.899	0.98	0.92	0.05	1.126
3	1.560	0.85	1.13	0.08	0.556
6	1.290	0.62	1.09	0.08	0.388
9	1.011	0.54	1.07	0.08	0.295

$\phi_{fp}$  is a correction factor for the mean pressure flow component of the shear stress, and it was also obtained via a simulation performed by Patir and Cheng (1979). The values for  $\phi_{fp}$  are calculated using Equation 31 where  $\phi_{fp}$  is only a function of the film thickness and other roughness parameters.

$$\phi_{fp} = 1 - D e^{-sH} \quad (31)$$

The roughness parameters found in Equation 31 are tabulated and shown in Table 3.

Table 3: Coefficients used in Equation 31

$\Gamma$	D	s
1/9	1.51	0.52
1/6	1.51	0.54
1/3	1.47	0.58
1	1.40	0.66
3	0.98	0.79
6	0.97	0.91
9	0.73	0.91

$\phi_{fs}$  is another correction term which is a results of the effects of roughness and sliding.

$\phi_{fs}$  is calculated using Equation 32 which is obtained via a fitting of data to obtain an empirical relationship which was performed by Patir and Cheng (1979).

$$\phi_{fs} = A_3 H^{\alpha_4} e^{-\alpha_5 H + \alpha_6 H^2} \quad (32)$$

Equation 32 is only a function of the film thickness and other roughness coefficients, which are tabulated in Table 4.

Table 4: Coefficients used in Equation 32

$\gamma$	$A_3$	$\alpha_4$	$\alpha_5$	$\alpha_6$
1/9	14.1	2.45	2.30	0.10
1/6	13.4	2.42	2.30	0.10
1/3	12.3	2.32	2.30	0.10
1	11.1	2.31	2.38	0.11
3	9.8	2.25	2.80	0.18
6	10.1	2.25	2.90	0.18
9	8.7	2.15	2.97	0.18

$\phi_f$  is a term that comes about due to an averaging of the sliding velocity component of the shear stress, which is obtained through integration for any given frequency density of roughness heights. Patir and Cheng (1979) obtain an analytical expression for  $\phi_f$  that is sufficient for numerical calculations.  $\phi_f$  is defined by Equations 33 and 34 which is a function of the film thickness and roughness.

For  $H \leq 3$ ,

$$\phi_f = \frac{35}{32} z \left\{ \left( 1 - z^2 \right)^3 \ln \left( \frac{z+1}{\varepsilon^*} \right) + \frac{1}{60} \left[ -55 + z(132 + z(345 + z(-160 + z(-405 + z(60 + 147z)))) \right] \right\} \quad (33)$$

For  $H > 3$ ,

$$\phi_f = \frac{35}{32} z \left\{ (1 - z^2)^3 \ln \left( \frac{z+1}{z-1} \right) + \frac{z}{15} [66 + z^2 (30z^2 - 80)] \right\} \quad (34)$$

where

$$H = h / \sigma \quad z = H / 3 \quad \varepsilon^* = \varepsilon / (3\sigma)$$

### 3.2 Deformation - FEA for Influence Coefficients

The function of the deformation analysis is to obtain the film thickness distribution by computing the radial deformation of the sealing element, which is obtained using the influence coefficient method. The influence coefficient method takes into consideration the effects of the forces at all nodes on the deformation at a given node.  $(I_1)_{ik}$  represents the deformation at node i produced by a unit pressure at node k, and is termed the “influence coefficient.”

The film thickness at the ith node can be obtained from,

$$H_i = H_s + \sum_{k=1}^n (I_1)_{ik} (P_t - P_{sc})_k \quad (35)$$

where  $H_s$  is the static film thickness,  $P_t$  is the total pressure, and  $P_{sc}$  is the static contact pressure.  $P_t$ , the total pressure in the deformation analysis, is defined as,

$$P_t = P_c + P \frac{P_a}{E} \quad (36)$$

which shows that the total pressure is equal to the sum of the contact pressure at the node and the fluid pressure nondimensionalized relative to the Young's Modulus which is the same nondimensionalization as for the contact pressure.

The static film thickness,  $H_s$ , used in Equation 35 is obtained via a model presented by Streator (2001) and is shown in Equation 37.

$$H_s = -1.0641 + \sqrt{(3.6305 - 5.0684 \log_{10} I)} \quad (37)$$

where the parameter,  $I$ , is defined by,

$$I = \frac{P_{sc}}{\frac{4}{3} \frac{1}{(1-\nu^2)} \sigma^{3/2}} \quad (38)$$

Finite Element Analysis (FEA) was implemented in order to obtain the influence coefficients and the static contact pressure curve for the sealed pressures, which are both necessities for the numerical model. These results were obtained offline and introduced into the numerical model as inputs rather than being integrated within the model. The commercial software package ANSYS was used to obtain these influence coefficients and static contact pressure curve. The geometry for the rod, seal, and housing were created in ANSYS from precise measurements and the engineering drawing of the parts. An axisymmetric model for these parts was used to simplify the model and to save computation time. Appropriate material properties are then applied to the rod, housing, and seal. These geometries were then to be meshed. The mesh was created using element type PLANE82, which is a 2-D 8-node quadratic element with axisymmetric capabilities, for all of the geometries. The mesh was then refined in key areas where convergence issues could be a problem and to obtain detailed results in the sealing zone. A convergence study was performed to ensure accurate results, that as the mesh was refined further the results did not differ significantly from the previously obtained results. The meshing of the geometries for the model is shown in Figure 5.

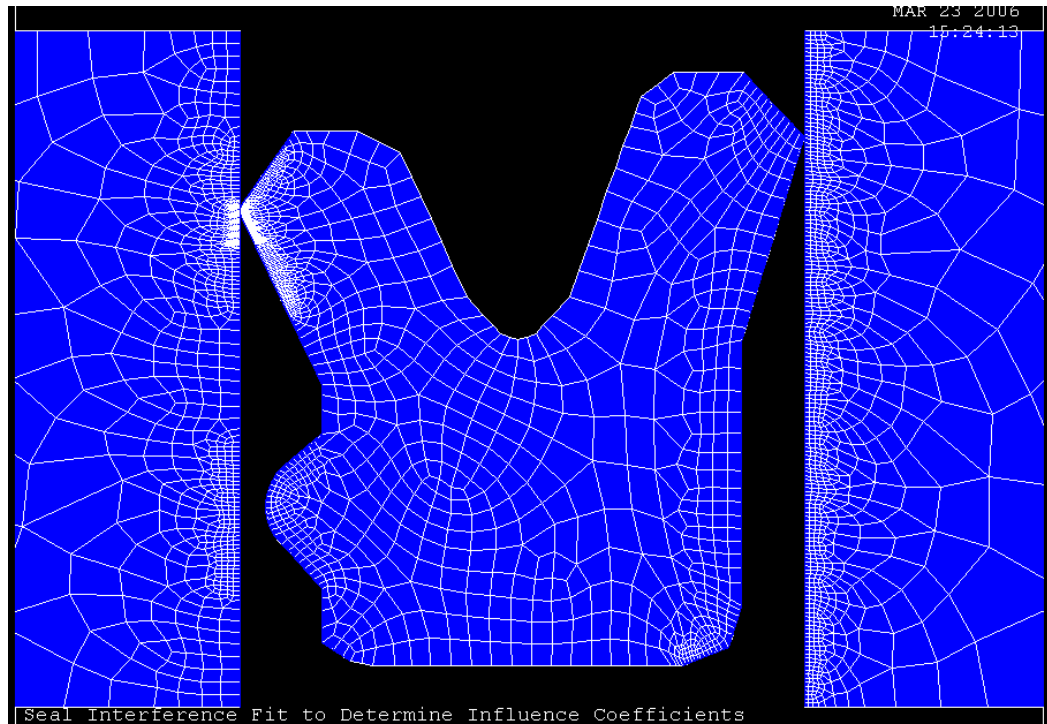


Figure 5: Meshing of geometries

Next, a contact model is implemented using elements CONTA172 and TARGE169 with a coefficient of friction of 0.25. The CONTA172 element was used to simulate the contact surfaces as it is a 2-D 3-node surface-to-surface element. The TARGE169 is a 2-D target element which is applied with the CONTA172 element. The coefficient of friction of 0.25 is a typical value for this type of application. These contact and target surfaces were applied anywhere in the geometry where contact between the seal and housing or seal and rod may occur. This process was performed via a trial and error methodology. A symmetric pair was created such that the contact is capable to deform all of the surfaces in the contacting regions; however, the significant deformation exists in the sealing element due to the fact that it has a much lower Young's Modulus and a higher Poisson's ratio.



A static analysis was performed for the interference fit between the seal and the housing and rod. This interference fit was performed by starting with the geometry of the rod, seal, and housing and applying a displacement to the rod in order to obtain the initial conditions for preloading the seal, as provided by the seal manufacturer. Due to the large amount of deformation for the interference fit with respect to the total dimensions of the seal, a series of ten equally spaced load steps was used to apply this total displacement. The reasoning behind this tactic is that it is needed for the interference fit due to convergence difficulties arising from the mesh density and the contact algorithm. Finally, varying amounts of pressure could be applied to the side of the seal sealing the pressure with atmospheric pressure being applied to the other side of the seal to obtain the necessary results. For the cases detailed in this project, 6.9 MPa (1000 psi) and 13.8 MPa (2000 psi) were applied separately as the sealed pressures. Figure 6 shows the deformed seal with the meshing.

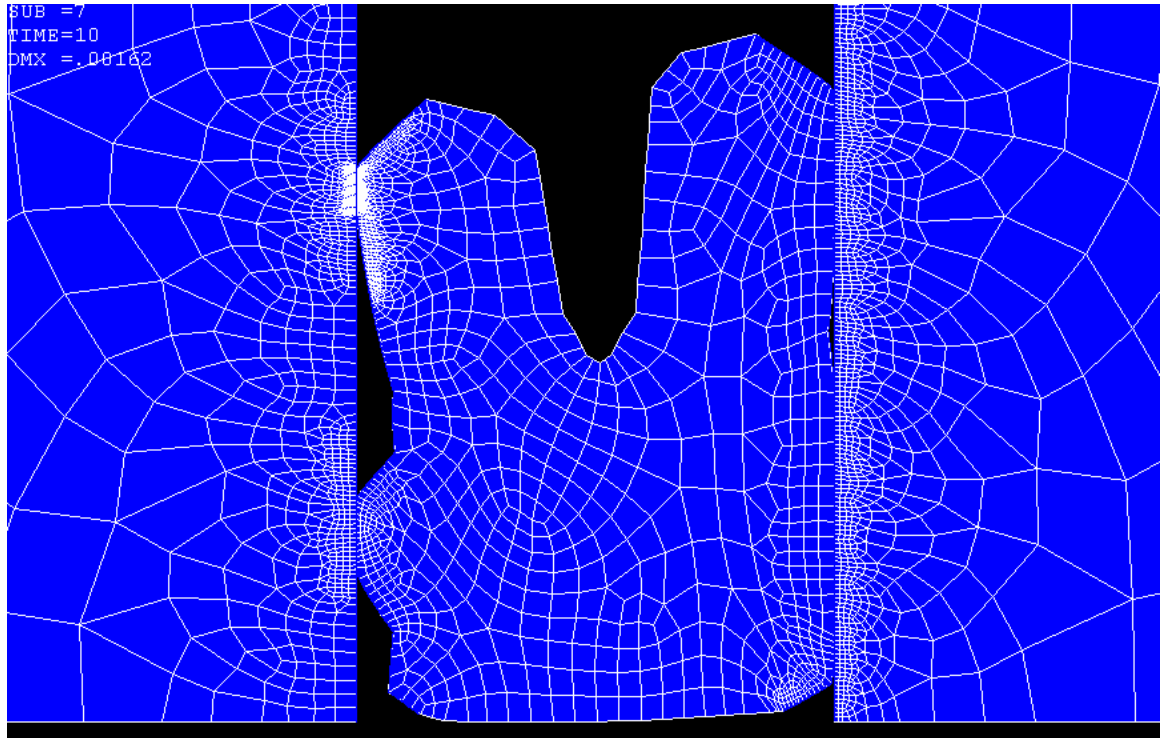


Figure 6: Deformed seal with meshing

From the results of the convergence study, forty points in contact were obtained within the sealing zone for which the static contact pressure and the influence coefficients are obtained. The static contact pressure at each of these forty nodes was extracted from ANSYS, and then a curve fit was applied to be used in the 196 nodes for the rest of the numerical model. Additionally, the influence coefficients were calculated. The method for obtaining these coefficients is as follows. For each node, a unit force was applied at that node and the displacements at all forty nodes were recorded. This process was repeated for all forty nodes. Thus, a 2-D matrix was created using the displacements at each node caused by a unit force at another node. Figure 7 shows a typical plot of the influence coefficients.

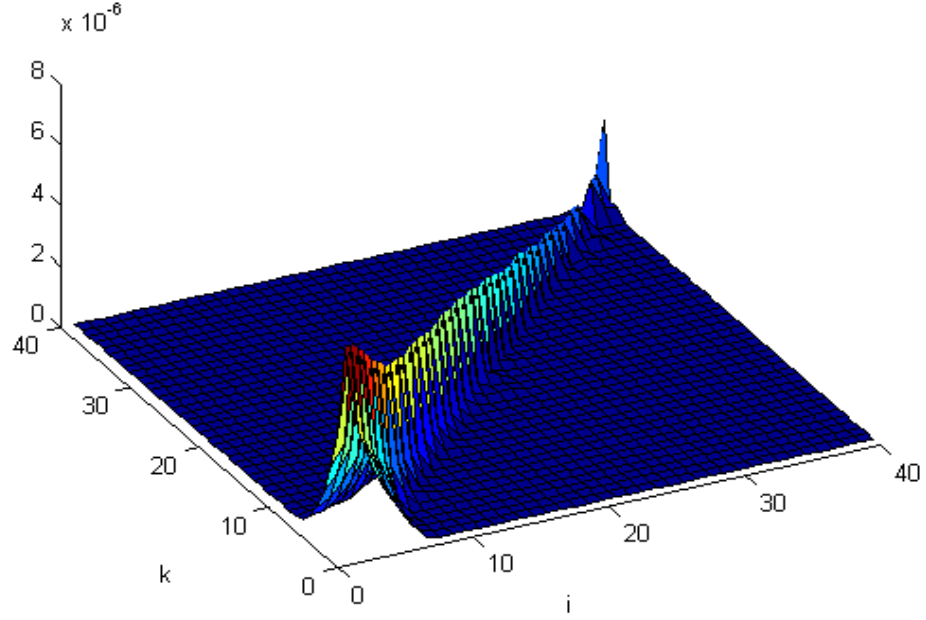


Figure 7: Influence coefficients for the deformation analysis

These obtained displacements were then related back to the dimensionless parameters used in the numerical model. Equation 39 shows the applied formula to convert the results for the influence coefficients obtained from ANSYS into the actual influence coefficients to be used in the numerical model in Equation 35,

$$I_l = I_l^* \cdot P_{ref} \frac{\Delta x \cdot \pi \cdot D}{\sigma} \quad (39)$$

where  $I_l$  is the influence coefficients for the numerical model,  $I_l^*$  is the influence coefficients obtained via ANSYS,  $P_{ref}$  is a reference pressure of  $10^5$  bar,  $\Delta x$  is the nodal step size in the x-direction,  $D$  is the rod diameter, and  $\sigma$  is the rms roughness.

### 3.3 Contact Mechanics

The section of this analysis is performed if the film thickness indicates that asperities are in contact, and the criterion is that  $h/\sigma < 3$ . The contact mechanics is used to determine the contact pressure. In mixed lubrication, the contact pressure is added to the pressure obtained via the fluid mechanics analysis in order to compute both the film thickness and deformations. The contact pressure,  $P_c$ , is obtained from the Greenwood and Williamson model assuming a Gaussian distribution of asperities, which is shown in Equation 40.

$$P_c = \frac{4}{3} \frac{1}{(1-\nu^2)} \hat{\sigma}^2 \frac{1}{\sqrt{2\pi}} \int_H^\infty (\zeta - H)^{3/2} e^{-\frac{\zeta^2}{2}} d\zeta \quad (40)$$

where  $\nu$  is Poisson's ratio,  $\hat{\sigma}$  is the dimensionless roughness,  $H$  is the film thickness, and  $\zeta$  is a dummy variable of integration. Equation 40 is what is approximated by the model by Streater (2001) and led to Equation 37 in the deformation analysis.

The shear stress on the rod due to the contact can be solved for using Equation 41.

$$\hat{\tau}_c = -fP_c \left( \frac{\zeta}{|\zeta|} \right) \quad (41)$$

There is no analytical solution for obtaining the exact contact pressure as shown in Equation 40. Thus, Streater (2001) provides a curve fit for approximating these results in a reasonable manner. Equation 42 shows the integral that must be solved numerically.

$$I = \frac{1}{\sqrt{2\pi}} \int_H^\infty (\zeta - H)^{3/2} e^{-\frac{\zeta^2}{2}} d\zeta \quad (42)$$

The approximate solution for Equation 42 obtained by Streater (2001) is shown in Equation 43 and provides reasonably accurate results,

$$\log_{10}(I) = C_2 H^2 + C_1 H + C_0 \quad (43)$$

where  $C_2 = -0.1973$ ,  $C_1 = -0.4199$ , and  $C_0 = 0.4929$ . According to Streater (2001), the results for Equation 36 have maximum errors of 6 to 14% for  $H$  between 1 and 6, which is the range for this numerical model. Now that a method has been presented for obtaining a numerical solution, the integral in Equation 42 can be solved, and the contact pressures are obtained using Equation 40.

### 3.4 Program Details

The computational scheme for the numerical model is shown in Figure 8. The generated computer program requires several inputs from the user in order to obtain results for specified conditions. These necessary inputs are seal properties such as Young's Modulus and Poisson's ratio, fluid properties such as viscosity, and operating conditions such as rod speed and roughness values, as well as initial guesses of the film thickness (a uniform profile) and the cavitation index,  $F$ , (value of 1). The fluid mechanics analysis that was outlined previously is then performed to obtain the initial fluid pressure distribution based on the given parameters. An iteration loop is present within this fluid mechanics loop to converge on the results for pressure dependent viscosity and the cavitation index. Next, the contact mechanics analysis is performed to obtain the contact pressure distributions, and the deformation analysis is performed to yield the normal deformations. The film thickness distribution is updated and iteration resumes until the convergence criterion is satisfied for the film thickness.

For the fluid mechanics analysis to be considered converged, a parameter,  $\varepsilon_p$ , must obtain a value less than a given value of  $1 \times 10^{-4}$ . The parameter  $\varepsilon_p$  is defined as a

maximum relative difference of pressures between successive iterations as shown in Equation 44.

$$\varepsilon_p = \max_{all\ nodes} \left( \frac{|p_i - p_{i-1}|}{p_{i-1}} \right) \quad (44)$$

where  $i$  denotes the current iteration and  $i-1$  denotes the previous iteration.

For the contact mechanics and deformation analyses to be considered converged, a similar parameter,  $\varepsilon_h$ , must also achieve a value less than  $1 \times 10^{-4}$ . The parameter  $\varepsilon_h$  is a maximum relative difference of film thicknesses as shown in Equation 45.

$$\varepsilon_h = \max_{all\ nodes} \left( \frac{|h_i - h_{i-1}|}{h_{i-1}} \right) \quad (45)$$

where  $i$  denotes the current iteration and  $i-1$  denotes the previous iteration and  $\varepsilon_h$  is the maximum from all nodal results.

These iteration loops continue until both the fluid pressure and film thickness convergence criterion shown in Equations 44 and 45 are both satisfied simultaneously. Once complete convergence is obtained, auxiliary calculations for the flow rate (leakage) and frictional shear stress are performed to obtain the desired results from the numerical model.

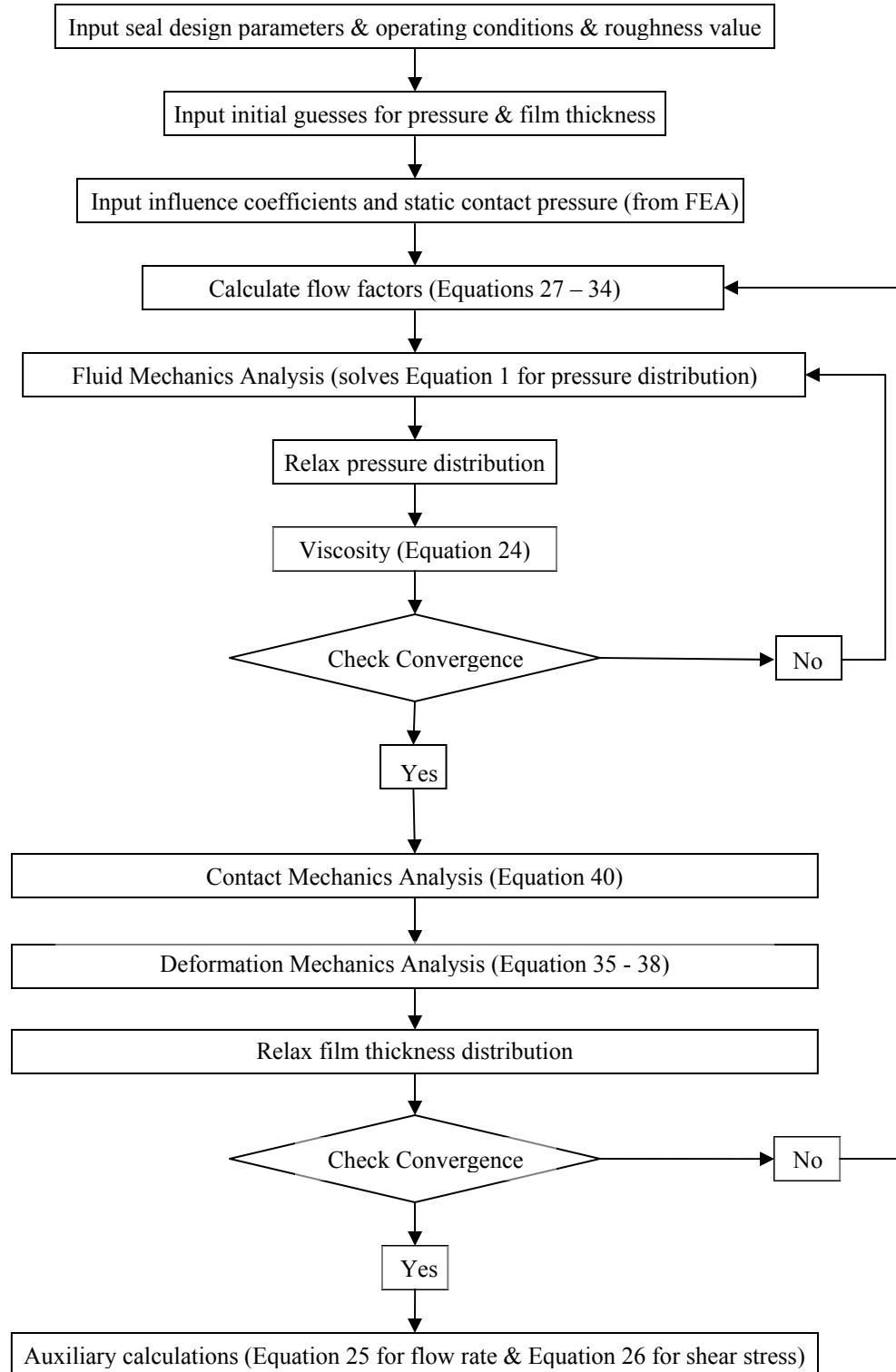


Figure 8: Computational scheme

## **CHAPTER 4**

### **RESULTS**

The numerical model for a reciprocating rod seal has been created according to the descriptions provided in Chapter 3. The seal that will serve as the base case for this numerical model is a Hallite seal used in an injection molding machine. This seal seals the hydraulic cylinder that is used to open and close the mold. The rod and housing surrounding the seal are comprised of steel and thus the material properties are a Young's Modulus of 210 GPa and a Poisson's ratio of 0.29. The Hallite seal is an elastomer with material properties of a Young's Modulus of 43 MPa and a Poisson's ratio of 0.49. Several cases for different operating conditions for this seal have been simulated using different input parameters, and results are provided throughout this chapter.

#### **4.1 Dimensionless Results for 6.9 MPa Sealed Pressure**

Operating parameters and specifications were provided for the seal and these values were used as base case parameters for the seal testing according to the numerical model and program. The base parameters for which computations have been performed for this typical hydraulic rod seal are shown in Table 5. The asperity radius and asperity density were selected based on observations of somewhat similar seals.

The first set of results to be investigated is dimensionless results for a sealed pressure of 6.9 MPa (1000 psi).



Table 5: Base seal parameters

		Dimensionless
Elastic modulus, $E$	$43 \times 10^6$ Pa	
Poisson's ratio, $\nu$	0.49	
Sealed pressure, $p_{sealed}$	6.90 MPa (1000 psi)	
Rod diameter, $D$	88.9 mm (3.5")	
Stroke	1.93 m (76")	
Speed – outstroke, $U$	0.635 m/s (25 in/s)	973
Speed – instroke, $-U$	0.813 m/s (32 in/s)	1245
Reference viscosity, $\mu_0$	0.043 Pa-s	
Pressure-viscosity coefficient, $\alpha$	$20 \times 10^{-9}$ Pa $^{-1}$	$20 \times 10^{-4}$
Asperity radius, $R$	1 $\mu$ m	$6.401 \times 10^4$
RMS roughness, $\sigma$	0.3 $\mu$ m	1.392
Asperity density, $\eta$	$10^{13}$ m $^{-2}$	
Sealing zone length, $L$	0.321 mm	
Asperity contact friction coefficient, $f$	0.25	
Aspect ratio, $\gamma$	1	

Using the base case parameters, the film thickness distribution was obtained within the sealing zone. When investigating film thickness results, the key value for the magnitude is  $3\sigma$  for dimensional results or 3 for dimensionless results. For values of film thickness larger than this key value, full film lubrication would be indicated. Whereas for lower values of film thickness than this key value, mixed lubrication would be present as asperity contact would occur. The results for the film thickness for the first case are shown below in Figure 9 for both the outstroke and instroke of the rod.

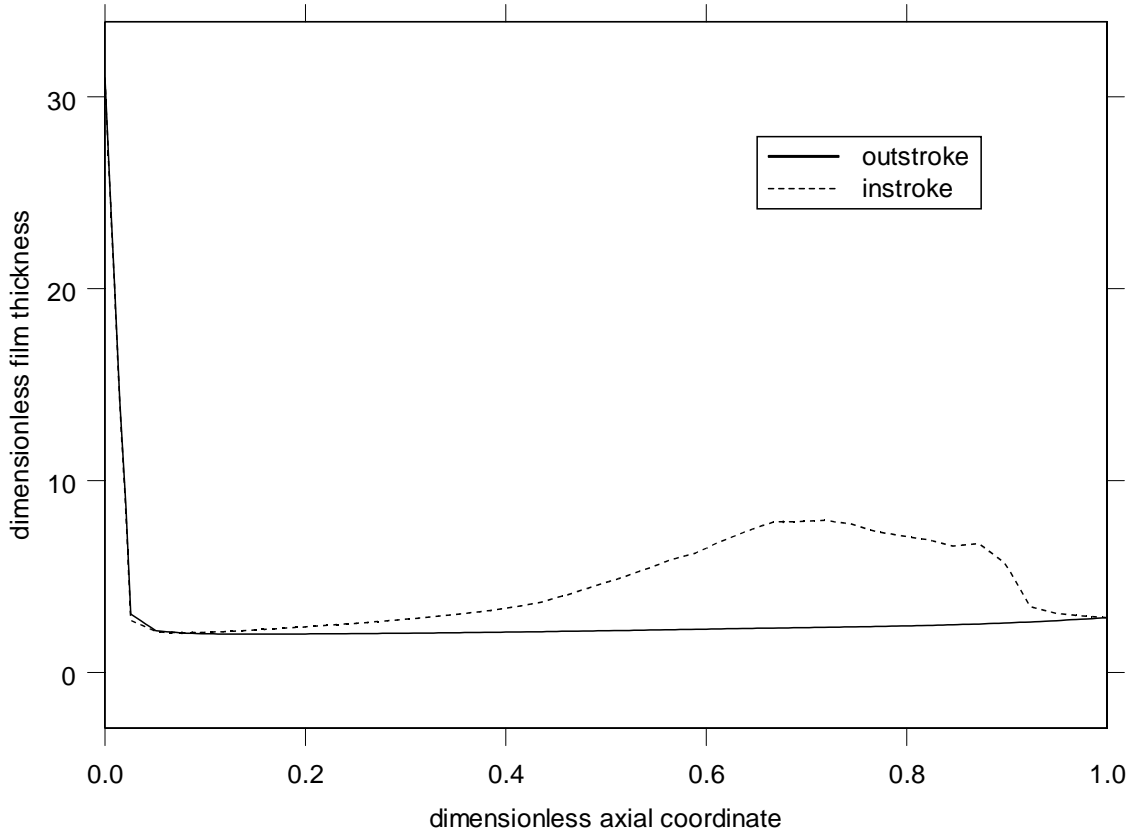


Figure 9: Film thickness distributions, base case

Figure 9 shows that for the outstroke of the rod, the film thickness has a dimensionless value of less than 3 (as contact exists when  $h/\sigma \leq 3$ ) through almost the entire sealing zone, indicating mixed lubrication. Figure 9 reveals that for the instroke of the rod, the film thickness is less than 3 for about one-third of the sealing zone in the region located near the high pressure end. Once again, this result characterizes mixed lubrication in this region. Throughout the remainder of the sealing zone, the film thickness is larger than 3, which implies that full film lubrication exists in this region.

Pressure curves are also generated based on the results for the fluid pressure, contact pressure, and static contact pressure. A key observation to be made is that cavitation is present if the fluid pressure has a value of zero. Additionally if the contact pressure is zero, the presence of full film lubrication is noted. The fluid pressure, contact pressure, and the static contact pressure distributions in the sealing zone for the base case parameters and the outstroke of the rod are shown below in Figure 10.

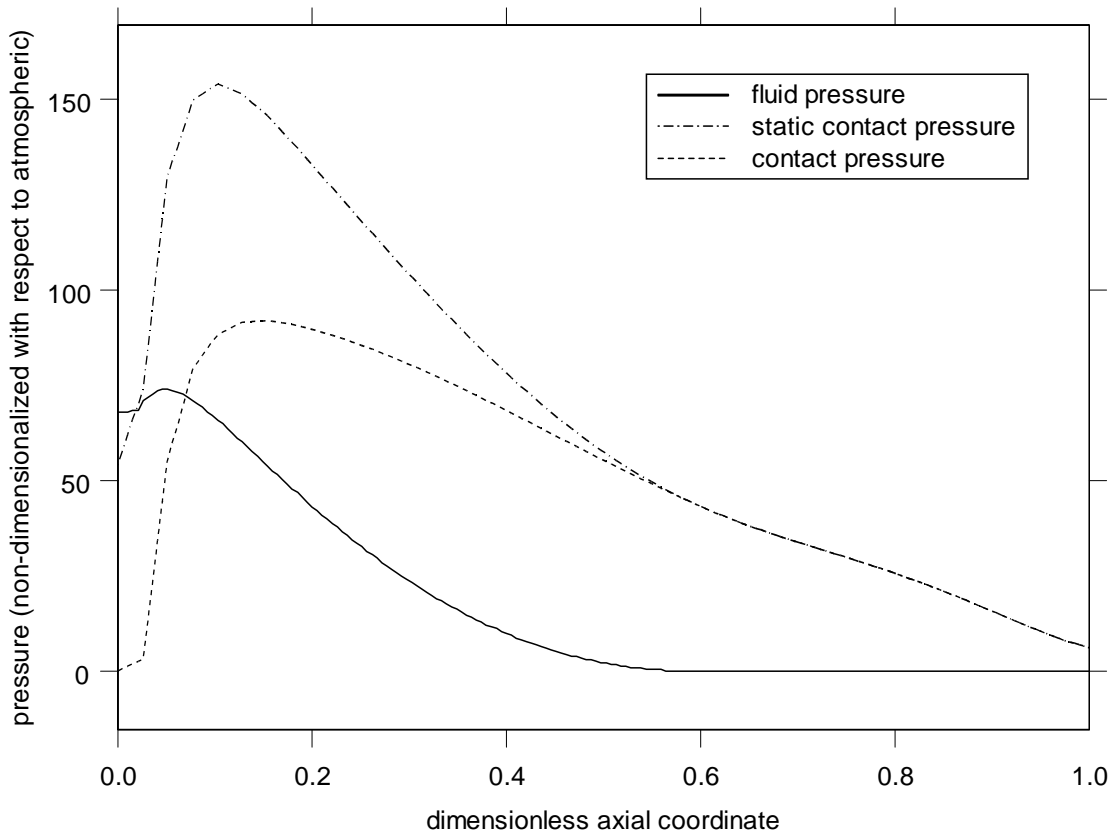


Figure 10: Pressure distributions, base case, outstroke

The results in Figure 10 for the pressure distributions agree well with the film thickness results of Figure 9. Hydrodynamic fluid pressure generation is present over the

first half of the sealing zone nearest the sealed pressure, which reduces the contact pressure in this region due to the seal lip lifting off of the rod. Thus, the contact pressure decreases below the static contact pressure. The contact pressures have large enough values to indicate the presence of mixed lubrication in this region. Over the second half of the sealing zone, the fluid pressure is zero which indicates the presence of cavitation. Due to the presence of cavitation, there is no decrease in the contact pressure from the static contact pressure, which indicates mixed lubrication.

The pressure distributions for the instroke case are shown below in Figure 11.

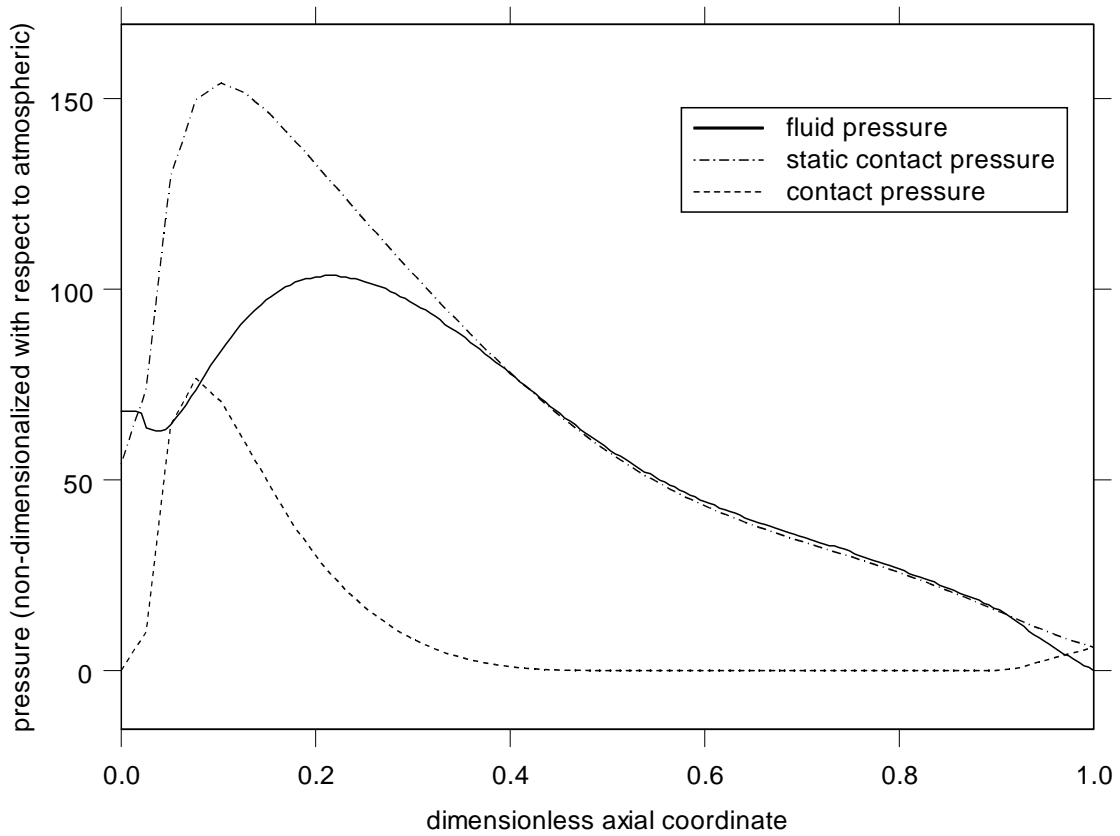


Figure 11: Pressure distributions, base case, instroke

Key observations similar to those in Figure 9 can be made for the pressure distributions in Figure 11. In Figure 11, the contact pressure is zero and no cavitation is present over the two-thirds of the sealing zone furthest from the sealed pressure. This indicates that the seal completely lifts off from the rod, as a result of significant hydrodynamic fluid pressure generation. Thus, full film lubrication with zero contact pressure exists over this region. Over the first one-third of the sealing zone nearest the sealed pressure, mixed lubrication is present as both the contact pressure and fluid pressure both have values.

The shear stress in the sealing zone is also calculated via auxiliary calculations in the numerical model. Figure 12 shows the obtained distribution of the frictional shear stress.

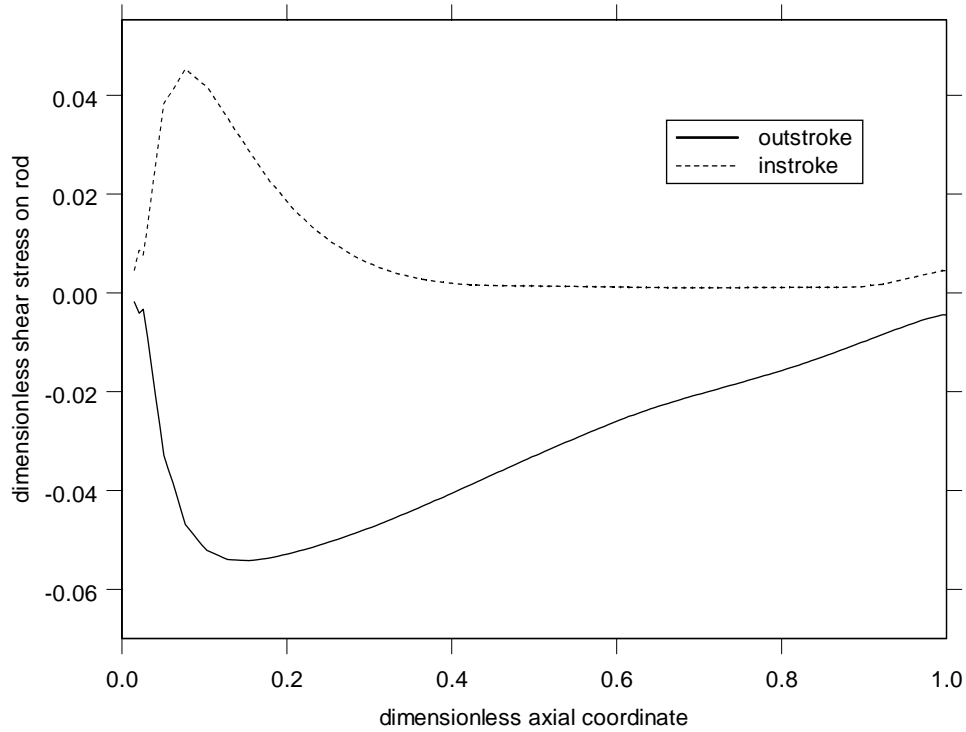


Figure 12: Frictional shear stress distributions, base case

Figure 12 shows that the shear stress has a larger magnitude for the outstroke than for the instroke. This fact can be attributed to the differences in the film thickness distributions. The shear stress values also have differing signs, which should be expected, and the peaks of the distribution exist near the high pressure side where the maximum contact pressures are located.

The computer program performs additional auxiliary calculations to obtain the dimensionless flow rates. The values for the dimensionless flow rates for the base case for instroke and outstroke are shown in Table 6.

Table 6: Dimensionless flow rates for base case, 6.9 MPa sealed

	Magnitude of Dimensionless flow rate, $\hat{q}$
Base case instroke	$2.302 \times 10^4$
Base case outstroke	$1.713 \times 10^4$

While the results for the flow rate are significant, the key attribute from the seal that is the most important is the net leakage. The net leakage is the difference between the amount of fluid carried out by the rod during the outstroke and the amount of fluid carried back in by the instroke. In order to have no net leakage from the seal, it is necessary that the latter must equal or exceed the former. The leakage of the seal for each stroke is determined by multiplying the flow rate by the stroke time. Since the latter is inversely proportional to the rod speed, the dimensionless parameter that describes the leakage is  $\hat{q}/\zeta$ . Based on this parameter, if the parameter for the instroke equals or exceeds the value of the parameter for the outstroke then the seal is predicted to not leak. However, if the value of the parameter for the instroke does not equal or exceed the parameter for the outstroke then the seal is predicted to leak. For the base case,

$(\hat{q}/\zeta)_{outstroke} = 17.61$  and  $(\hat{q}/\zeta)_{instroke} = 18.49$ . Therefore, this seal is predicted to not leak by the numerical model for the given base parameters.

Figure 13 shows a plot of  $\hat{q}/\zeta$  versus dimensionless seal roughness,  $\hat{\sigma}$ , where the base case parameters are all used except for the roughness, which is varied. In Figure 13, the arrows in the figure indicate the base case roughness and operating point.

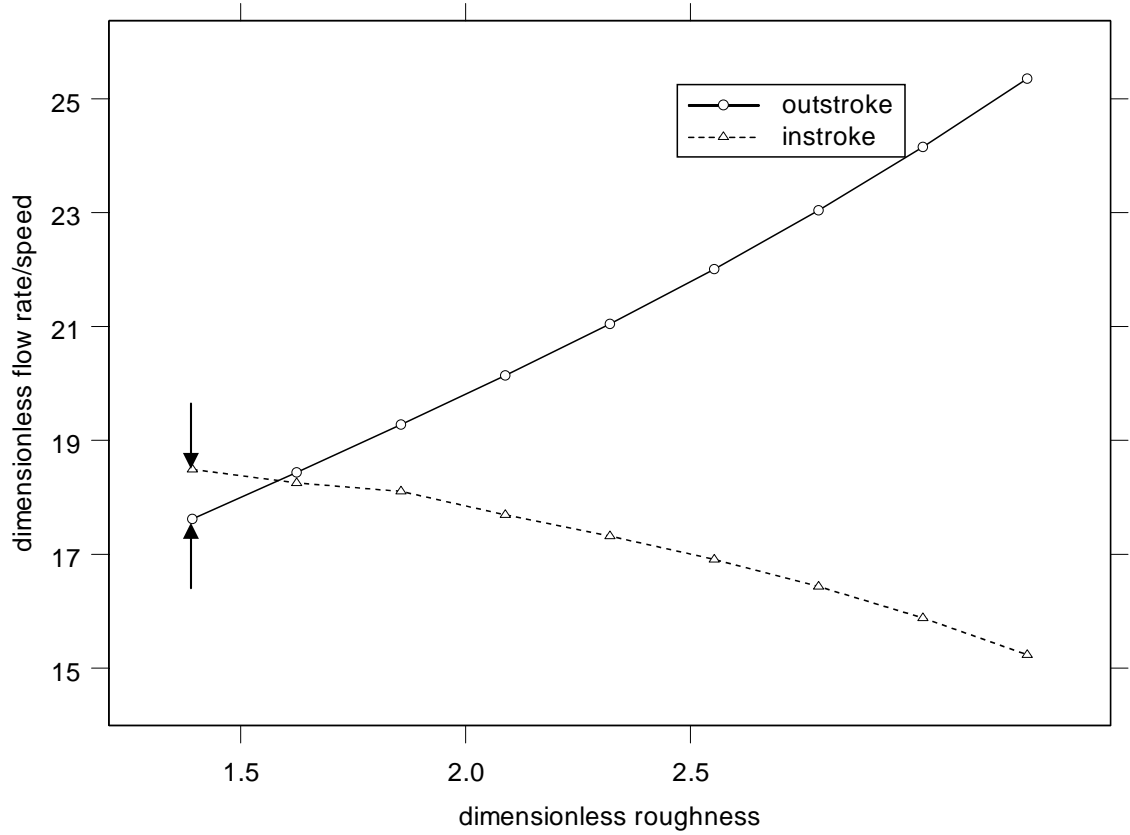


Figure 13: Flow rate/speed vs. roughness, base case speeds

The concept used here is that if the  $\hat{q}/\zeta$  for the instroke case has a greater magnitude than the  $\hat{q}/\zeta$  for the outstroke case then the seal will have no leakage. Thus,

for dimensionless roughness values greater than approximately 1.58 (corresponding to a roughness of  $0.34\text{ }\mu\text{m}$ ), the seal will have some leakage, whereas for values lower, the seal will have no leakage. Based on the results shown in Figure 13, it becomes obvious that the roughness of the seal has a drastic effect onto whether or not a given seal will or will not seal appropriately. Based on a full-film lubrication model, Müller and Nau (1998) states that a seal will not leak as long as the magnitude of the slope of the static contact pressure curve near the high pressure end of the seal is larger than that near the low pressure side, and the instroke speed is equal to or larger than the outstroke speed. This is the case for the analyzed seal. However, Figure 13 reveals that for roughness values above 1.58 the seal will leak. This observation shows that the effectiveness of the seal is highly dependent on the seal roughness magnitude, and models based on full-film lubrication are inadequate.

Figure 14 shows plots of  $\hat{q}/\zeta$  versus the dimensionless rod speed for two roughness values of  $\hat{\sigma} = 1.392$  and  $2.320$  ( $\sigma = 0.3\text{ }\mu\text{m}$  and  $0.5\text{ }\mu\text{m}$ ). Figure 14 assists in the determination of whether or not a seal will leak, as for a specified roughness it can be seen whether or not  $\hat{q}/\zeta$  for the instroke exceeds the  $\hat{q}/\zeta$  value for the outstroke. Any combination of roughness and instroke and outstroke speeds can be investigated to obtain a case where the seal does not leak. In Figure 14, the arrows indicate the dimensionless flow rate over speed results for each of the roughness values at the operating speeds.



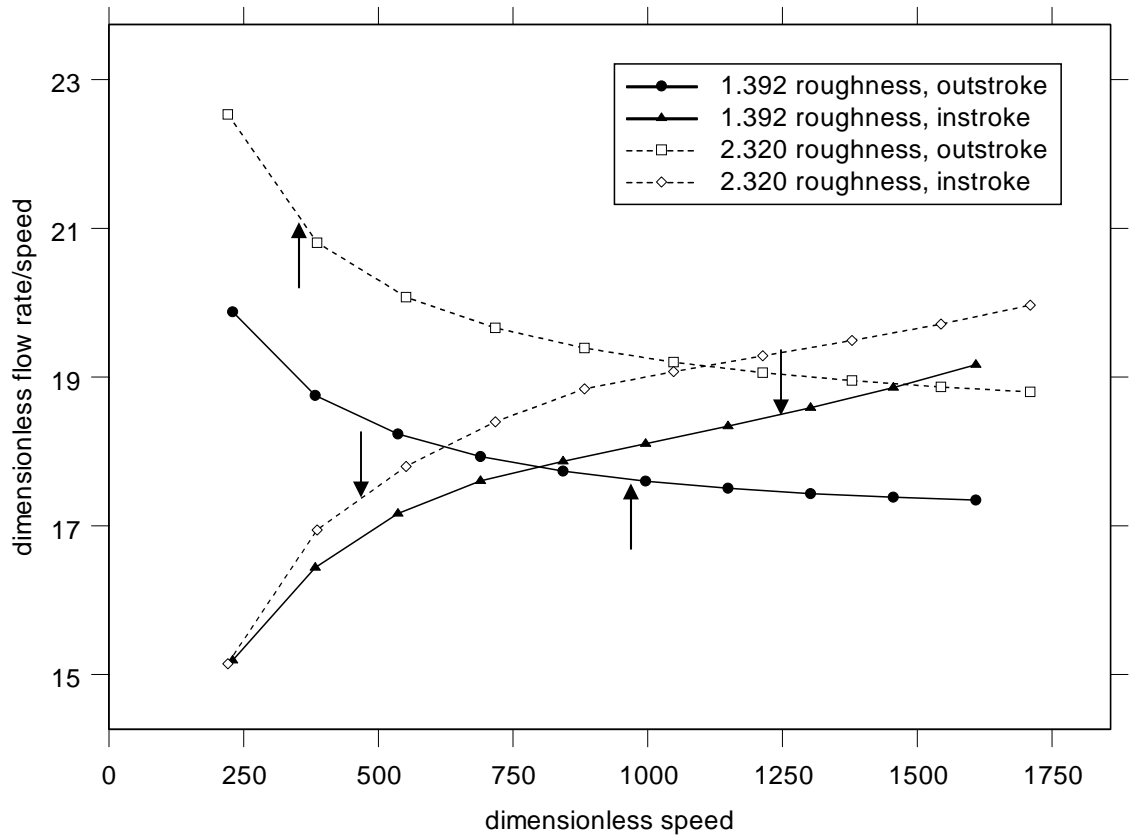


Figure 14: Flow rate/speed vs. speed for 1.392 & 2.320 roughnesses (0.3  $\mu\text{m}$  & 0.5  $\mu\text{m}$ )

It can be seen that for roughness of 1.392 (0.3  $\mu\text{m}$ ), Figure 14 indicates that the seal will not leak for the given operating conditions as the dimensionless flow rate over speed for the instroke exceeds that of the outstroke for the operation speeds. For roughness of 2.320 (0.5  $\mu\text{m}$ ), Figure 14 indicates that at the given operating conditions leakage will occur from the seal as the dimensionless flow rate of the outstroke exceeds that of the instroke for the operation speeds. These results are consistent with the predictions made by Figure 13 where the maximum roughness for no leakage with the base parameters is 1.58 (0.34  $\mu\text{m}$ ). Variations in the rod speeds for the instroke and

outstroke have an effect on whether or not the seal will leak. For the case with a roughness of 1.392 (0.3  $\mu\text{m}$ ), the base case speeds yield results showing that the speed will not leak; however, for lower speeds the seal will actually leak. Additionally, the case with a roughness of 2.320 (0.5  $\mu\text{m}$ ) leaks using the base case operating speeds, but for significantly higher speeds the seal will not leak. Thus, the operating speeds of the rod for the instroke and outstroke play a significant role in determining whether or not a seal will leak.

It is shown that the current base case model for a roughness of 0.3  $\mu\text{m}$  does not leak, however the base case model with a roughness of 0.5  $\mu\text{m}$  does leak. Table 7 summarizes the findings from Figure 13.

Table 7: Leakage rates for base cases, 6.9 MPa sealed

	$(\hat{q}/\zeta)_{outstroke}$	$(\hat{q}/\zeta)_{instroke}$
Roughness of 0.3 $\mu\text{m}$	17.61	18.49
Roughness of 0.5 $\mu\text{m}$	21.04	17.35

It can be seen that at the base speeds a larger roughness of 0.5  $\mu\text{m}$  increases  $(\hat{q}/\zeta)_{outstroke}$  by 3.43 and decreases  $(\hat{q}/\zeta)_{instroke}$  by 1.14. The significance of this observation is that the increase in roughness causes net leakage by its influence on both the outstroke and instroke.

Figure 15 – Figure 17 show the pressure distributions for the instroke and outstroke and the film thickness distributions for the seal with a roughness of 0.5  $\mu\text{m}$ .

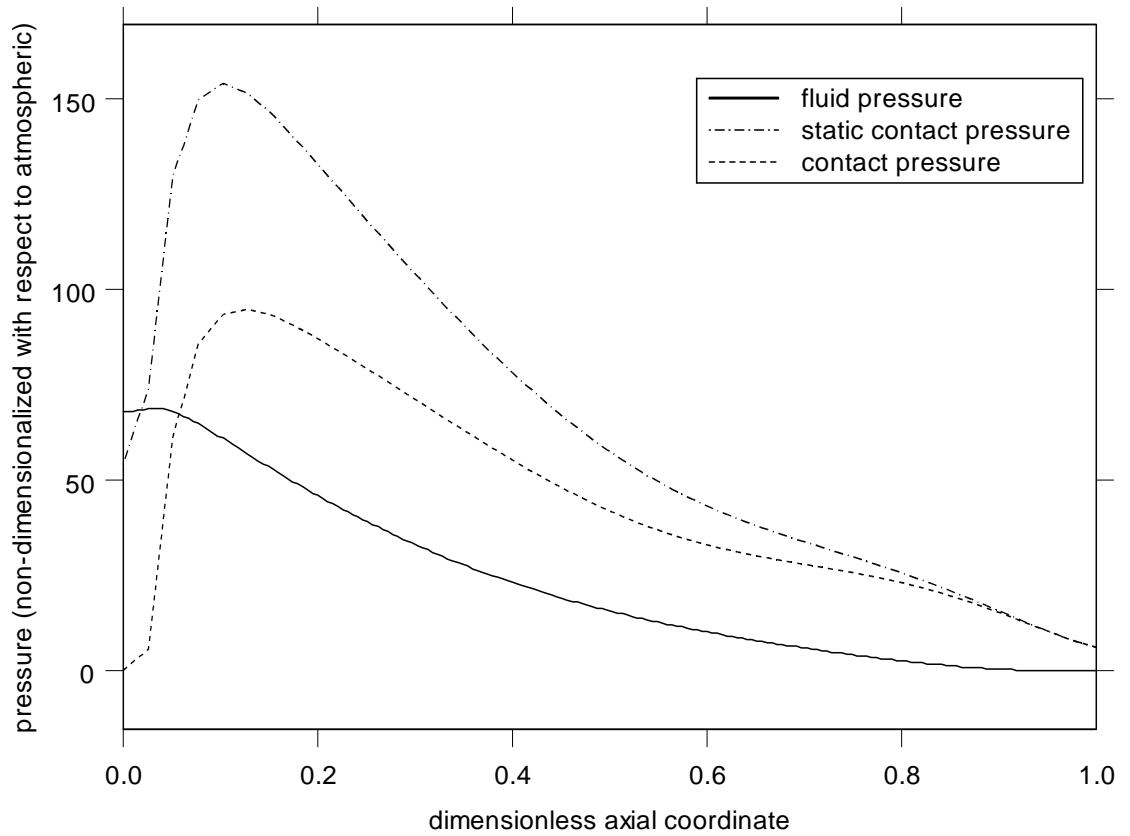


Figure 15: Pressure distributions, 2.320 roughness ( $0.5 \mu\text{m}$ ), base speeds, outstroke

Similar observations are made as were made with Figure 10 and Figure 11. Figure 15 shows the outstroke results for the  $0.5 \mu\text{m}$  case which differs from Figure 10 for outstroke results for the  $0.3 \mu\text{m}$  case in that the previously noticeable cavitation is no longer present. The lack of cavitation can be seen as in Figure 15 as the fluid pressure no longer goes to zero through the sealing zone but remains at a positive value. These results also indicate the presence of mixed lubrication as some contact pressure exists throughout the entire sealing zone. The significance of this observation is that the cavitation that was previously present for the smoother case is no longer present during the outstroke of the

rod, and as a result the amount of fluid transported out by the rod during this phase is significantly larger. Thus, a decrease in seal roughness leads to the occurrence of cavitation during the outstroke of the rod which is beneficial in limiting the amount of fluid transported outward.

Additionally, the pressure distributions for the instroke results for the  $0.5\ \mu\text{m}$  case are shown below in Figure 16.

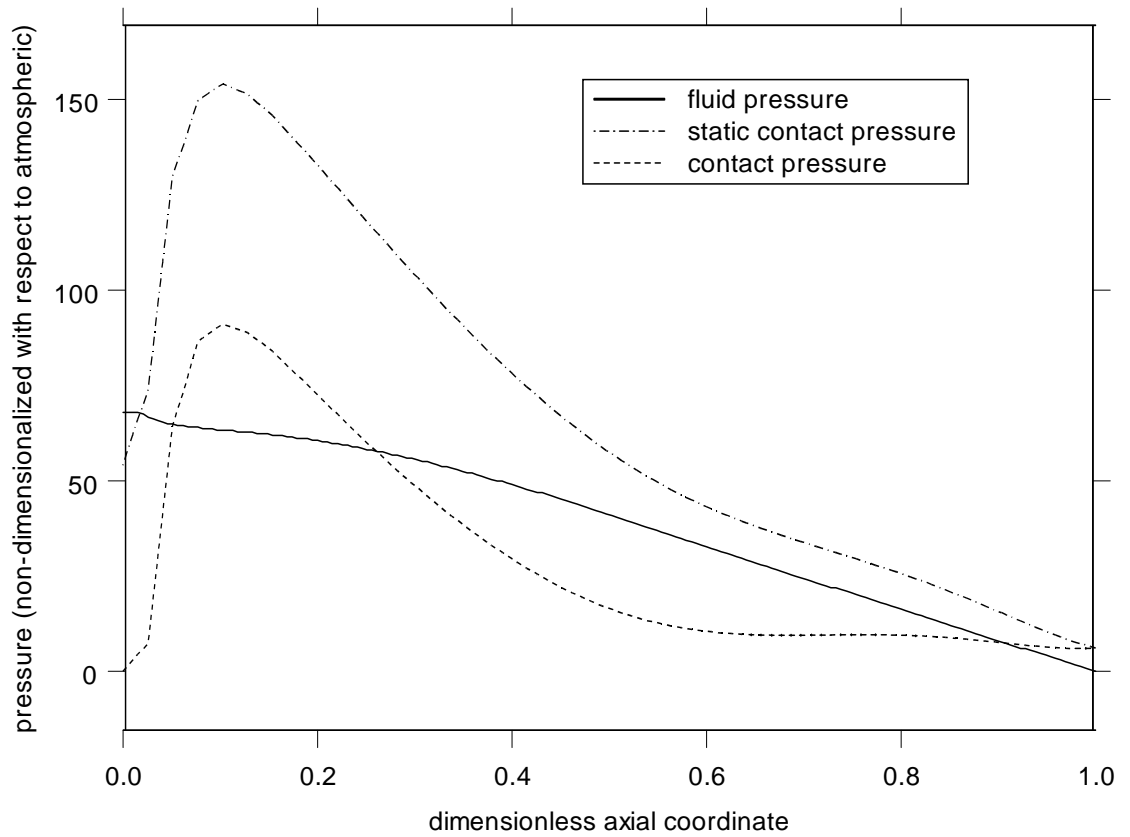


Figure 16: Pressure distributions, 2.320 roughness ( $0.5\ \mu\text{m}$ ), base speeds, instroke

By comparing the results shown in Figure 16 for the  $0.5\ \mu\text{m}$  case with Figure 11 for the  $0.3\ \mu\text{m}$  case, it can be noted that mixed lubrication now exists over the entire sealing zone

rather than the full-film lubrication for the 0.3  $\mu\text{m}$  case. Additionally, the magnitude for the fluid pressure is significantly lower for the 0.5  $\mu\text{m}$  case. The increase in the seal roughness leads to an elimination of the full film lubrication present in the smoother case. The fluid transported during the instroke is therefore less for the rougher case. As shown by Figure 15, Figure 10, Figure 16 and Figure 11, a smoother seal with lower surface roughness has better results concerning net leakage, as the smoother seal tends to have cavitation during the outstroke, limiting the amount of fluid transport during the outstroke, and full film lubrication during the instroke of the rod, increasing the amount of fluid transport during the instroke of the rod. These results show that the smoother the seal, the more effective it will be.

The film thickness distribution for both the instroke and outstroke of the 0.5  $\mu\text{m}$  case is shown below in Figure 17.

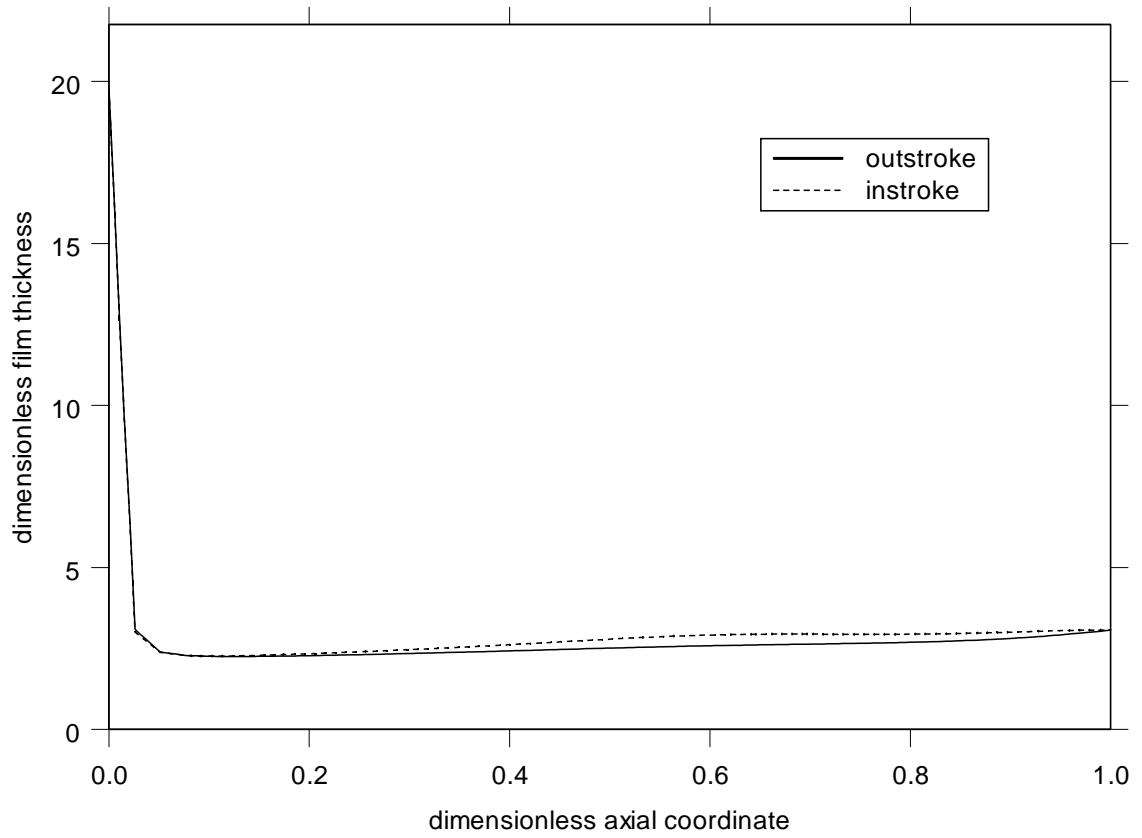


Figure 17: Film thickness distributions, 2.320 roughness ( $0.5\ \mu\text{m}$ ), base speeds

Comparing Figure 17 with Figure 9, confirms the observation, above, that the increased roughness of the 2.320 roughness case, leads to elimination of the full-film lubrication present in the smoother case.

#### 4.2 Dimensionless Results for 13.8 MPa Sealed Pressure

The results for the same base case parameters now using a sealed pressure of 13.8 MPa (2000 psi) have also been calculated for a typical hydraulic rod seal and similar figures have been generated. These figures have similar trends to the ones created for the sealed pressure of 6.9 MPa, and the similarities and difference will be discussed.

The film thickness distribution for the sealing zone is shown in Figure 18 using the base case parameters with the higher sealed pressure.

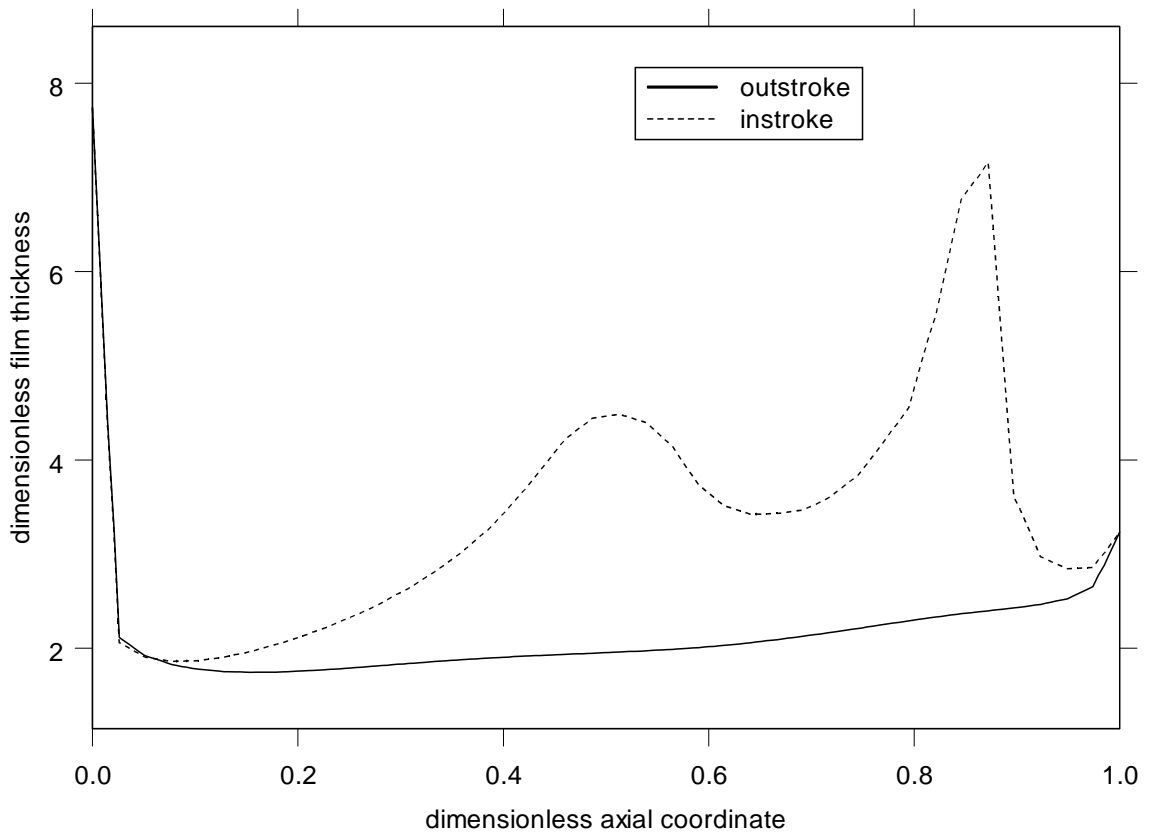


Figure 18: Film thickness distributions, base case

In Figure 18, it can be seen that once again the dimensionless film thickness for the outstroke of the rod has a value less than 3 throughout the entire sealing zone. The

film thickness has a larger value at the initial section of the sealing zone nearest the high pressure side of the seal, which indicates the presence of mixed lubrication in this region. For the instroke of the rod, the film thickness is less than three indicating mixed lubrication for approximately one-third of the sealing zone in the area located nearest the high pressure side. This result is similar to the result obtained for the sealed pressure of 6.9 MPa results. Additionally, in the remainder of the sealing zone the film thickness has a value larger than 3 which indicates the presence of full film lubrication, which also agrees with the results for the 6.9 MPa. The film thickness in this region is much larger for the 13.8 MPa case than was the case for the 6.9 MPa case. Thus, increasing the sealed pressure leads to similar trends within the film thickness distributions with the magnitude of the film thickness for the full film lubrication during the instroke to be much greater than for the lower sealed pressure case. This is a favorable characteristic.

The fluid pressure, static contact pressure, and contact pressure distributions within the sealing zone for a sealed pressure of 13.8 MPa are shown for the outstroke of the rod in Figure 19.



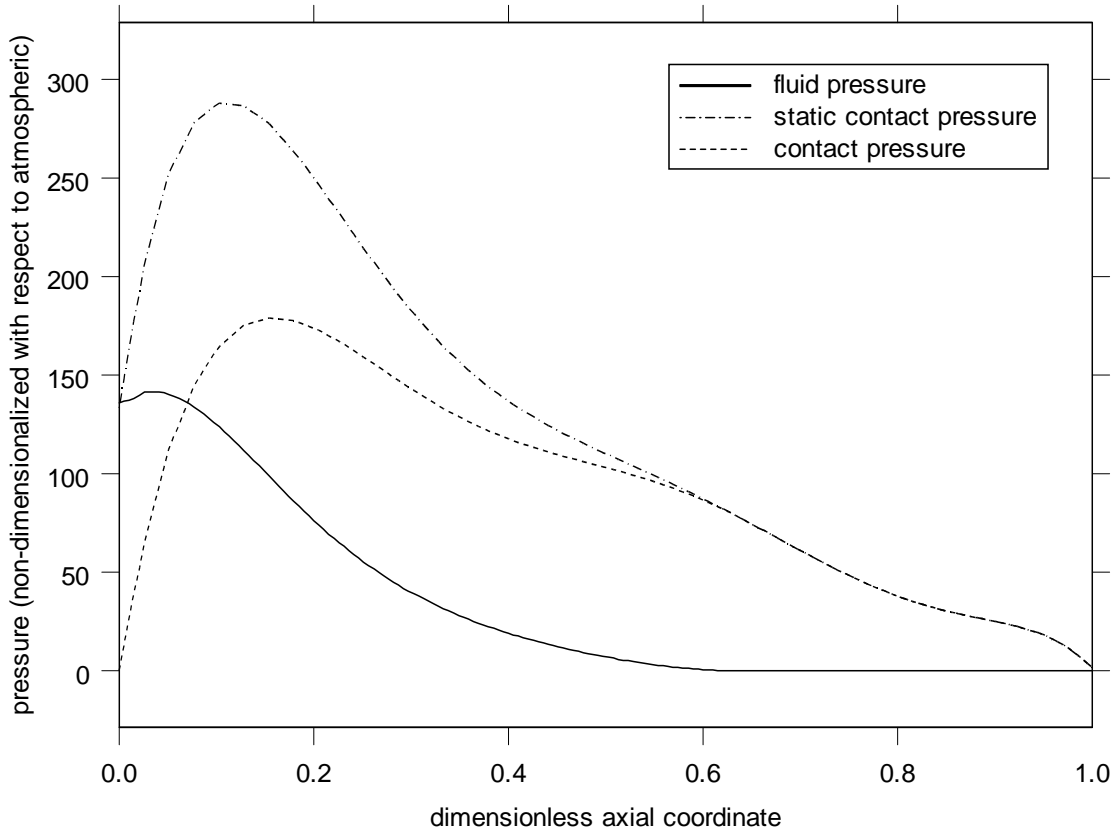


Figure 19: Pressure distributions, base case, outstroke

Once again, these results shown in Figure 19 agree well with the film thickness results. The seal lip partially lifts off the rod reducing the contact pressure and causing the presence of hydrodynamic fluid pressure over the first half of the sealing zone nearest the sealed pressure. The contact pressures are less than the static contact pressure over this region, but they are large enough to indicate mixed lubrication. Over the second half of the sealing zone, the fluid pressure goes to zero indicating cavitation. The presence of cavitation implies that the contact pressure is equal to the static contact pressure which characterizes mixed lubrication. The primary difference between the high pressure

results and the low pressure results is that the magnitudes of the pressures are higher for the sealed pressure of 13.8 MPa case. Both cases have a region of cavitation during the outstroke of the rod, but the region is over a slightly larger portion of the sealing zone for the lower pressure case. For the higher pressure case, this is unfavorable.

Similar to Figure 19, the pressure distributions for the instroke of the rod are obtained and shown in Figure 20.

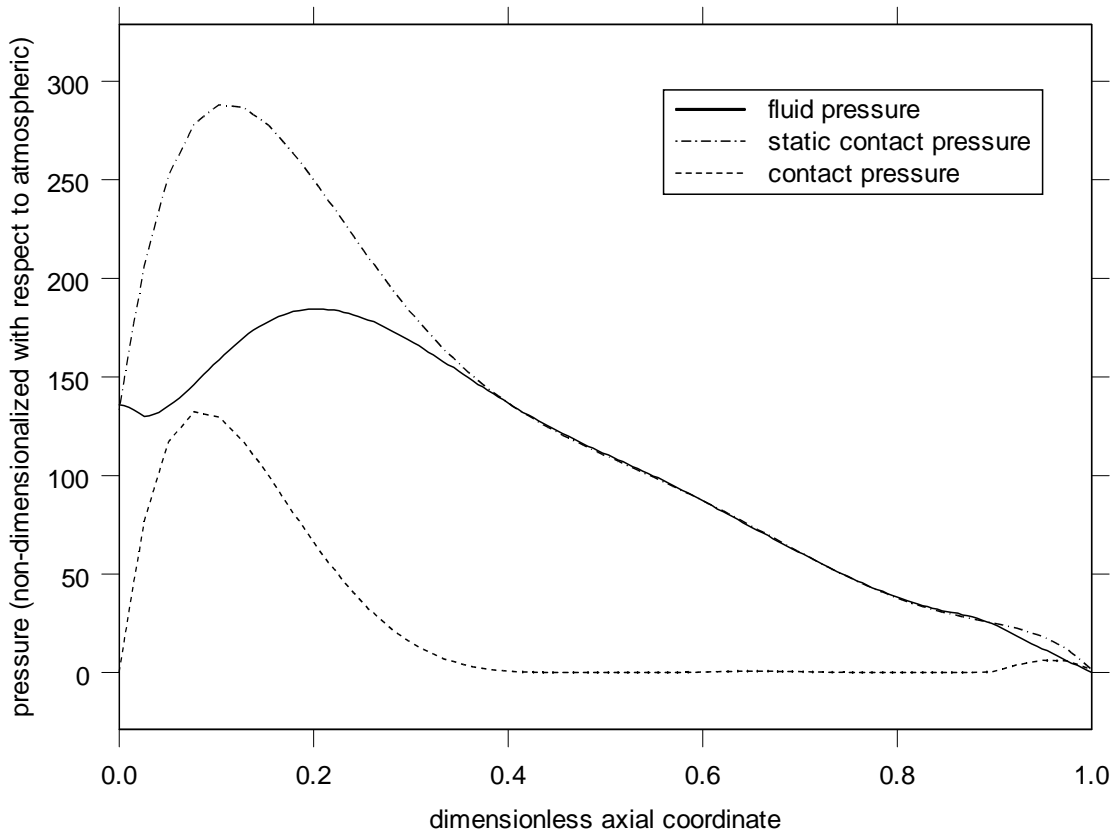


Figure 20: Pressure distributions, base case, instroke

In Figure 20, mixed lubrication is present over the first one-third of the sealing zone nearest the sealed pressure as there is both fluid pressure and contact pressure values.

It also can be seen that the contact pressure is zero and no cavitation is present in the fluid pressure over the two-thirds of the sealing zone furthest from the sealed pressure. This observation shows that the seal must lift off completely from the rod resulting in significant amount of hydrodynamic fluid pressure. As a result, it can be stated that full film lubrication is present in this region with no contact amongst the asperities, consistent with Figure 18.

Figure 21 shows the distribution of the frictional shear stress in the sealing zone that is obtained via auxiliary calculations from the numerical model.

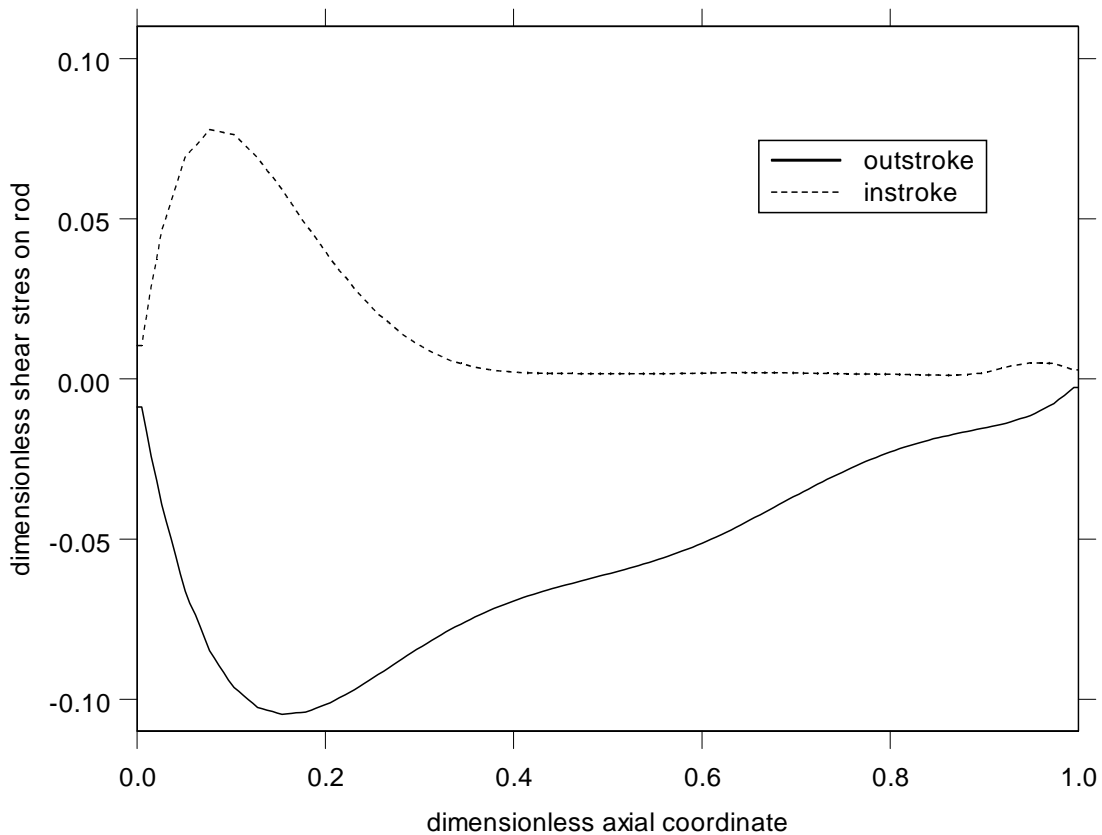


Figure 21: Frictional shear stress distributions, base case

Figure 21 has similar patterns to Figure 12 which shows the shear stress distributions for the 6.9 MPa case. The shear stress has a larger magnitude for the outstroke than for the instroke, because of the film thickness profile. Also, the shear stress values still have opposing signs, and the peaks of the distributions occur near the high pressure side approximately where the lip is located and the contact pressure is a maximum. The shear stress distributions for the higher pressure case follow the same general trends as the lower pressure case, where the magnitudes for the former are larger than for the latter.

Additional calculations are performed by the computer program to obtain the dimensionless flow rate. The results for the dimensionless flow rates for the base case parameters at 13.8 MPa for the instroke and outstroke are shown in Table 8.

Table 8: Dimensionless flow rates for base case, 13.8 MPa sealed

	Magnitude of Dimensionless flow rate, $\hat{q}$
Base case instroke	$2.121 \times 10^4$
Base case outstroke	$1.622 \times 10^4$

Increasing the sealed pressure to 13.8 MPa caused both the instroke and outstroke flow rates to decrease in magnitude. However, the leakage of the seal is once again the key parameter which is determined by investigating the dimensionless parameter of  $\hat{q}/\zeta$ . For the base case and the higher sealed pressure,  $(\hat{q}/\zeta)_{outstroke} = 16.67$  and  $(\hat{q}/\zeta)_{instroke} = 17.03$ . As the value for the instroke exceeds the value for the outstroke, the seal is predicted to not leak by the numerical model for the given base parameters. The results for  $\hat{q}/\zeta$  for both the instroke and the outstroke and the lower pressure have

slightly higher values than for the higher pressure. However, for the lower pressure, the difference between the instroke fluid transport and the outstroke fluid transport had a magnitude of 0.88, while that difference for the higher pressure case had a magnitude of 0.36. As the sealed pressure is increased, the effectiveness of the seal is therefore decreased. This observation implies that for constant operating parameters a smaller sealed pressure will yield better results for net leakage, which should be expected.

Figure 22 shows a plot of  $\hat{q}/\zeta$  versus dimensionless rms roughness,  $\hat{\sigma}$ , where the base case parameters are all used except for the roughness that is varied. The arrows indicate the base case with a roughness of  $0.3 \mu\text{m}$ .

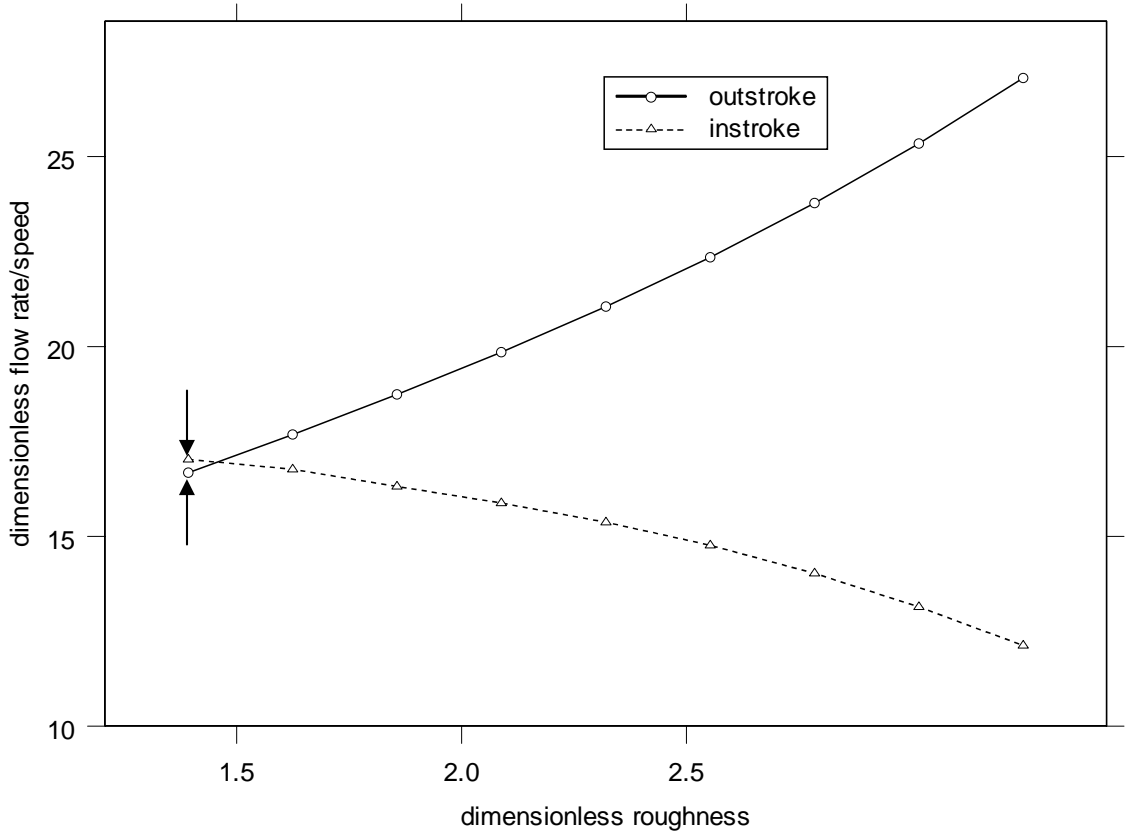


Figure 22: Flow rate/speed vs. roughness, base case speeds, 13.8 MPa

The idea for this plot is once again that if the  $\hat{q}/\zeta$  for the instroke is greater in magnitude than the  $\hat{q}/\zeta$  for the outstroke case, then the seal will not leak. Thus, for dimensionless roughness values greater than approximately 1.46 (corresponding to a roughness of  $0.32\text{ }\mu\text{m}$ ), leakage will be present from the seal, whereas from lower values of roughness there will be no leakage. For the lower sealed pressure of  $6.9\text{ MPa}$ , the seal did not leak for roughness values below  $1.58$  ( $0.34\text{ }\mu\text{m}$ ). Based on these results, an increase in the sealed pressure will decrease the maximum roughness for which the seal will not leak.

Figure 23 shows plots of  $\hat{q}/\zeta$  versus the dimensionless rod speed for two roughness values of  $\hat{\sigma} = 1.392$  and  $2.320$  ( $\sigma = 0.3\text{ }\mu\text{m}$  and  $0.5\text{ }\mu\text{m}$ ).

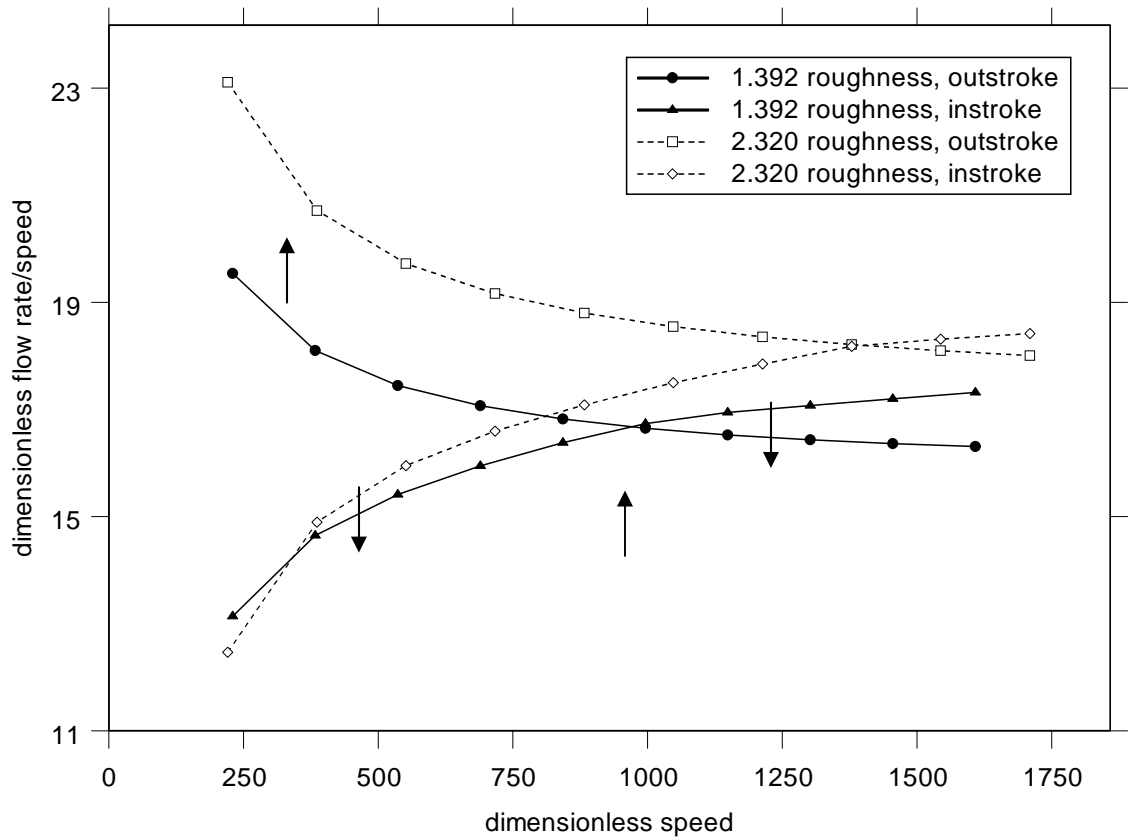


Figure 23: Flow rate/speed vs. speed for 1.392 & 2.320 roughness ( $0.3\text{ }\mu\text{m}$  &  $0.5\text{ }\mu\text{m}$ )

Once again, the rod speed plays an important role in whether or not the seal will leak, as decreasing the rod speeds for the smoother case will cause the seal to leak and increasing the rod speeds for the rougher case can cause the seal to not leak. The seal at the higher sealed pressure has similar performance as the lower sealed pressure and reacts to variance in rod speeds in a similar manner, as can be seen by comparing Figure 23 with Figure 14.

The numerical model has shown that the current base case parameters of a seal with a roughness of 0.3  $\mu\text{m}$  does not leak, however the base case model with a roughness of 0.5  $\mu\text{m}$  does leak.

Table 9 summarizes the leakage rates obtained from Figure 23.

Table 9: Leakage rates for base cases, 13.8 MPa sealed

	$(\hat{q}/\zeta)_{outstroke}$	$(\hat{q}/\zeta)_{instroke}$
Roughness of 0.3 $\mu\text{m}$	16.67	17.03
Roughness of 0.5 $\mu\text{m}$	21.04	15.37

Figure 24 – Figure 26 show the pressure distributions for the instroke and outstroke and the film thickness distributions for the seal with a roughness of 0.5  $\mu\text{m}$ .

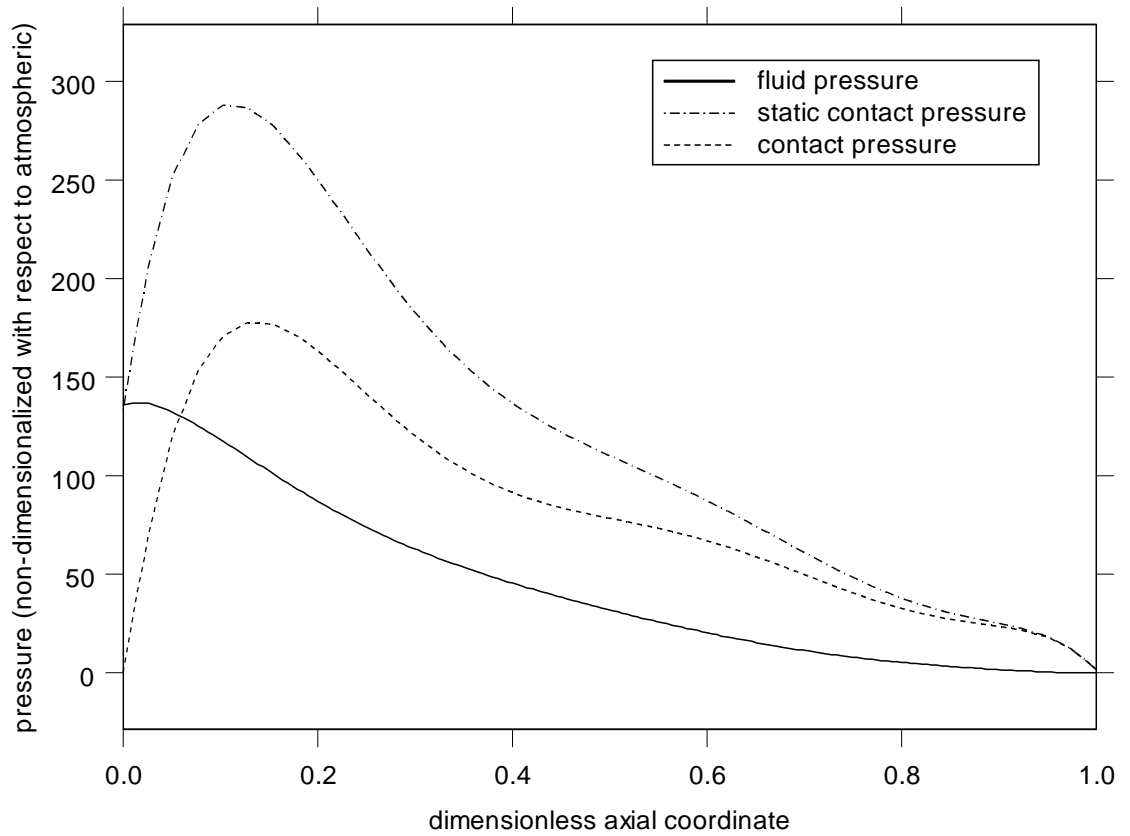


Figure 24: Pressure distributions, 2.320 roughness (0.5  $\mu\text{m}$ ), base speeds, outstroke

Figure 24 shows the outstroke results for the 0.5  $\mu\text{m}$  case which differs from Figure 19 for outstroke results for the 0.3  $\mu\text{m}$  case in that cavitation is no longer present. The lack of cavitation can be seen as in Figure 24, the fluid pressure no longer goes to zero through the sealing zone and the presence of mixed lubrication is noted. The elimination of the presence of cavitation during the outstroke of the rod was also noted for the lower sealed pressure. The trends for the pressure distributions with a larger seal roughness and higher sealed pressure agree with those found for the lower sealed pressure; however the magnitudes for the higher sealed pressure are larger.



The instroke results for the  $0.5\ \mu\text{m}$  case are shown below in Figure 25.

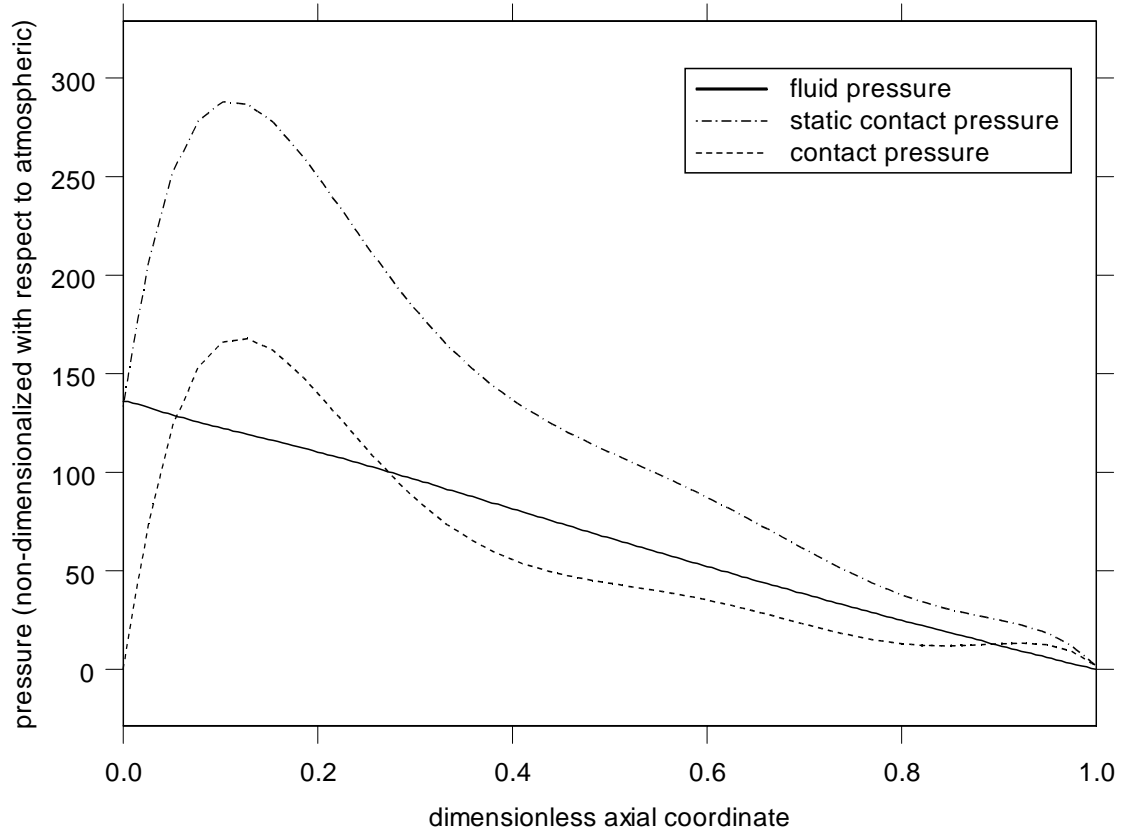


Figure 25: Pressure distributions, 2.320 roughness ( $0.5\ \mu\text{m}$ ), base speeds, instroke

By comparing the results shown in Figure 25 for the  $0.5\ \mu\text{m}$  case with Figure 20 for the  $0.3\ \mu\text{m}$  case, it can be noted that contact pressure now exists over the entire sealing zone rather than the one-third for the  $0.3\ \mu\text{m}$  case indicating mixed lubrication, eliminating the presence of full film lubrication. Additionally, the magnitude for the fluid pressure is significantly lower for the  $0.5\ \mu\text{m}$  case. This elimination of the presence of full film lubrication during the instroke of the rod is consistent with the results of the

lower sealed pressure case. The magnitudes for the pressure distributions at a higher sealed pressure are larger than those for a lower sealed pressure.

The film thickness distribution for the  $0.5\ \mu\text{m}$  case is shown below in Figure 26.

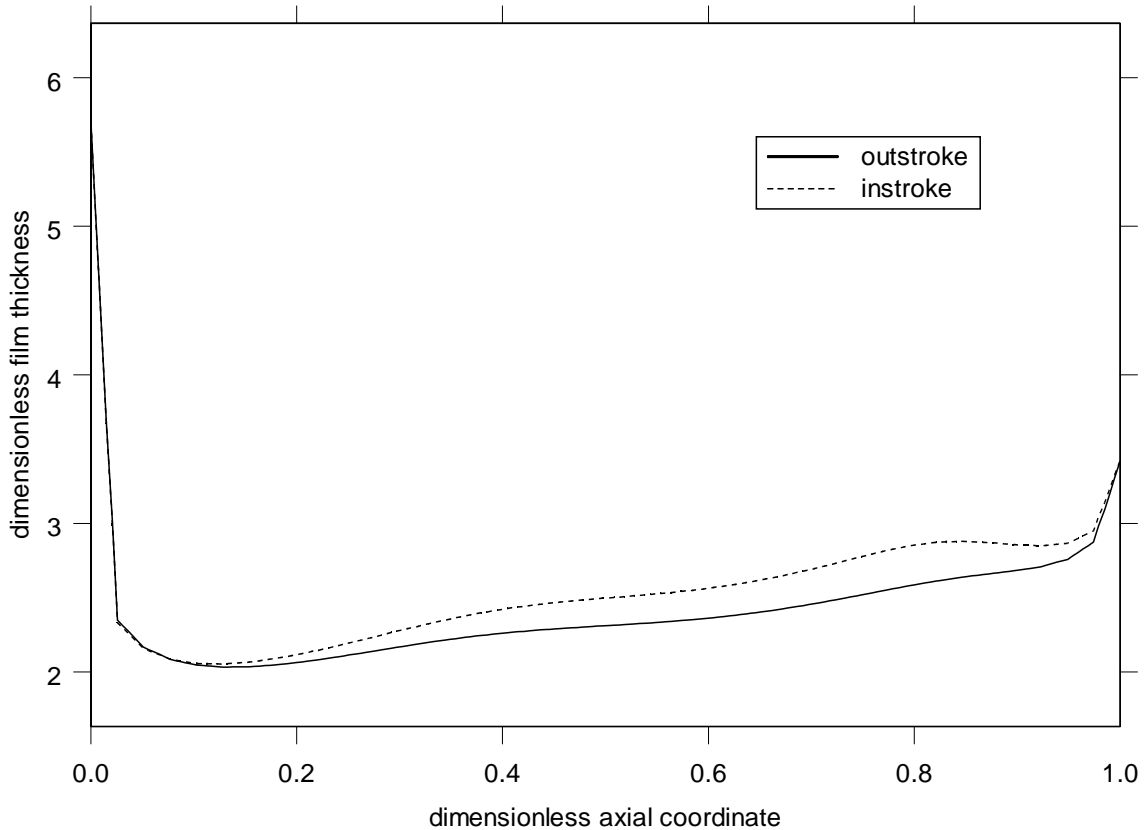


Figure 26: Film thickness distributions, 2.320 roughness ( $0.5\ \mu\text{m}$ ), base speeds

It can be noted in Figure 26 for the  $0.5\ \mu\text{m}$  case that the film thickness for the instroke appears to have a lower value throughout the sealing zone below the key parameter of a dimensionless film thickness of 3, which indicates mixed lubrication as the pressure distributions also did.

### 4.3 Dimensional Results for 6.9 MPa Sealed Pressure

Dimensional results were also obtained for the case with a sealed pressure of 6.9 MPa. The base case parameters found in Table 5 were used to simulate the results for the seal. Conversions are made to obtain the dimensional results from the dimensionless results. Each quantity was non-dimensionalized during the numerical model, and a reversal of that process will yield the dimensional results. The dimensional leakage can be related to the dimensionless leakage via

$$leakage = \frac{\hat{q}}{\zeta} \cdot \left( \frac{\sigma \cdot \pi \cdot D \cdot L}{12} \right) \quad (39)$$

The results are similar to the plots for the dimensionless results for the 6.9 MPa case, and the film thickness and pressure distributions for both the 0.3  $\mu\text{m}$  and 0.5  $\mu\text{m}$  cases are shown in Figure 34 – Figure 40 of Appendix B.

To quantify the leakage of the seal, the dimensional leakage per stroke (fluid transport) was obtained as a function of the roughness of the seal, and the results are shown in Figure 27. The base case roughness results for the outstroke and the instroke are indicated by the arrows on the figure.

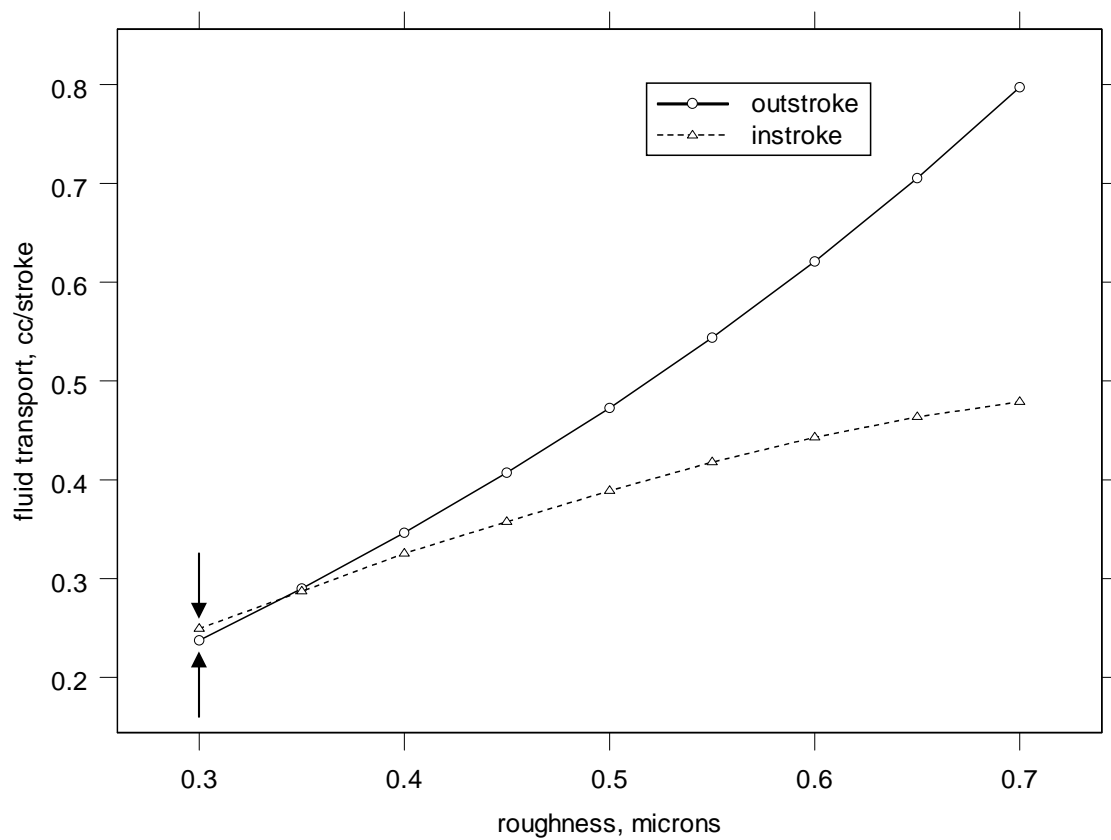


Figure 27: Fluid transport vs. roughness

Figure 28 and Figure 29 show the effect of rod speed of the leakage per stroke of the seal for different roughness values; the arrows indicate the base operating speeds of the rod.

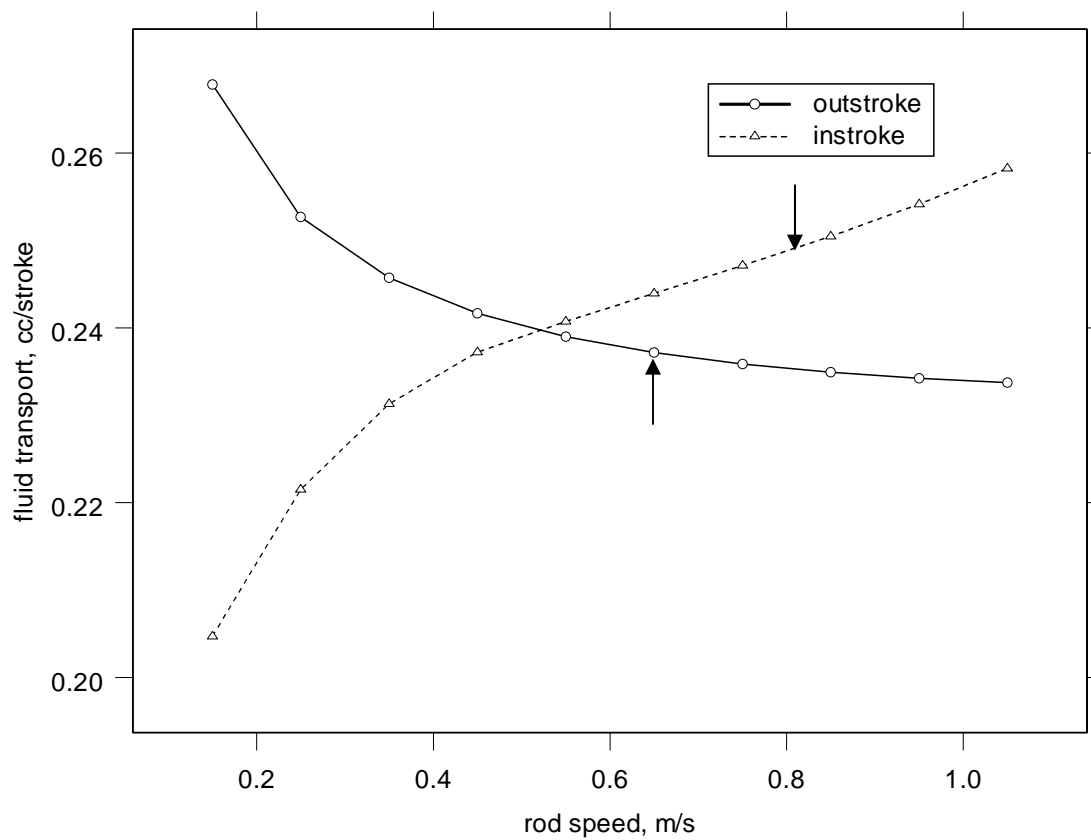


Figure 28: Fluid transport vs. rod speed for 0.3  $\mu\text{m}$  roughness

Figure 29 shows the results for the fluid transport for a seal with a roughness value of 0.5  $\mu\text{m}$ . The arrows again indicate the fluid transport at the base operating speeds for the instroke and outstroke of the rod.

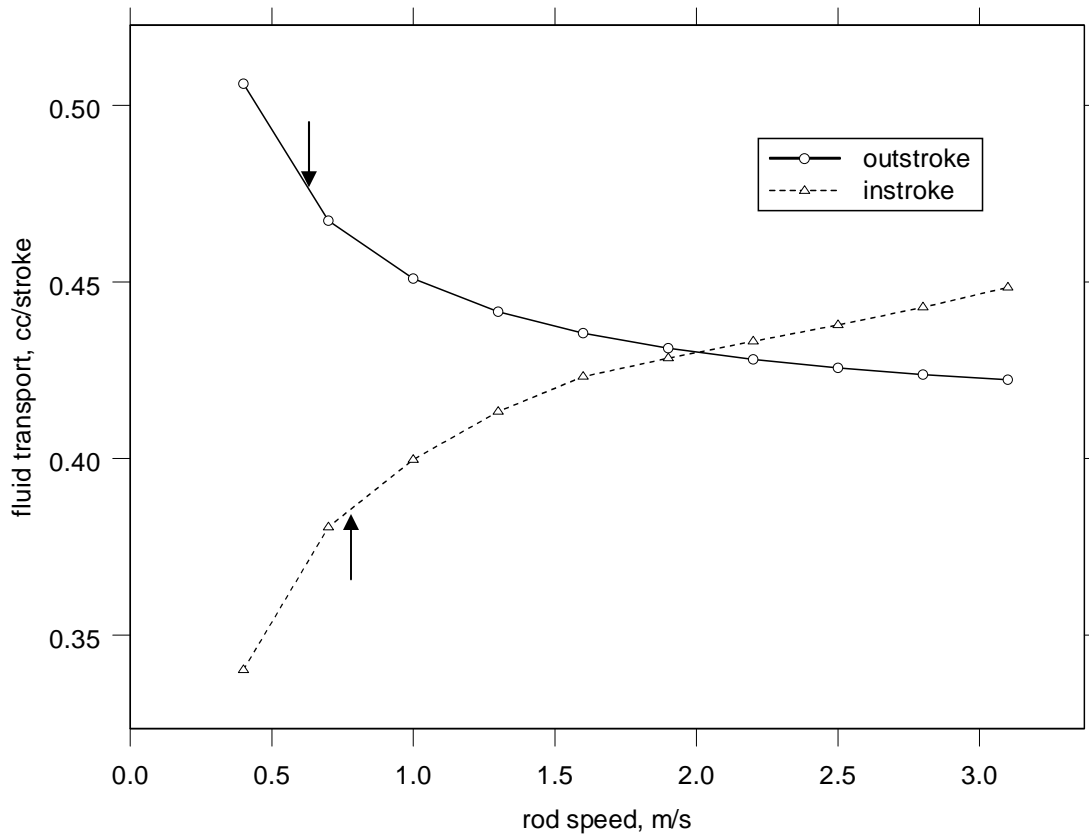


Figure 29: Fluid transport vs. rod speed for 0.5  $\mu\text{m}$  roughness

The results showing the magnitudes for the fluid transport for the different roughness values from Figure 28 and Figure 29 are summarized below in Table 10.

Table 10: Fluid transport results for different roughness values

	0.5 $\mu\text{m}$ roughness seal - leaking	0.3 $\mu\text{m}$ roughness seal – non-leaking
Fluid transport – outstroke	0.473 cc/stroke	0.237 cc/stroke
Fluid transport – instroke	0.390 cc/stroke	0.249 cc/stroke

Table 10 shows insight into the leakage rates for a given seal. For the 0.5  $\mu\text{m}$  roughness seal, the fluid transport magnitudes are almost double what they are for the 0.3  $\mu\text{m}$  roughness case. This increase in the roughness values causes an increase in the fluid transport value, but the change in roughness causes the outstroke fluid transport to increase at a greater rate than the instroke fluid transport. For fluid transport in the 0.3  $\mu\text{m}$  case, the instroke is greater than the outstroke; however this is no longer the situation for the 0.5  $\mu\text{m}$  case.

#### **4.4 Dimensional Results for 13.8 MPa Sealed Pressure**

Dimensional results were also obtained for the case with a sealed pressure of 13.8 MPa. The base case parameters found in Table 5 were used to simulate the results for the seal. The results are similar to the plots for the dimensionless results for the 13.8 MPa case, and the film thickness and pressure distributions for both the 0.3  $\mu\text{m}$  and 0.5  $\mu\text{m}$  cases are shown in Figure 41 – Figure 47 of Appendix C.

The fluid transport is obtained as a function of the roughness and it is used to quantify the leakage of the seal. The results are shown in Figure 30, and the base case results of roughness are indicated by the arrows.

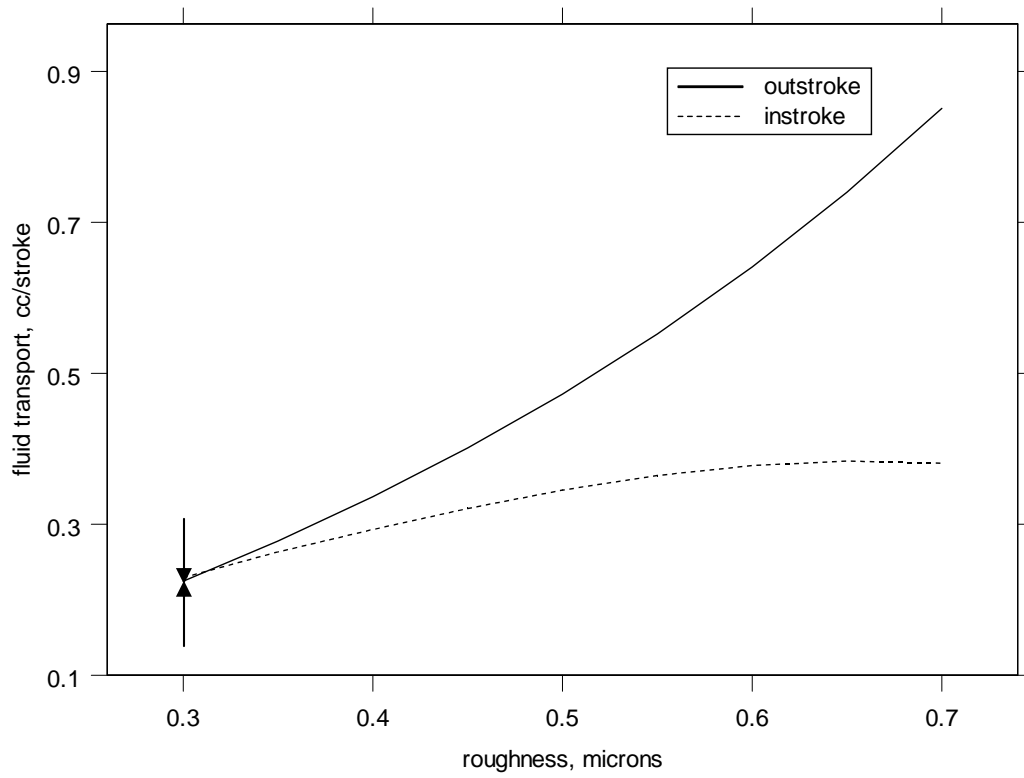


Figure 30: Fluid transport vs. roughness for 13.8 MPa

Figure 31 and Figure 32 show the fluid transport for different rod speeds for two different roughness values. The arrows indicate the base operating speeds of the rod.



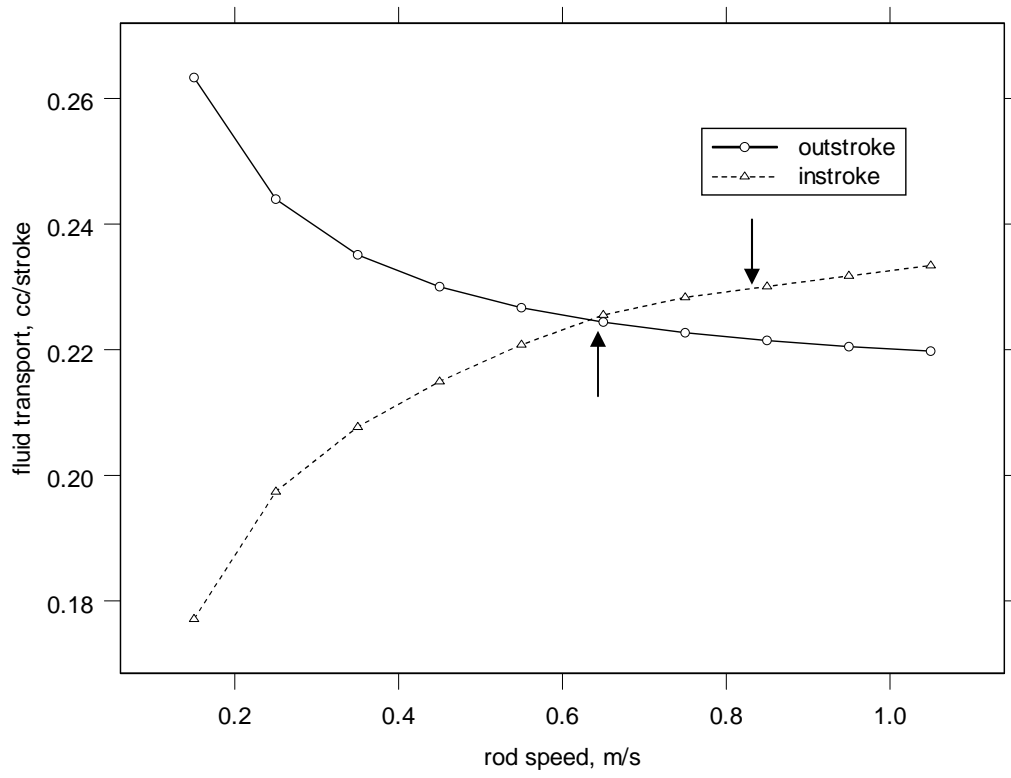


Figure 31: Fluid transport vs. rod speed for 0.3  $\mu\text{m}$  roughness

Figure 32 shows the fluid transport for the same conditions on the seal except that now the seal roughness is 0.5  $\mu\text{m}$ . Once again, the arrows indicate the results for the base operating speeds of the rod.

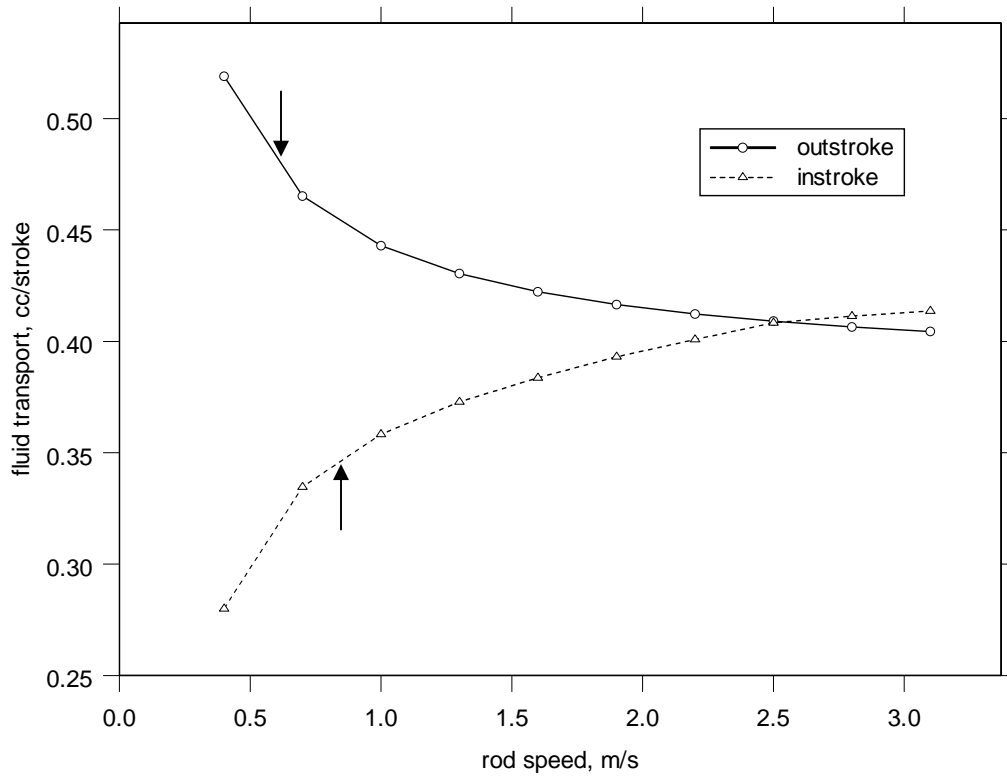


Figure 32: Fluid transport vs. rod speed for 0.5  $\mu\text{m}$  roughness

Table 11 summarizes the results obtained from Figure 31 and Figure 32.

Table 11: Fluid transport results for different roughness values

	0.5 $\mu\text{m}$ roughness seal – leaking	0.3 $\mu\text{m}$ roughness seal – non-leaking
Fluid Transport – outstroke	0.473 cc/stroke	0.222 cc/stroke
Fluid Transport – instroke	0.346 cc/stroke	0.229 cc/stroke

Table 11 shows the effect that seal roughness has on the amount of fluid transport for the instroke and outstroke of the rod. The fluid transport for the outstroke for a seal roughness of 0.5  $\mu\text{m}$  is more than twice the fluid transport for the 0.3  $\mu\text{m}$  roughness case. The fluid transport for the instroke for a seal roughness of 0.5  $\mu\text{m}$  is about 1.5 times the fluid transport for the 0.3  $\mu\text{m}$  roughness case. Based on this, it is noted that increasing the roughness parameter causes the outstroke value for fluid transport to grow faster than the instroke value for the fluid transport when all other parameters are held constant. From Table 11, it also can be seen that the seal does not leak for the 0.3  $\mu\text{m}$  seal roughness case as the instroke fluid transport is greater than the outstroke fluid transport. However, the seal does leak for the 0.5  $\mu\text{m}$  case as the outstroke fluid transport is larger than the instroke fluid transport.

## **CHAPTER 5**

### **CONCLUSIONS**

A numerical model and associated computer program have been developed to model a typical hydraulic rod seal. This model consists of fluid mechanics, deformation mechanics, and contact mechanics analyses and couples them to predict key seal performance characteristics such as leakage and friction. Based on the results shown in this numerical model, the seal may or may not leak depending on the roughness value for the seal as well as the operating speeds. For the base operating speeds, classical full film lubrication theory would predict that the seal would not leak. The created numerical model shows that this is not always the case. There is some limiting roughness value for below which the seal will seal properly and above which the seal will leak. Thus, the roughness must be taken into consideration when constructing a numerical model, which this model does. Additionally, previous numerical models have assumed full film lubrication throughout the sealing zone, but the results from this numerical model have shown that this is not necessarily the case. The results of the numerical model show that mixed lubrication is found in portions if not the entire sealing zone during both the instroke and outstroke of the rod. The inclusion of mixed lubrication also impacts the effectiveness of the seal. Cavitation and its effects were included in this numerical model. Cavitation impacts the amount of fluid transported during the outstroke of the rod, which can alter whether or not the seal will leak. Thus, the created numerical model for this project is successful as it takes into consideration the effects of seal roughness, mixed lubrication, and cavitation.

## APPENDIX A

### TDMA Procedure

The Tri-diagonal Matrix Algorithm (TDMA) is a procedure to solve a system of algebraic equations characterized by an  $N$  by  $N$  matrix with non-zero coefficients located along the three main diagonals. TDMA uses simplified Gaussian elimination involving forward elimination and backward substitution. This simplification significantly decreases the number of computations necessary to solve the system of equations.

The grid for the mesh of the sealing zone in this case is shown in Figure 33, where  $P$  denotes the present node at location  $i$ ,  $W$  is the western node at location  $i - 1$ , and  $E$  is the eastern node at location  $i + 1$ .

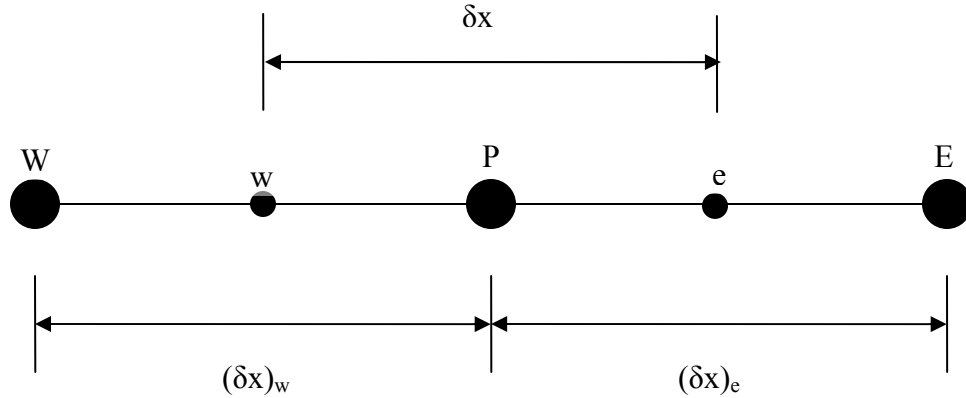


Figure 33: Nodal definitions

The first step in the algorithm is to set the boundary conditions for the pressure at the sealed and liquid sides of the seal to be implemented in the solution. The discretization equations found in Equation 46 are solved using the TDMA techniques to be outlined.

$$A_i \phi_i = B_i \phi_{i+1} + C_i \phi_{i-1} + D_i \quad (46)$$

where  $A_i$ ,  $B_i$ ,  $C_i$ , and  $D_i$  are defined for a positive speed by,

$$\begin{aligned}
A_i &= \left( \frac{2 \cdot K_{i+1} \cdot K_i}{K_{i+1} + K_i} + \frac{2 \cdot K_{i-1} \cdot K_i}{K_{i-1} + K_i} \right) \cdot F_i + 6\zeta(1 - F_i)(H_T)_{i+1} \\
B_i &= \left( \frac{2 \cdot K_{i+1} \cdot K_i}{K_{i+1} + K_i} \right) \cdot F_{i+1} \\
C_i &= \left( \frac{2 \cdot K_{i-1} \cdot K_i}{K_{i-1} + K_i} \right) \cdot F_{i-1} \\
D_i &= -6\zeta \cdot H_{i+1} + 6\zeta \{ [1 + (1 - F_{i-1})\phi_{i-1}](H_T)_{i-1} \} \\
&\quad - 6\zeta \cdot F_i \left[ \left( \frac{2 \cdot (\phi_{s.c.x.})_i \cdot (\phi_{s.c.x.})_{i+1}}{(\phi_{s.c.x.})_i + (\phi_{s.c.x.})_{i+1}} \right) - \left( \frac{2 \cdot (\phi_{s.c.x.})_i \cdot (\phi_{s.c.x.})_{i-1}}{(\phi_{s.c.x.})_i + (\phi_{s.c.x.})_{i-1}} \right) \right]
\end{aligned}$$

and for a negative speed by,

$$\begin{aligned}
A_i &= \left( \frac{2 \cdot K_{i+1} \cdot K_i}{K_{i+1} + K_i} + \frac{2 \cdot K_{i-1} \cdot K_i}{K_{i-1} + K_i} \right) \cdot F_i + 6\zeta(1 - F_i)(H_T)_{i-1} \\
B_i &= \left( \frac{2 \cdot K_{i+1} \cdot K_i}{K_{i+1} + K_i} \right) \cdot F_{i+1} \\
C_i &= \left( \frac{2 \cdot K_{i-1} \cdot K_i}{K_{i-1} + K_i} \right) \cdot F_{i-1} \\
D_i &= 6\zeta \cdot H_{i-1} - 6\zeta \{ [1 + (1 - F_{i+1})\phi_{i+1}](H_T)_{i+1} \} \\
&\quad - 6\zeta \cdot F_i \left[ \left( \frac{2 \cdot (\phi_{s.c.x.})_i \cdot (\phi_{s.c.x.})_{i+1}}{(\phi_{s.c.x.})_i + (\phi_{s.c.x.})_{i+1}} \right) - \left( \frac{2 \cdot (\phi_{s.c.x.})_i \cdot (\phi_{s.c.x.})_{i-1}}{(\phi_{s.c.x.})_i + (\phi_{s.c.x.})_{i-1}} \right) \right]
\end{aligned}$$

The forward elimination is implemented according to equations 47, 48, 49, and 50 involving those equations according to the techniques of Patankar (1980) to obtain the P and Q distributions.

$$P(1) = \frac{B(1)}{A(1)} \tag{47}$$

$$Q(1) = \frac{D(1)}{A(1)} \tag{48}$$

$$P(I) = \frac{B(I)}{A(I) - C(I) \cdot P(I-1)} \tag{49}$$

$$Q(I) = \frac{D(I) + C(I) \cdot Q(I-1)}{A(I) - C(I) \cdot P(I-1)} \quad (50)$$

Finally, a back substitution of the obtained values is performed to obtain the pressure distribution,  $\phi$ , which is shown in Equations 51 and 52.

$$\phi(N) = Q(N) \quad (51)$$

$$\phi(I) = P(I) \cdot \phi(I+1) + Q(I) \quad (52)$$

The effects of cavitation are taken into consideration using the switch,  $F$ , previously introduced. Thus, if the  $\phi$  is positive, the switch is set to a value of 1 and otherwise the switch is set to a value of zero.

After this step, a convergence check is performed on the pressure distribution to see that if the maximum change in pressure at a node no longer exceeds an established convergence criterion. If this criterion is not satisfied, the pressure and cavitation parameters are then updated via relaxation parameters and the TDMA procedure continues until convergence is met.

## APPENDIX B

### Dimensional Results for 6.9 MPa Sealed Pressure

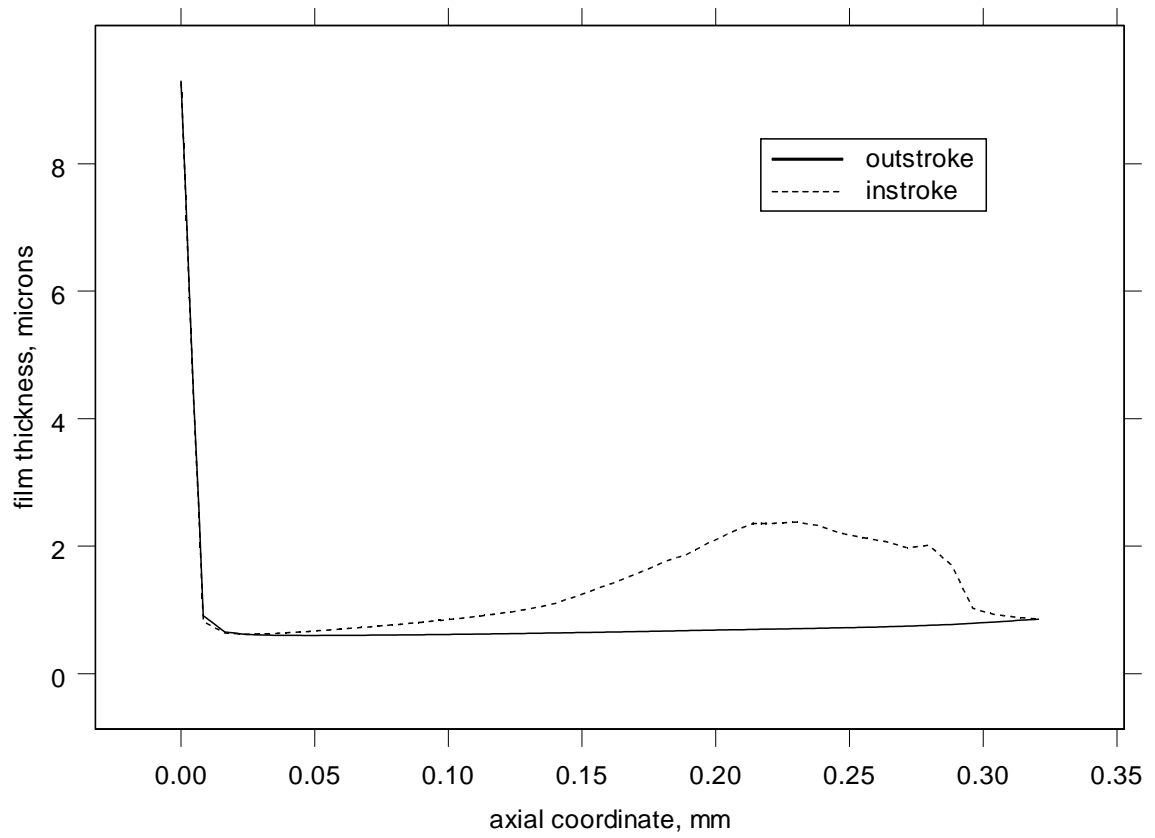


Figure 34: Film thickness distributions, base case



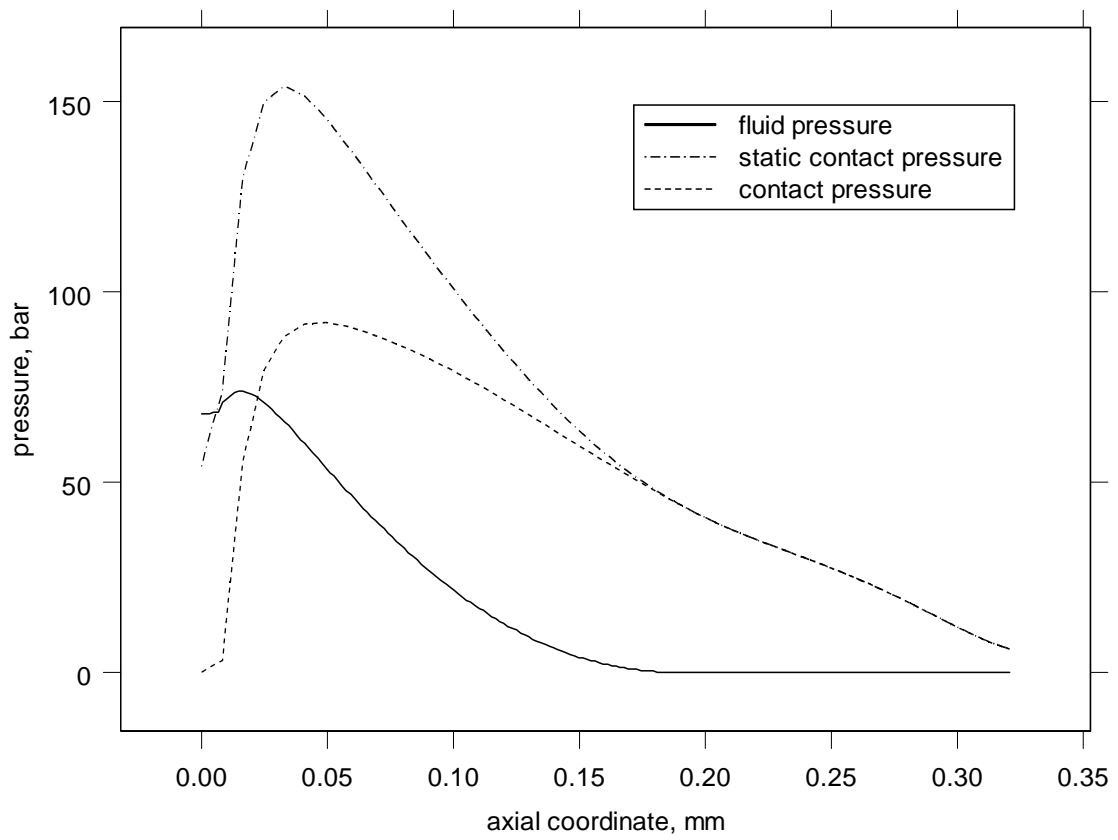


Figure 35: Pressure distributions, outstroke, base case

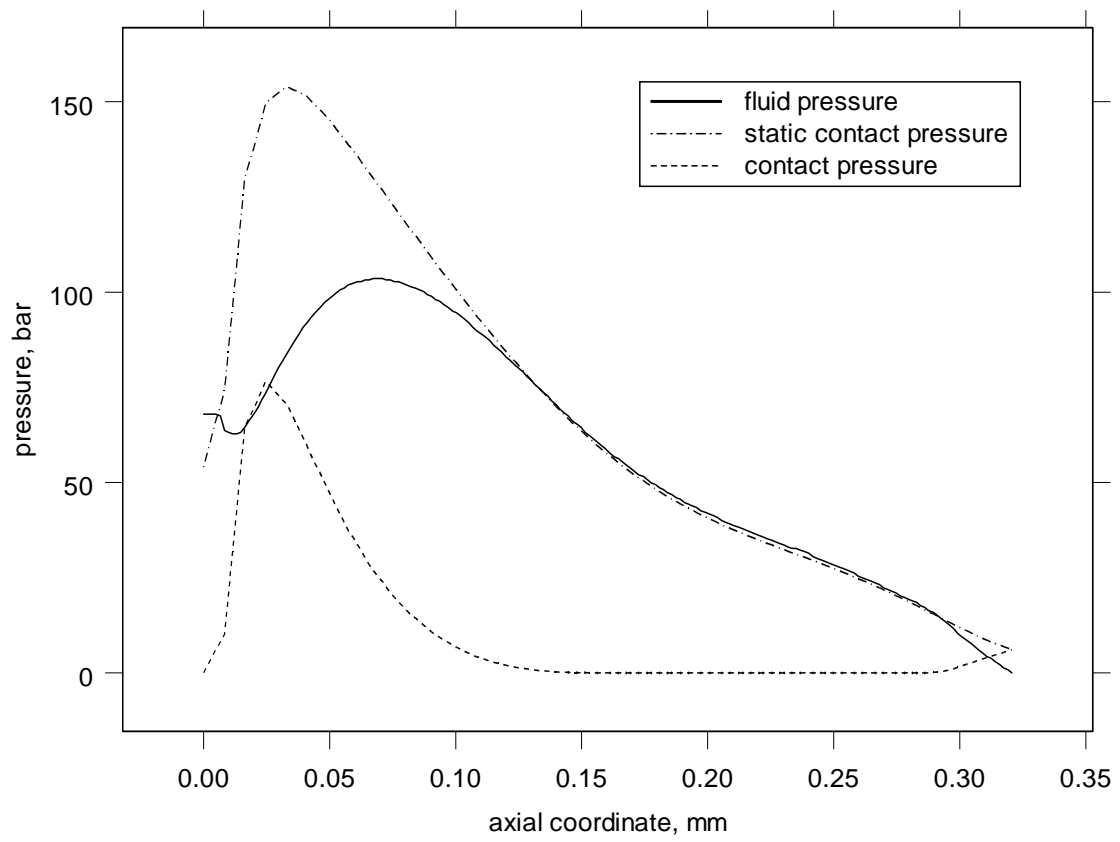


Figure 36: Pressure distributions, instroke, base case

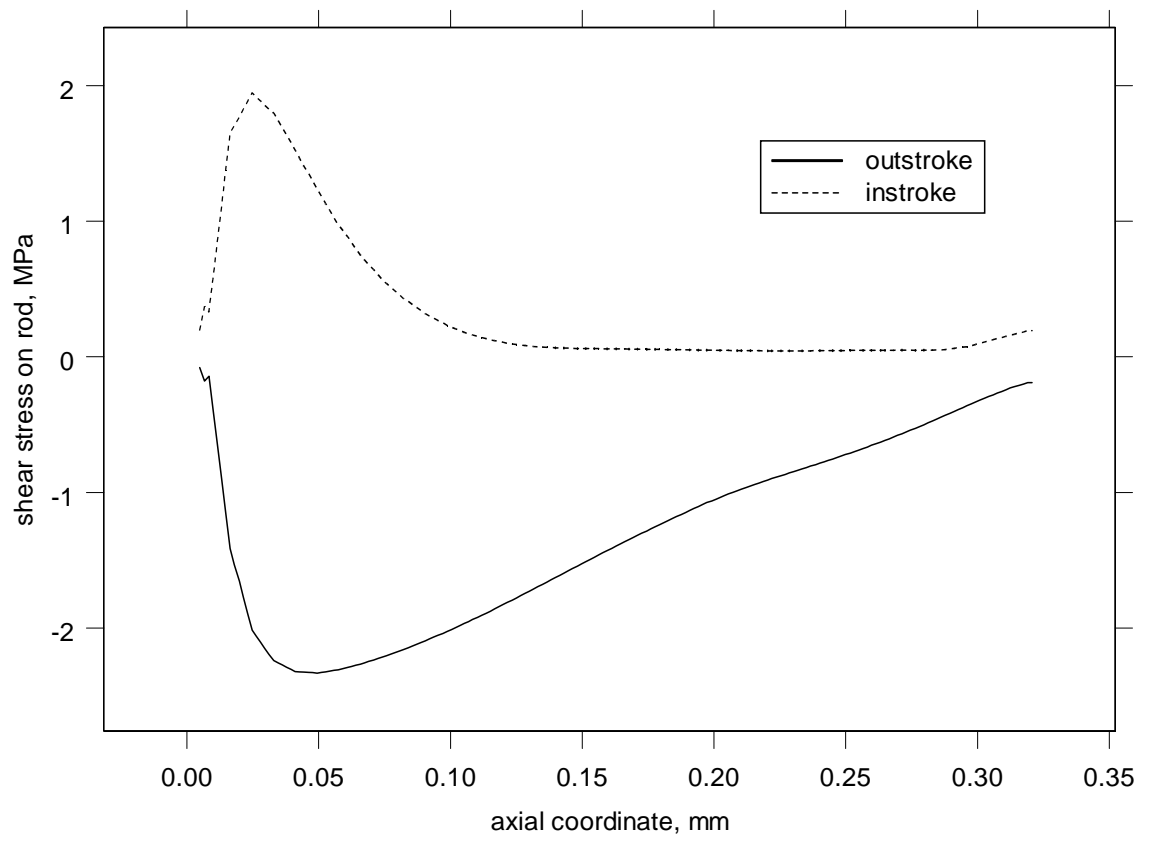


Figure 37: Frictional shear stress distributions, base case

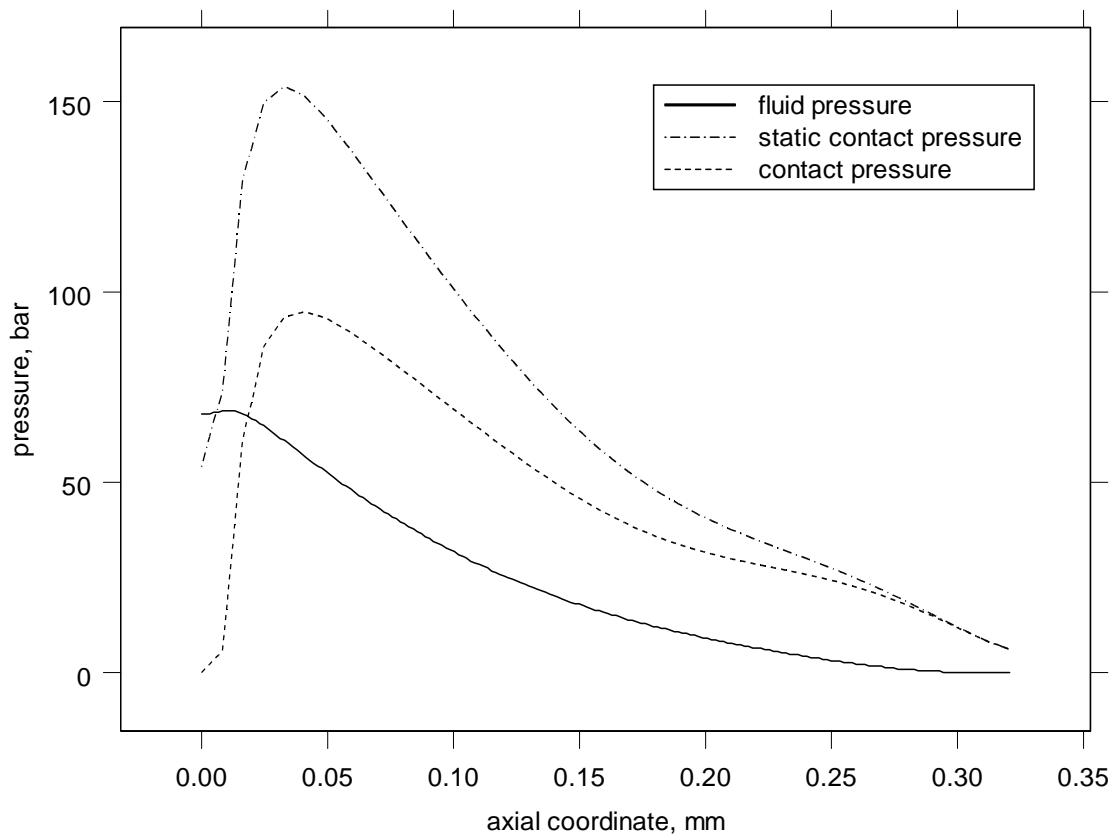


Figure 38: Pressure distributions, outstroke, 0.5  $\mu\text{m}$  roughness

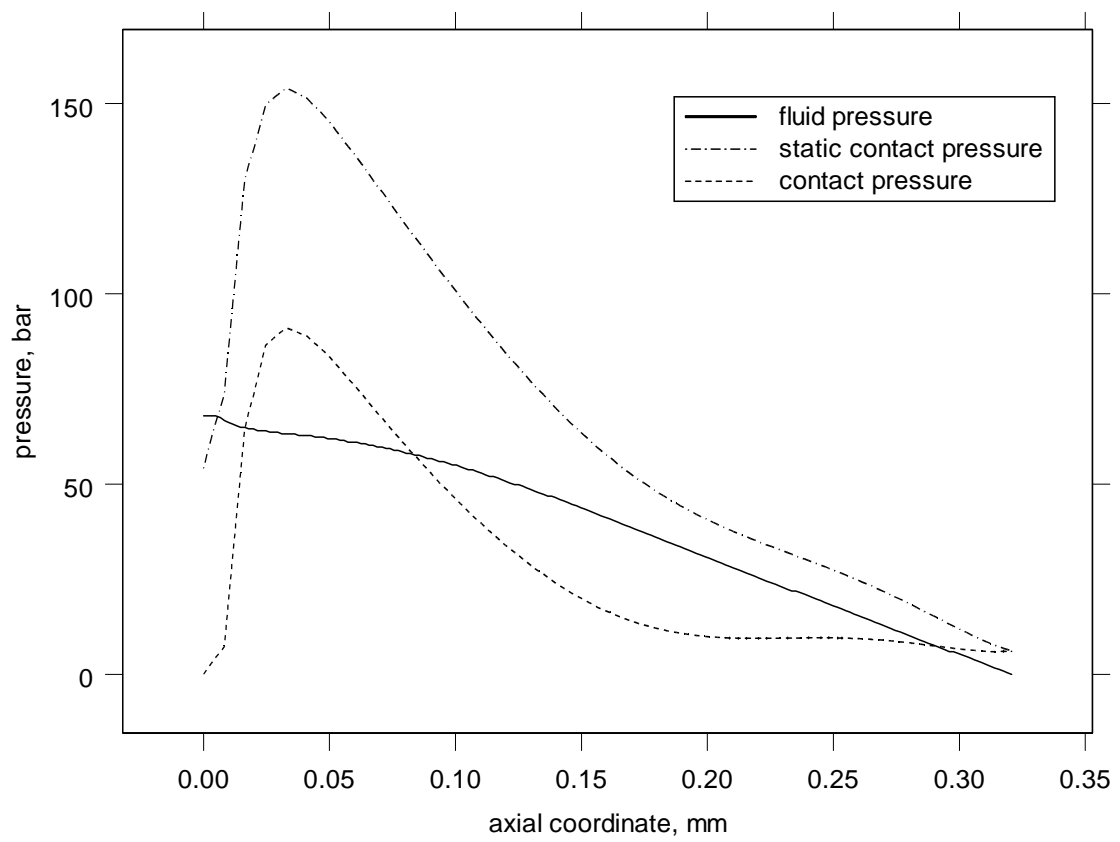


Figure 39: Pressure distributions, instroke, 0.5  $\mu\text{m}$  roughness

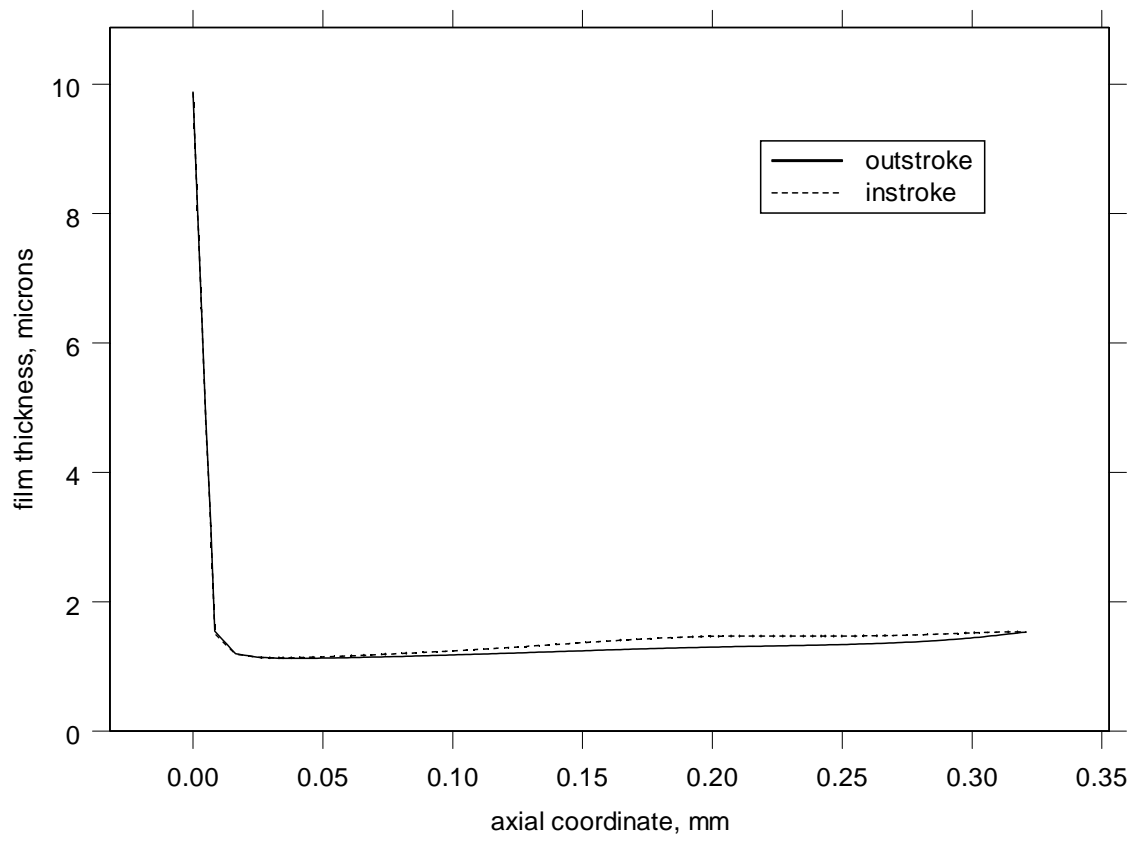


Figure 40: Film thickness distributions, 0.5  $\mu\text{m}$  roughness

## APPENDIX C

### Dimensional Results for 13.8 MPa Sealed Pressure

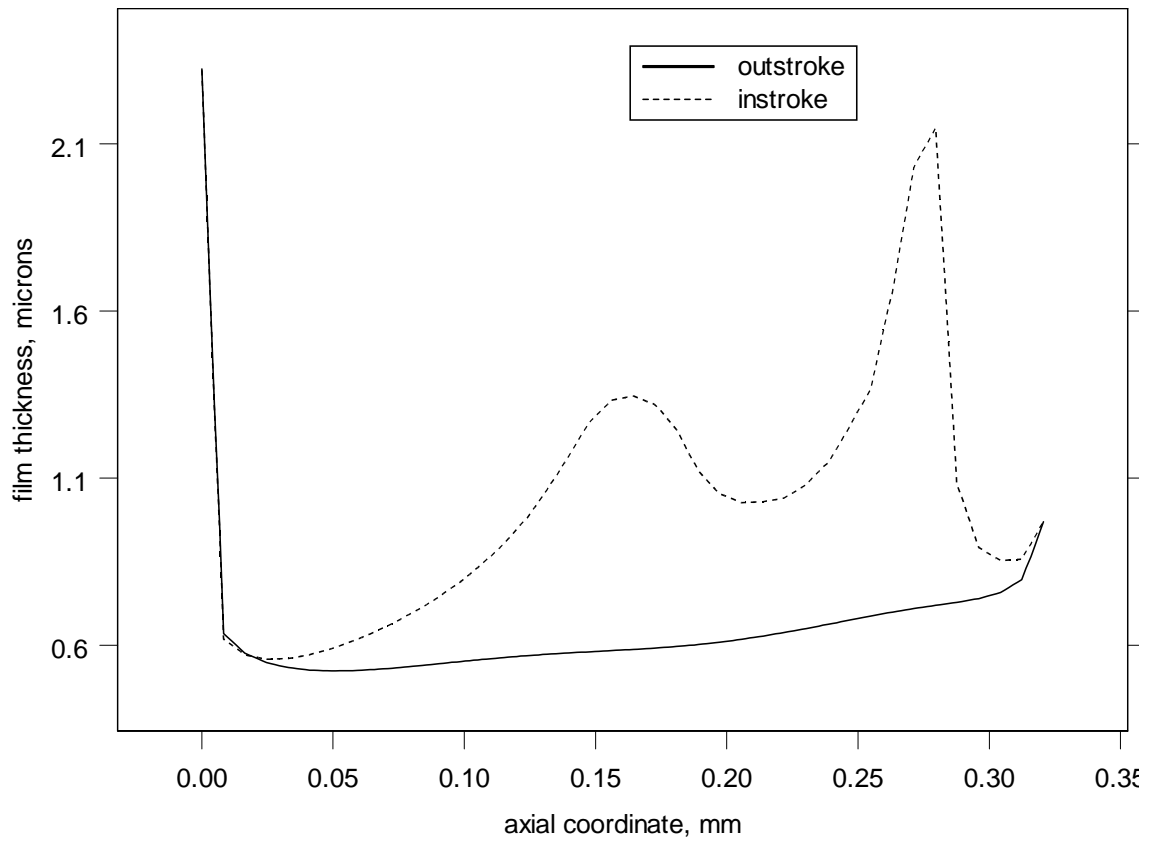


Figure 41: Dimensional film thickness distributions for 13.8 MPa, base case

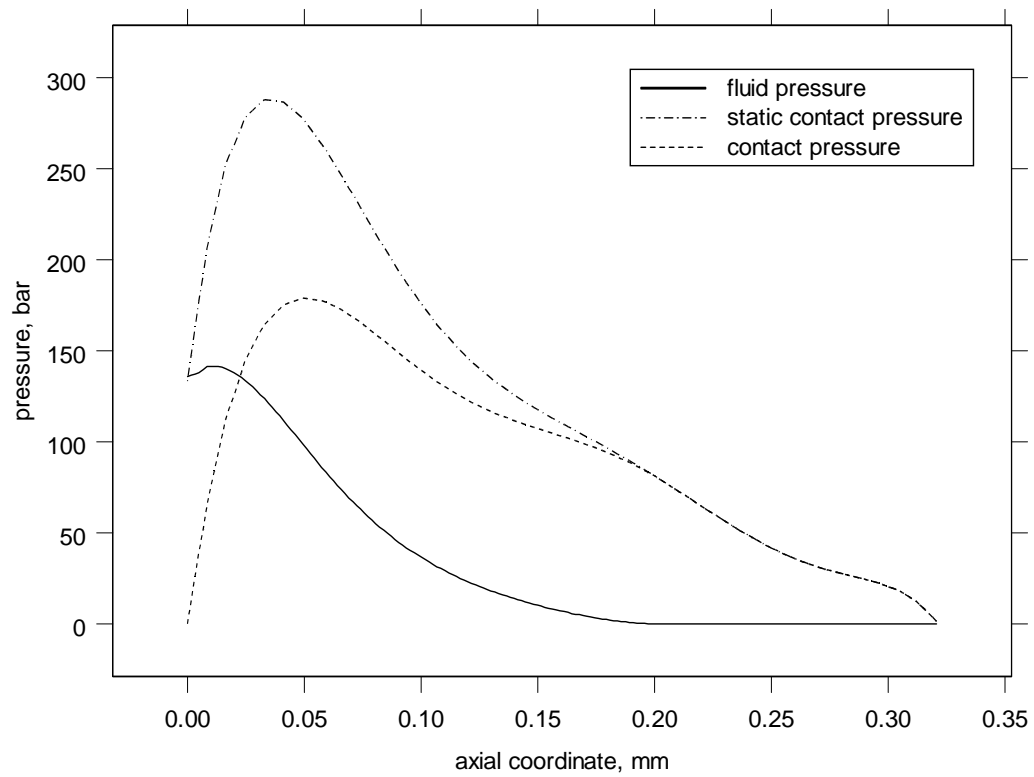


Figure 42: Dimensional pressure distributions, outstroke, base case, 13.8 MPa



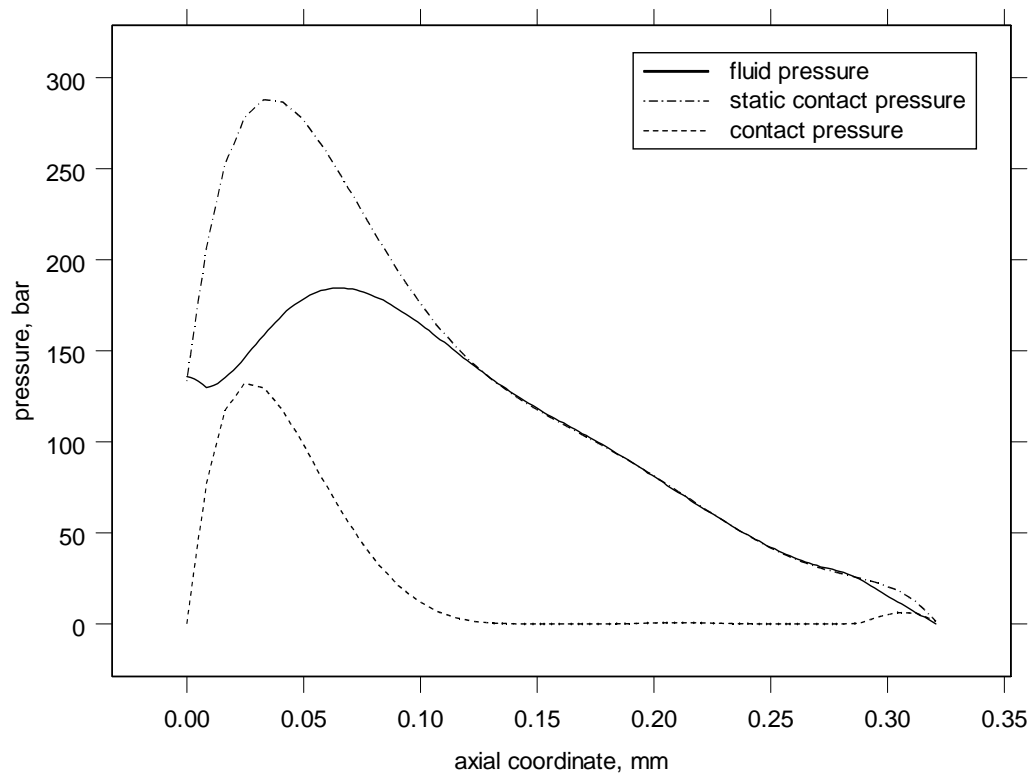


Figure 43: Dimensional pressure distributions, instroke, base case, 13.8 MPa

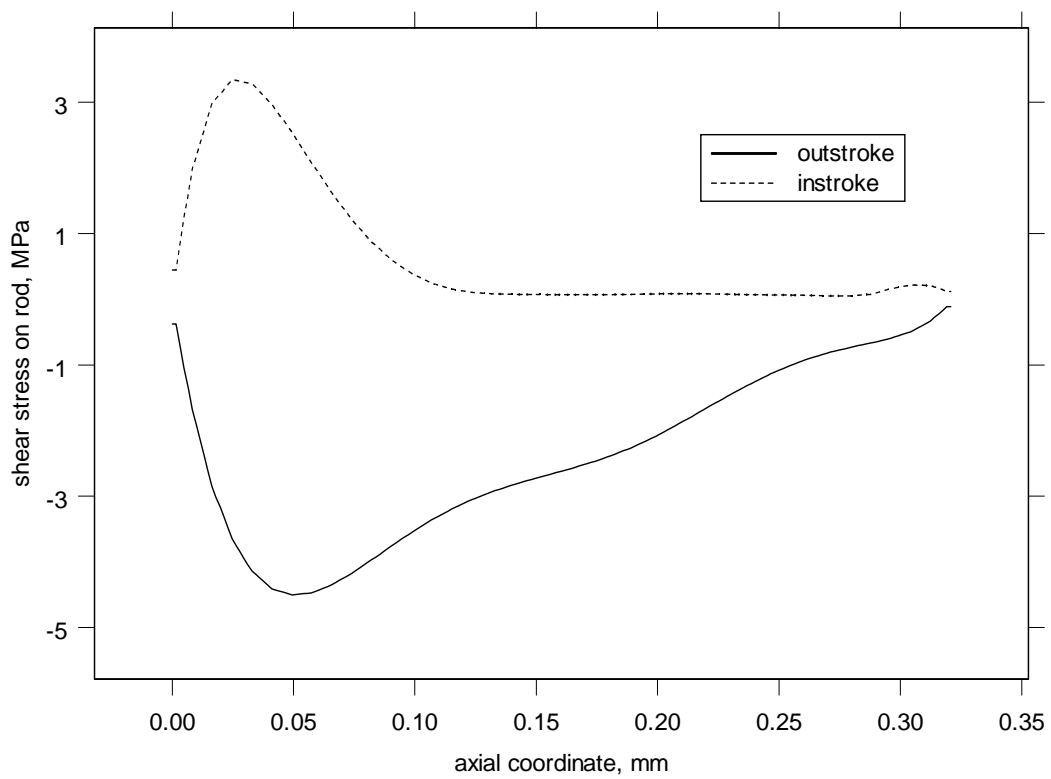


Figure 44: Frictional shear stress distributions, base case, 13.8 MPa

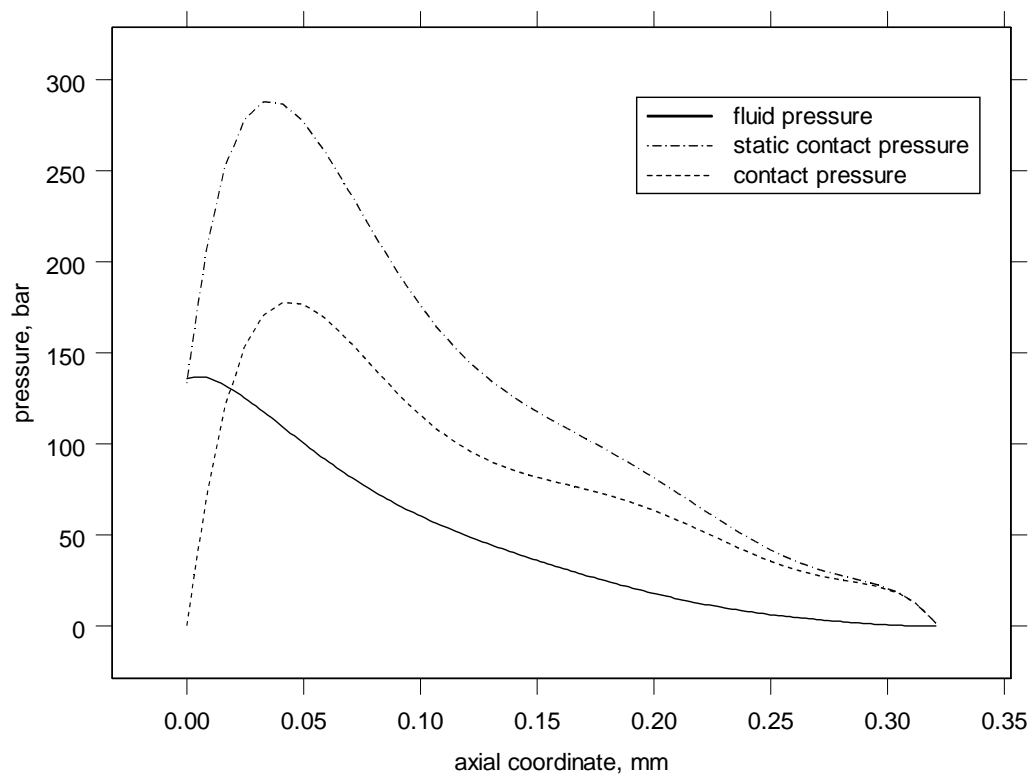


Figure 45: Dimensional pressure distributions, outstroke, 0.5  $\mu\text{m}$  roughness

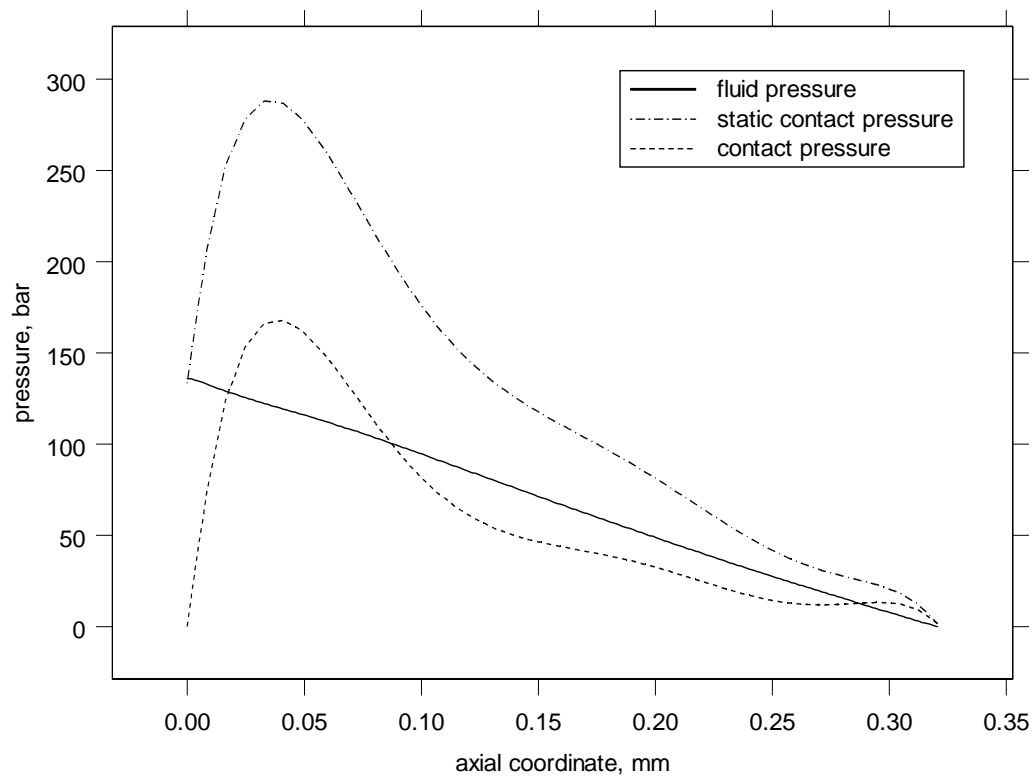


Figure 46: Dimensional pressure distributions, instroke,  $0.5\text{ }\mu\text{m}$  roughness

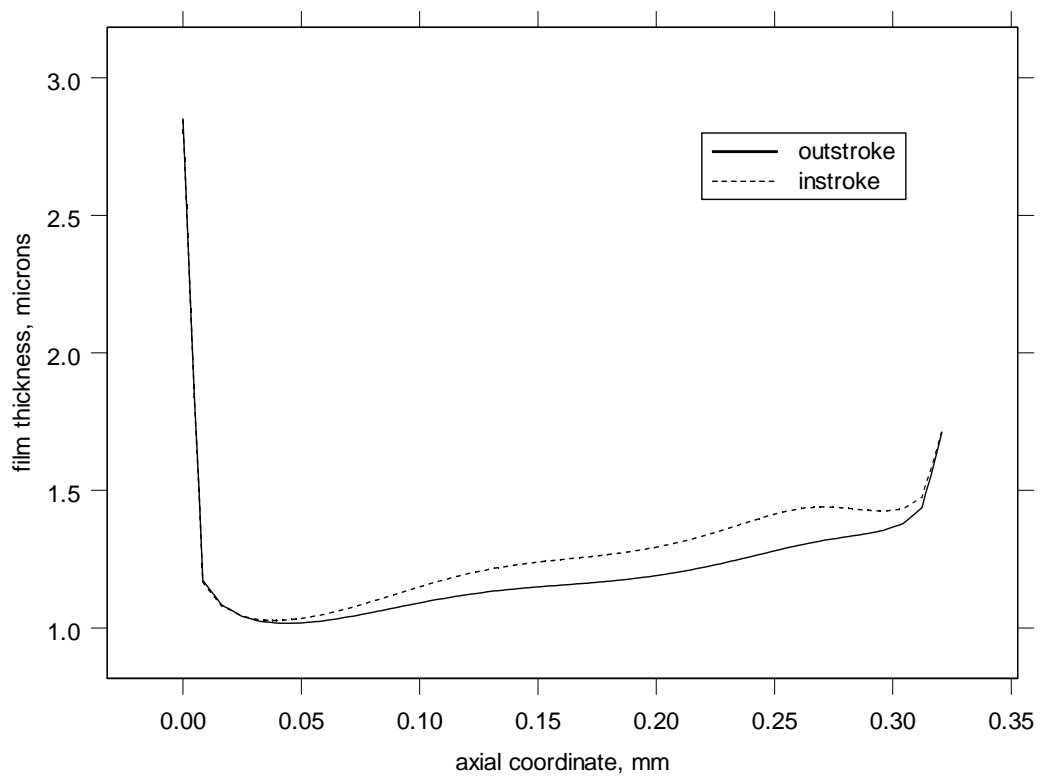


Figure 47: Dimensional film thickness distributions for 13.8 MPa, 0.5  $\mu\text{m}$  roughness

## REFERENCES

- Claus, R. G., "Development of a High Performance, Heavy Duty Piston Seal", *Proc. 49th National Conference on Fluid Power*, NFPA, pp. 383-389 (2002).
- Field, G. J., Nau, B. S., "A Theoretical Study of the Elastohydrodynamic Lubrication of Reciprocating Rubber Seals", *ASLE Transactions*, vol. 18, pp. 48-54 (1974).
- Field, G. J., Nau, B. S., "Film Thickness and Friction Measurements During Reciprocation of a Rectangular Section Rubber Seal Ring", *Proc. 6th BHRA International Conference on Fluid Sealing*, C5 (1973).
- Greenwood, J. A., Williamson, J. B. P., "Contact of Nominally Flat Rough Surfaces", *Proc. Royal Society (London)*, vol. A295, pp. 300-319 (1966).
- Hirano, F., Kaneta, M., "Theoretical Investigation of Friction and Sealing Characteristics of Flexible Seals for Reciprocating Motion", *Proc. 5th BHRA International Conference on Fluid Sealing*, G2 (1971).
- Ishiwata, H., Kambayashi, H., "A Study of Oil Seal for Reciprocating Motion", *Proc. 2nd BHRA International Conference on Fluid Sealing*, B3 (1964).
- Kanters, A. F. C., Verest, J. F. M., Visscher, M., "On Reciprocating Elastomeric Seals: Calculation of Film Thicknesses Using the Inverse Hydrodynamic Lubrication Theory", *Tribology Transactions*, v. 33, pp. 301-306 (1990).
- Kanters, A. F. C., Visscher, M., "Lubrication of Reciprocating Seals: Experiments on the Influence of Surface Roughness on Friction and Leakage", *Proc. 15th Leeds-Lyon Symposium on Tribology*, pp. 69-77 (1988).
- Kawahara, Y., Ohtake, Y., Hirabayashi, H., "Oil Film Formation of Oil Seals for Reciprocating Motion", *Proc. 9th BHRA International Conference on Fluid Sealing*, C2 (1981).
- Müller, H. K., Nau, B. S., *Fluid Sealing Technology*, Marcel Dekker, New York (1998).
- Naderi, A., Albertson, K., Peng, S., "Finite Element Analysis of a Hydraulic Seal: BS U-Cup", *Proc. 46th National Conference on Fluid Power*, NFPA, pp. 99-105 (1994).
- Nikas, G. K., "Elastohydrodynamics and Mechanics of Rectangular Elastomeric Seals for Reciprocating Piston Rods", *J. of Tribology*, vol. 125, pp. 60-69 (2003).

Nikas, G. K., “Transient Elastohydrodynamic Lubrication of Rectangular Elastomeric Seals for Linear Hydraulic Actuators”, *J. of Engineering Tribology*, vol. 217, pp. 461-473 (2003).

Nikas, G. K., Sayles, R. S., “Nonlinear Elasticity of Rectangular Elastomeric Seals and its Effect on Elastohydrodynamic Numerical Analysis”, *Tribology International*, vol.37, pp. 651-660 (2004).

O’Donogue, J. P. and Lawrie, J. M., “The Mechanism of Lubrication in a Reciprocating Seal”, *Proc. 2nd BHRA International Conference on Fluid Sealing*, B6 (1964).

Patankar, S.V., 1980, *Numerical Heat Transfer and Fluid Flow*, New York, Hemisphere.

Patir, N., Cheng, H. S., “An Average Flow Model for Determining Effects of Three-Dimensional Roughness on Partial Hydrodynamic Lubrication”, *J. of Lubrication Technology*, vol. 100, pp. 12-17 (1978).

Patir, N., Cheng, H. S., “Application of Average Flow Model to Lubrication Between Rough Sliding Surfaces”, *J. of Lubrication Technology*, vol. 101, pp. 220-229 (1979).

Pavyar, P. and Salant, R.F., 1992, “A Computational Method for Cavitation in a Wavy Mechanical Seal”, *ASME Journal of Tribology*, Vol. 114, pp. 199-204.

Peng, S., Sun, S., Albertson, K., “FEA-Assisted Design of Low-Friction U-Cup as Spool Valve Seals”, *Proc. 47th National Conference on Fluid Power*, NFPA, pp. 175-182 (1966).

Prati, E., Strozzi, A., “A Study of the Elastohydrodynamic Problem in Rectangular Elastomeric Seals”, *J. of Tribology*, vol. 24, pp. 505-512 (1984).

Ruskell, L. E. C., “A Rapidly Converging Theoretical Solution to the Elastohydrodynamic Problem for Rectangular Rubber Seals”, *J. Mechanical Engineering Science*, vol. 22, pp. 9-16 (1980).

Salant, R.F., Maser, N., Yang, B., “Elastohydrodynamic Model of a Reciprocating Hydraulic Rod Seal”, *Proc. AITC-AIT 2006 International Conference on Tribology*, Sept 20-22, 2006, Parma, Italy.

Salant, R.F., Maser, N., Yang, B., “Numerical model of a reciprocating hydraulic rod seal, including seal roughness and mixed lubrication”, *Proc. 14<sup>th</sup> International Sealing Conference*, Oct 10-11, 2006, Stuttgart, Germany.

Salant, R.F., Maser, N., Yang, B., “Numerical Model of a Reciprocating Rod Seal”, *Journal of Tribology*, accepted for publication, and *Proc. STLE/ASME International Joint Tribology Conference*, Oct 20-25, 2006, San Antonio, TX, U.S.A.

Streator, J. L., “A Model of Mixed Lubrication with Capillary Effects”, *Proc. 15th Leeds-Lyon Symposium on Tribology*, pp. 121-128 (2001).

Weiss, H., “New Generation of Hydraulic Seals Supports Progress for Hydraulic Cylinders”, *Proc. 47th National Conference on Fluid Power*, NFPA, pp. 153-163 (1996).

Yang, Y., Hughes, W. F., “An Elastohydrodynamic Analysis of Preloaded Sliding Seals”, *ASLE Transactions*, vol. 27, pp. 197-202 (1983).